Doctoral Dissertation (Censored)

博士論文（要約）

Synthesis and Materials Properties of Spiro-conjugated Carbon-bridged Phenylenevinylenes

（スピロ接合型炭素架橋フェニレンビニレンの合成と物性）

A Dissertation Submitted for the Degree of Doctor of Philosophy

December 2019

令和元年 12 月 博士（理学）申請

Department of Chemistry, Graduate School of Science,
The University of Tokyo
東京大学大学院 理学系研究科 化学専攻

Hiroyoshi Hamada
濱田　拓実

Abstract

Organic π-conjugated molecules have been attracting much attention because their potential applications in optoelectronic and semiconducting materials. The properties of organic materials are largely derived from their molecular structure. Hence, the construction of new molecular backbone by molecular design enables the desired materials properties and opens up the new dimensional materials. Based on this concept, in my doctoral course study, I focused on two new π-conjugated scaffolds where planer π-conjugated systems are connected via an olefinic- or a spiro-linkage. The integration of materials properties is successfully achieved by the combination of functional structures, which provides the opportunities for further applications.

Chapter 2 describes the aggregation-responsive two wavelength on-off-on fluorescence switching behavior of tetrakis(benzo[*b*]furyl)ethene (**TBFE**). The molecule designed in combination of emissive benzo[*b*]furyl units and tetraarylethene, a well-known aggregation-induced emission backbone. Three-stage two-wavelength on-off-on fluorescence switching was achieved in THF/H_2O mixed solvents. The mechanistic study revealed the switching is derived from aggregation-induced properties, suggesting materials properties could be integrated by the combination of functional molecular structures.

In Chapter 3–6, the investigation on spiro-conjugated carbon-bridged *p*-phenylenevinylenes (Spiro-CPVs) are described. Chapter 3 reports the design, synthesis and properties of spiro-CPV core structure. The novel spiro π-conjugated backbone was designed by utilizing a bridging sp^3 carbon atom of carbon-bridged oligo(*p*-phenylenevinylene) (COPV) as a spiro center to connect two COPV units in perpendicular. Spiro-CPV exhibited circularly polarized luminescence (CPL) with high stability and inter-subunit electron interaction thanks to structural rigidity, molecular chirality, and spiroconjugation derived from spiro-linkage.

Chapter 4 describes the enhancement of radiative decay by π-elongation of spiro-CPV.

Expansion of π-system on spiro-CPV intensified extinction coefficient, and hence accelerated radiative decay. High radiative rate constant was achieved by the attaching phenylethynyl group to show a fluorescence quantum yield of 0.99, the highest value for organic CPL molecules.

In Chapter 5, the modification of electronic structure by the incorporation of heterocycle is described. The electronic properties in the rigid spiro-CPV backbone changed due to electron donating and accepting effects of heteroatoms. Especially, the introduction of SO_2 group caused intramolecular charge transfer upon photoexcitation to evoke solvatochromism in fluorescence. Moreover, the linear correlation of a luminescence dissymmetry factor and solvent polarity was observed, which is rarely reported possibly because of large structural reorganizations causing randomization of dissymmetry.

Chapter 6 describes the development of spiro-CPV-based hole transporting materials (HTMs). Tetrakis(diarylamino) spiro-CPVs have appropriate energy levels for the use as HTM and higher amorphous state stabilities than spiro-OMeTAD, a common hole transporting material. Spiroconjugation enabled inter-subunit electronic interactions in their radical cations, enhancing hole transfer in their spin-coated films by oxidant doping.

These investigations demonstrated that the integration of functional structures evokes materials properties that are more than just a summation of structure-derived properties, and therefore, could be a strong strategy to design materials properties.

Acknowledgements

The studies described in this thesis were carried out under the supervision of Professor Eiichi Nakamura at The University of Tokyo. I would like to express my sincerest gratitude to Professor Eiichi Nakamura for his professional support, valuable suggestions, and continuous encouragements during the course of study.

I gratefully appreciate to Professor Hayato Tsuji at Kanagawa University for his guidance in the study described in Chapter 2. I wish to express my acknowledgement to Dr. Rui Shang for his advice and discussion in the spiro-CPV studies.

I also thank Dr. Koji Harano, Dr. Laurean Ilies, and Dr. Takayuki Nakamuro, for their helpful advice, suggestions, and encouragements.

I would like to appreciate to all the laboratory members for their kind help. I would like to express my thanks to the members spent time together in same group for the daily discussion and sharing joy during my life in the laboratory; in particular: Dr. Zhongmin Zhou, Dr. Hiroki Nishioka, Dr. Yuki Itabashi, Dr. Takenari Sato, Mr. Ziyue Qiang, Mr. Takumi Sakamaki, and Mr. Yuki Sendai.

Finally, I would like to express sincere gratitude to Mr. Osamu Hamada and Ms. Masayo Hamada for their daily help, advice, and encouragement and for their continuous love.

Table of Contents

Abbreviations

ACQ	aggregation-caused quenching
AIE	aggregation-induced emission
APCI	atomic pressure chemical ionization
ASE	amplified spontaneous emission
BF	2-phenylbenzo[b]furan
B3LYP	Becke's 3-parameter hybrid with Lee, Young and Parr's correlation functional
CD	circular dichroism
COPV	carbon-bridged oligo(p-phenylenevinylene)
CPL	circularly polarized luminescence
CV	cyclic voltammetry
DFT	density functional theory
DLS	dynamic light scattering
DPV	differential pulse voltammetry
DSC	differential scanning calorimetry
EA	electron affinity
$E_{M^{4+}/M}$	standard reduction potential
E_{ox}	oxidation potential
ELT	electron transport layer
ESR	electron spin resonance
f	oscillator strength
FTO	fluorine doped tin oxide
$\|g_{abs}\|$	absorption dissymmetry factor
$\|g_{lum}\|$	photoluminescence dissymmetry factor
HTM	hole transporting material
HTL	hole transport layer
HOMO	highest occupied molecular orbital
HPLC	high-pressure liquid chromatography
HRMS	high-resolution mass spectrum

ICT	intramolecular charge transfer
IP	ionization potential
ITO	indium tin oxide
k_{nr}	nonradiative rate constant
k_r	radiative rate constant
LiNaph	lithium naphthalenide
LiTFSI	lithium bi(trifluoromethanesulfonyl)imide
LUMO	lowest unoccupied molecular orbital
mCPBA	*m*-chloroperoxybenzoic acid
MO	molecular orbital
MECI	minimum energy conical intersection
NMR	nuclear magnetic resonance
OBG	optical bandgap
PCE	power conversion efficiency
PEDOT	poly(3,4-ethylenedioxythiophene)
PSS	poly(styrenesulfonate)
PVSC	perovskite solar cell
PYS	photoelectron yield spectroscopy
r	atomic radius
SCLC	space charge limited current
SEM	scanning electron microscopy
spiro-CPV	spiro-conjugated carbon-bridged p-phenylenevinylene
spiro-OMeTAD	2,2',7,7'-tetrakis(*N*,*N*-di-*p*-methoxyphenyl-amine)9,9'-spirobifluorene
TAE	tetraarylethene
TBFE	tetrakis(benzo[*b*]furyl)ethene
TBP	2,6-di-*tert*-butylpyridine
TD	time-dependent
TGA	thermogravimetric analysis
TLC	thin-layer chromatography
T_{5d}	5% weight loss temperature

T_g	glass transition temperature
UV	ultraviolet
XRD	X-ray diffraction
$\lvert[\alpha]_D^{20}\rvert$	specific rotation
Φ_{FL}	fluorescence quantum yield
Δf	orientation polarizability parameter
$\Delta\nu$	Stokes shift
ε	molar extinction coefficient
λ	wavelength
μ	dipole moment
μ_h	hole mobility
τ	fluorescence lifetime

Chapter 1.

General Introduction

1.1. Organic π-conjugated materials: structure and properties

Organic π-conjugated molecules have been attracting organic and material scientists due to their applications for the wide fields, such as functional dyes[1] and semiconducting and optoelectronic devices,[2] and their scientific interests on aromaticity, radicals,[3] and so on. The properties of π-conjugated compounds are largely determined by their molecular structures and shapes. Configurationally, flat and rigid polyaromatics[4,5] are often emissive, stable and conductive due to their efficient π-systems, while curved π-conjugated molecules[6] show uncommon packing structure, molecular recognition, and molecular chirality because of unique topologies. Fullerenes[7] are often used as carrier transporting materials thanks to their spherical conjugation systems where charge delocalized on their whole structures to make reorganization energy small. Electronically, the incorporation of heteroatom[8] enables the modification of electronic structure to evoke unique functions that are difficult to achieve in hydrocarbons. By combining different functional structures, various organic material compounds have been designed to exhibit the desirable properties.

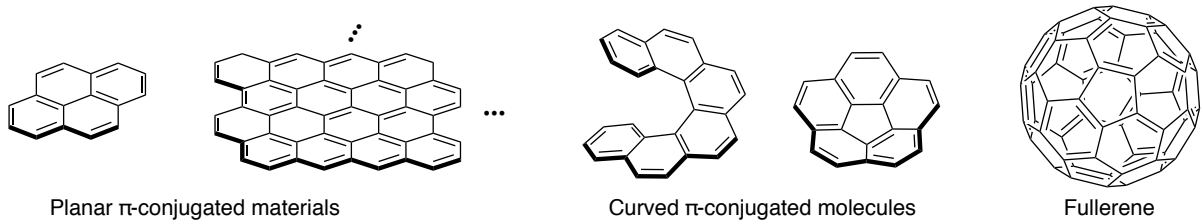

Figure 1.1. Examples of polyaromatics.

Our laboratory has developed organic π-conjugated scaffolds such as fused polycyclic furans[9] and carbon-bridged oligo(*p*-phenylenevinylene)s[4c] (COPVs). The furyl compounds overcome the instability of furyl rings by fusion of carbon aromatics and introduction of substituents, to allow their use in optoelectronic devices. COPV backbones are designed to inhibit the problematic structural disorder of oligo(*p*-phenylenevinylene)s by insertion of sp^3 carbon-bridged structure. COPVs are found to exhibit intense photoluminescence with high stability and efficient charge transfer. The use of the carbocycles and their polymeric derivatives in the fields of organic optoelectronics, molecular wires, and light harvesting were demonstrated.[4c, 10]

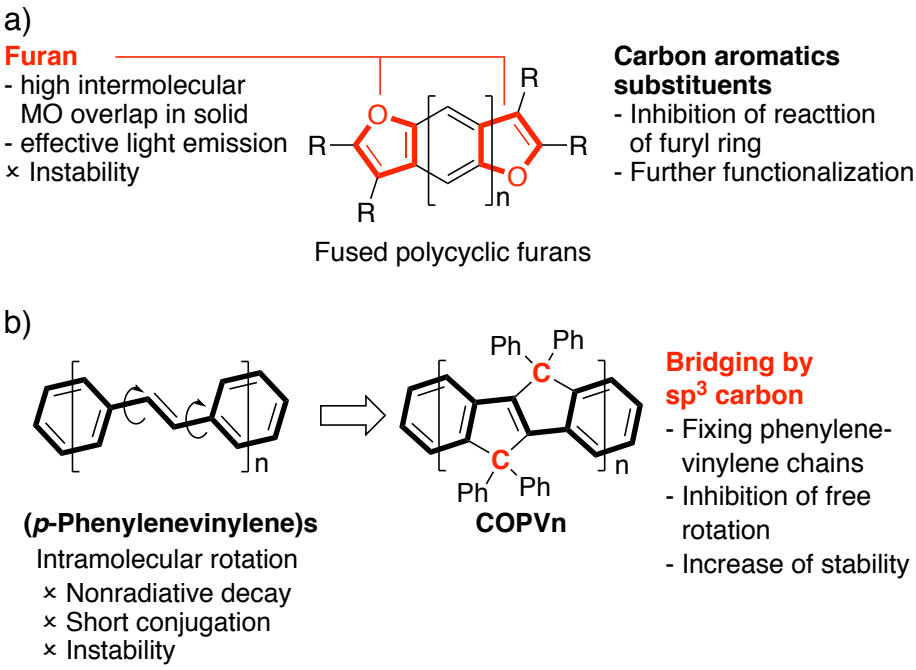

Figure 1.2. Structures and molecular designs of fused polycyclic furans and COPVs.

1.2. Spiro linkage: connection of two π units via a carbon atom

1.2.1. Spiro linkage of π-conjugated systems

Connection of organic π-conjugated compounds as π-units via functional linker structure expands the variety of materials properties. Spiro-linkage connects two π-conjugated system in perpendicular via a spiro-central carbon atom (Figure 1.3a). In 1997, Salbeck *et al.* introduced the three-dimensional spiro structure for organic semiconducting materials[11] to enable the improvement of morphologic stability and processability of small organic materials with the electronic properties of single π-units retained (Figure 1.3b). For example, it was demonstrated that 2,2',7,7'-tetrakis(diphenylamino)-9,9'-spirobifluorene (spiro-TAD) has much better glass transition temperature (T_g) than the parent compound, *N,N,N',N'*-tetraphenylbenzidine (TAD), while their hole mobility (μ_h) are comparable.[12] From this result, it is expected that the fusion of two functional π-conjugated compounds would give novel spiro compounds where the materials properties of each π-units and spiro-linkage are combined.

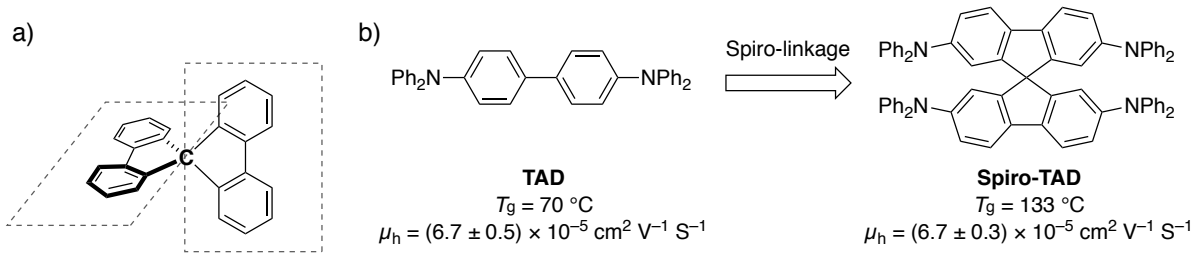

Figure 1.3. Spiro-linkage a) Structure. b) Improvement of T_g without change of μ_h.

1.2.2. Spiroconjugation

Spiro-linkage structure also evokes different electronic interactions between the connected systems. In 1967, Hoffmann *et al.*[13] and Fukunaga *et al.*[14] separately reported homoconjugation in spiro system, so-called "spiroconjugation" (Figure 1.4), which enables the electronic interaction between two connected π-systems via the quantum interference of molecular orbitals (MOs) around a spiro-center. In 1973, Schweig *et al.*[15] experimentally observed energy splitting of HOMO levels, so-called "spiro-splitting", by spectroscopic study on several spiro compounds for the first time to demonstrate the MO interaction via spiroconjugation. In 2018, Gauger *et al.* demonstrated the use of a spiro[4,4]nonatetracene molecule as molecular junction to utilize this quantum interference effect by spiroconjugation in the field of molecular electronics.[16] The orthogonal structure can also be utilized to regulate the electronic interactions. For instance, combination of electron-donor and acceptor units orthogonally connected via spiro structure efficiently gives appropriate MO separation.

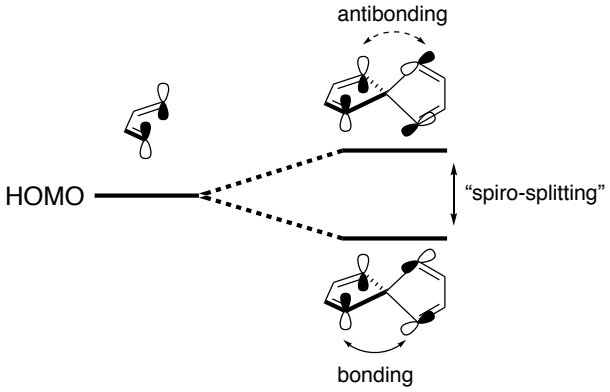

Figure 1.4. Spiroconjugation and spiro-splitting of HOMOs.

1.2.3. Construction of spiro structure

Since the first report on synthesis of 9,9'-spirobifluorene by Clarkson and Gomberg in 1930,[17] many spiro compounds have been synthesized and investigated their materials properties. The first method is based on the Friedel-Crafts type intramolecular cyclization in acidic condition (Scheme 1.1a), which have been used as the general strategy of the construction of spiro structure. In 2004, Zhou *et al.* reported an alternative route to synthesize spirobifluorene structure (Scheme 1.1b),[18] which undergoes double intramolecular cyclization.

Scheme 1.1. Construction of 9,9'-spirobifluorene structure reported by a) Clarkson and Gomberg and b) Zhou *et al.*

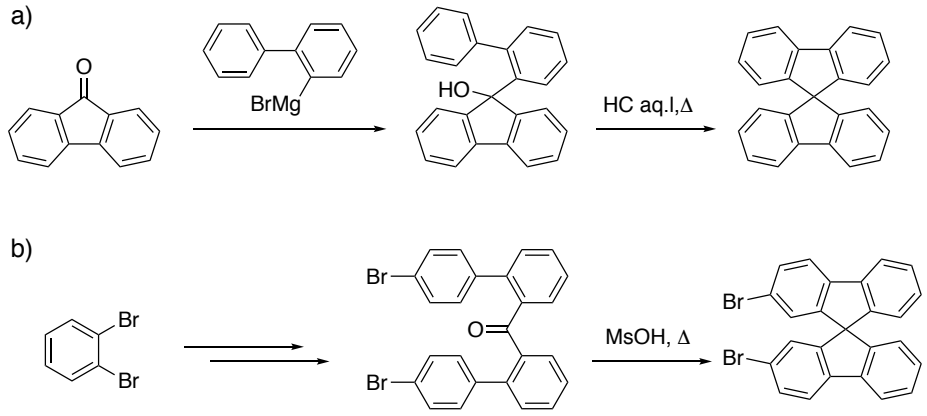

1.2.4. Spiro π-conjugated compounds as organic semiconducting materials

Spiro compounds have been utilized experimentally as carrier transporting materials in semiconducting devices[11] because of small reorganization energy, high morphological stability, and solubility attributed by spiroconjugation and three-dimensional structure. For instance, 2,2',7,7'-tetrakis(*N*,*N*-di-*p*-methoxyphenyl-amine)9,9'-spirobifluorene (Spiro-OMeTAD, Figure 1.5), reported by Grätzel *et al.* as a hole transporting material in dye sensitized solar cell in 1998,[19] has been utilized as one of the most common hole transporting material in the fields of organic semiconducting devices. In this system, perpendicular backbone and isotropic substituents attribute to the improvement of solubility and the easy formation of amorphous film, which enable the solution processing in device fabrication. The perpendicular spiro-conjugated π-systems also provide an advantage in light emitting device. In 2012, Adachi *et al.* demonstrated that spiro structure is effective scaffolds for thermally

activated delayed fluorescence (Figure 1.5),[20] where the spatial separation of HOMO and LUMO efficiently achieved thanks to perpendicular structure. By attaching electron donating and accepting groups on the different π-units on spiro-linkage respectively, they achieved the desired electronic structure and efficient TADF property. Since then, many researchers utilize spiro structure in TADF materials in order to construct appropriate electronic structures.[21]

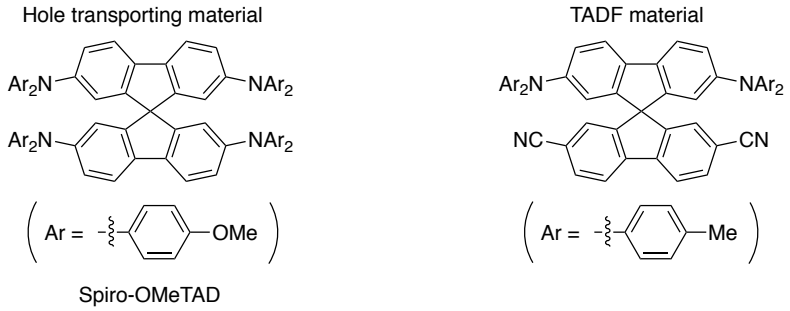

Figure 1.5. Examples of spiro compounds as organic semiconducting materials.

Spiro compounds are also applied as light-emitting scaffolds Intramolecular charge separation via spiro-linkage is utilized to environment-sensing dyes[22] and biological probes[23] as well. Moreover, in 2019, Casanova *et al.* computationally demonstrated that the regulation of electronic interaction between two conjugated system by spiro structure is potentially effective for the use in singlet fission materials.[24]

1.2.5. Chirality in spiro compounds

Spiro compounds can be chiral when the different units are introduced as π-units. Even if the two π-units are the same, it would evoke axial chirality when the π units are right-left asymmetric. Because the relative position of the two π-units are fixed via covalent bonds, the energetic barrier for racemization is generally high. Chiral spiro scaffold have been utilized in asymmetric synthesis[25] since von Baeyer utilized spiro structure for the backbone of axially chiral phosphorus ligands in 1900.[26] In 1992, Kumar *et al.* demonstrated asymmetric reduction reaction of ketones by using chiral *cis,cis*-spiro[4,4]nonane-1,6-diol as a chiral auxiliary to give the corresponding alcohols with good enantioselectivities (Scheme 1.2.).[27] The rigid and chiral backbone is also applied for molecular recognition as demonstrated by Alcazar *et al.* in 1992.[28]

Figure 1.6. Examples of chiral ligands based on spiro structures.

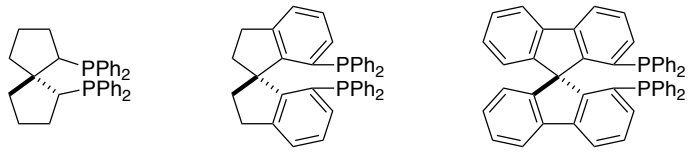

Scheme 1.2. Asymmetric reduction of ketones by using chiral spiro compounds reported by Kumar *et al*.

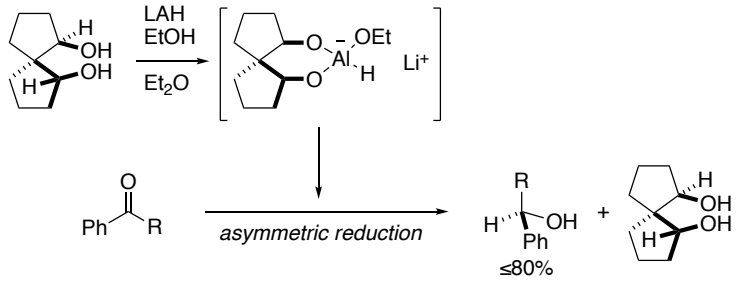

Optically, spiro compounds have been investigated on their optical rotation and circular dichroism (CD)[29] since the measurements on 9,9'-spirobifluorene derivatives reported by Haas *et al.* in 1969[30] and 1971 (Figure 1.7).[31] It was demonstrated that the absolute stereochemistry of spiro compounds can be determined from the sign of the CD band. Even though the investigation on CD of various spiro compounds had been performed, spiro compounds exhibiting circularly polarized luminescence (CPL), one of the attractive photonic phenomena due to potential applications such as display devices,[32] CPL lasers,[33] and biological probes,[34] had been demonstrated only in two papers , reported by Takai *et al.* and Nozaki *et al.,* until 2017.[35] Both of them described on silicon-bridged spiro compounds (Figure 1.8) synthesized via Rhodium-catalyzed reactions. While the photophysical properties were investigated, further development on these compounds for applications have never been conducted.

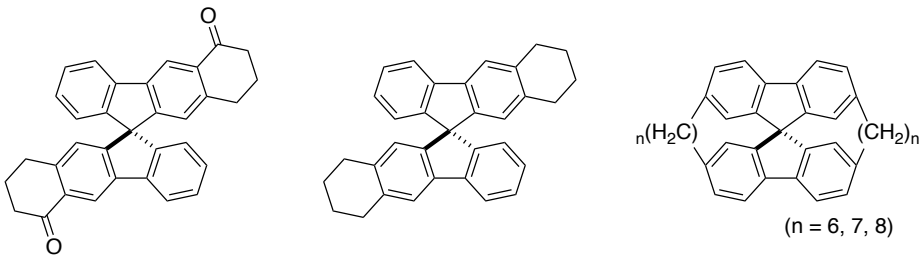

Figure 1.7. Examples of chiral spiro compounds investigated optical rotation and CD properties by Haas *et al*.

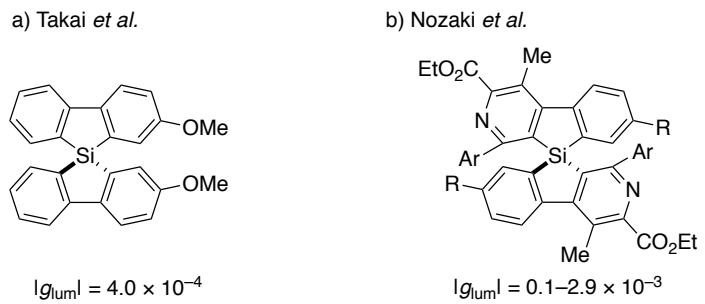

Figure 1.8. Examples of silicon-centered chiral spiro CPL compounds.

In 2017, Nakano *et al.* developed the first carbon-centered spiro CPL compounds based on thiophene and pyrrole (Figure 1.9).[36] The authors synthesized the thiophene-based one at first via nucleophilic addition of the corresponding dibromo benzothiophene and ester, followed by intramolecular Friedel-Crafts cyclization. They derivatized the initial spiro compounds by oxidation, addition of donor groups on the edges, and the transformation of thiophene into indole to study on their CPL properties. They also achieved the optical resolution by HPLC and solvatochromism in fluorescence. While a simple chiral spiro backbone had been desired for the potential of wide application, there still has been no other report. The development of new chiral spiro scaffolds are necessary to open up further applications.

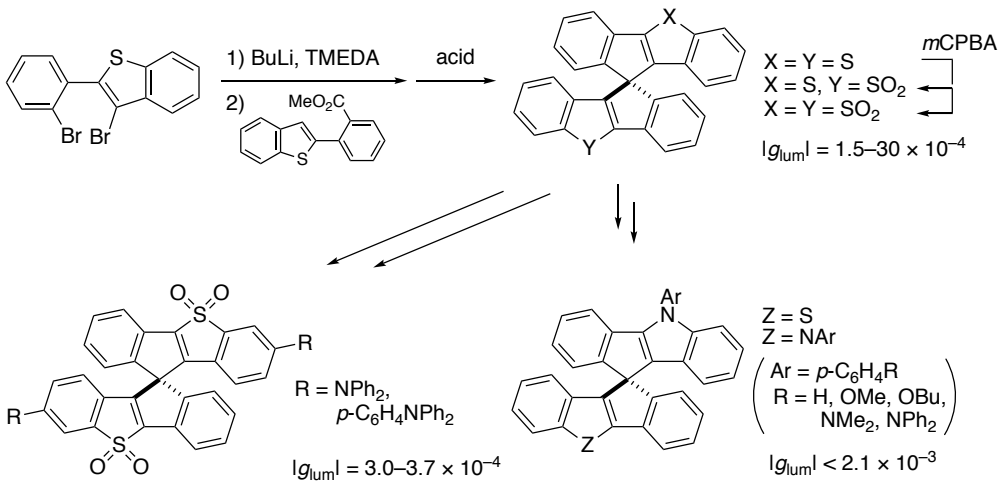

Figure 1.9. Chiral spiro CPL compounds reported by Nakano *et al.*

1.3. Thesis outline

Based on the concept that the fusion of molecular structure in one molecule enables to integrate material functions, or rather achieve new properties, I envisioned upgrading these structures toward the next dimension. In my doctoral course study, I focused on the investigation of two types of functional π-conjugated scaffolds designed by connection of planer π-conjugated systems via one or two carbon atoms as a spiro-linkage and an olefinoic linker.

In Chapter 2, I report the aggregation-responsive fluorescence switching behavior in tetrakis(benzo[*b*]furyl)ethene (**TBFE**, Figure 1.10a), which is initiated in my master course study and completed as a part of my Ph.D. study. **TBFE** was designed by combination of benzofuran units and an olefin linker and expected to exhibit both of aggregation-triggered photoluminescence and quenching because of incorporation of emissive benzo[*b*]furyl unit on tetraarylethene, a well-known aggregation-induced emission backbone. Three-stage two-wavelength on-off-on fluorescence switching was achieved in THF/H_2O mixed solvents, and its aggregation-triggered mechanism was supported by the investigation on photophysical and microscopic properties and size distributions. This work suggested me the efficiency of this design strategy and encouraged my developing a series of spiro-conjugated carbon-bridged *p*-phenylenevinylenes (spiro-CPVs), new spiro-conjugated carbocyclic scaffolds reported in Chapter 3–6. Spiro-CPV is designed by utilizing a bridging sp^3 carbon atom of COPV as a spiro center to connect two COPV units in perpendicular. In Chapter 3, the synthesis, optical resolution, and physicochemical properties of a simple spiro-CPV are reported (Figure 1.10b). Thanks to the rigid and axially chiral structure with spiroconjugation between two COPV units, spiro-CPV exhibited circularly polarized luminescence (CPL) with high stability and inter-subunit electron interaction. Chapter 4 describes the enhancement of radiative decay by π-elongation of spiro-CPV (Figure 1.10c). Radiative rate constant is ideally proportional to extinction coefficient.[37] Based on this idea, phenyl and phenylethynyl groups are attached on COPV units to intensify absorption. Photophysical study revealed that radiative decay is efficiently accelerated by π-elongation to achieve a fluorescence quantum yield of 0.99, the highest value for organic CPL molecules. In Chapter 5, the modification of electronic structure by the incorporation of heterocycle is reported (Figure 1.10d). The electronic properties changed due to electron donating and accepting effects of heteroatoms. Especially, the introduction of SO_2 group in the rigid and chiral spiro-CPV backbone caused intramolecular charge transfer upon photoexcitation to evoke solvatochromism in fluorescence.

Moreover, the linear correlation of a luminescence dissymmetry factor and solvent polarity was observed, which is rarely reported possibly because of large structural reorganizations causing randomization of dissymmetry factor. In Chapter 6, the development of spiro-CPV-based hole transporting materials (HTMs) is described (Figure 1.10e). Tetrakis(diarylamino) spiro-CPVs have appropriate energy levels for the use as HTM and higher amorphous state stabilities than spiro-OMeTAD,[38] a common hole transporting material. Spiroconjugation enabled inter-subunit electronic interactions in their radical cations, which enhances hole transfer in their spin-coated films by oxidant doping. These investigations proved that the integration of functional structures could be a strong strategy to design materials properties.

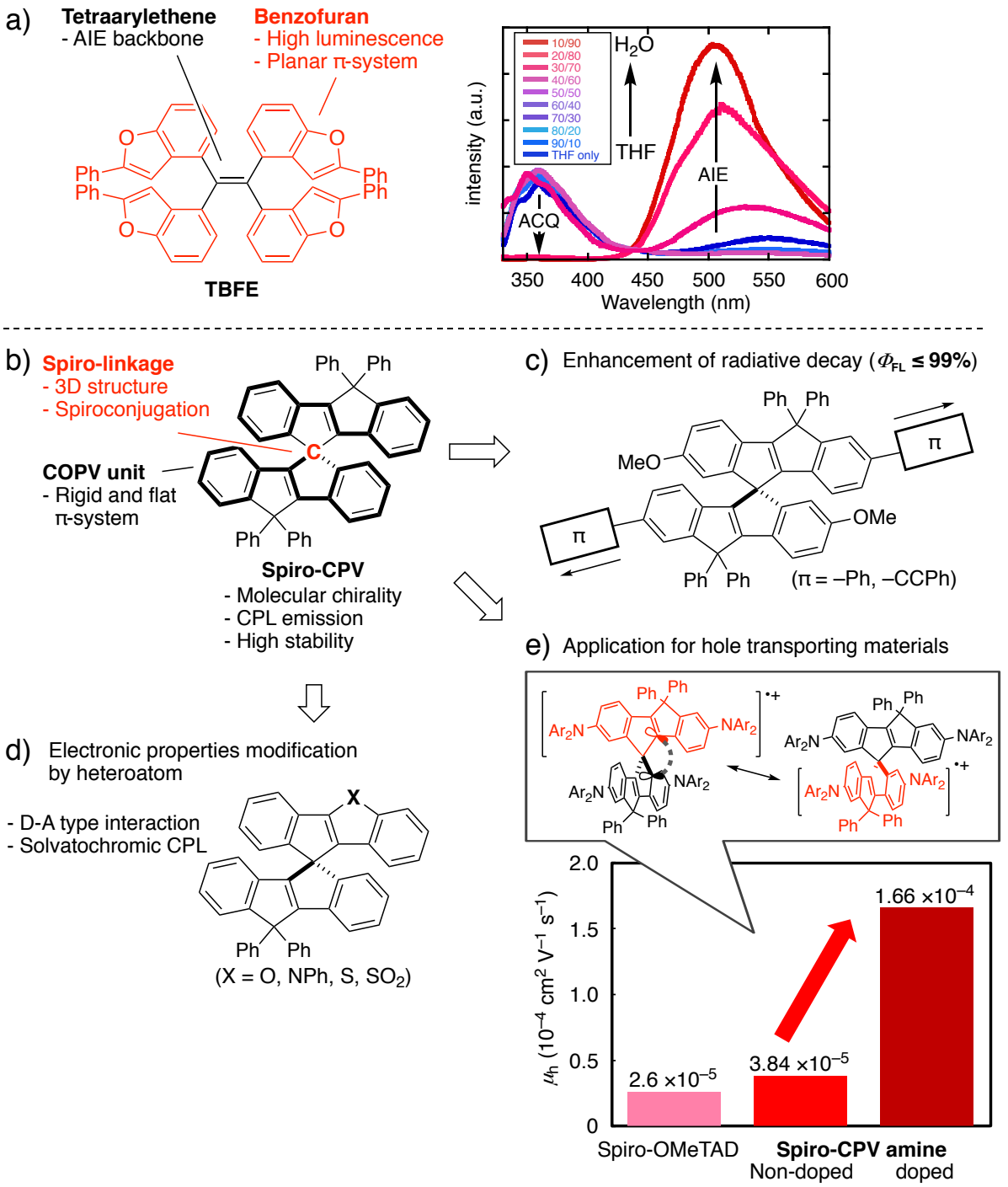

Figure 1.10. Overview of this thesis. a) **TBFE** for aggregation-triggered fluorescence switching. b) Spiro-CPV as a C_2-symmetric spiro-conjugated hydrocarbon. c) Photoluminescence enhancement for high quantum yield by expansion of π-system. d) Heteroatom-co-bridged spiro-CPV. e) Spiro-CPV-based hole transporting material for efficient carrier transport via spiroconjugation.

1.3. References

[1] (a) Vendrell, M.; Zhai, D.; Er, J. C.; Chang, Y.-T. *Chem. Rev.* **2012**, *112*, 4391–4420. (b) Guo, Z.; Park, S.; Yoon, J.; Shin, I. *Chem. Soc. Rev.* **2014**, *43*, 16–29. (c) Mei, J.; Leung, N. L. C.; Kwok, R. T. K.; Lam, J. W. Y.; Tang, B. Z. *Chem. Rev.* **2015**, *115*, 11718–11940.

[2] (a) Samuel, I. D.; Turnbull, G. A. *Chem. Rev.* **2007**, *107*, 1272–1295. (b) Anthony, J. E. *Angew. Chem. Int. Ed.* **2008**, *47*, 452–483.

[3] Abe, M. *Chem. Rev.* **2013**, *113*, 7011–7088.

[4] (a) Scherf, U. *J. Mater. Chem.* **1999**, *9*, 1853–1864. (b) Grimsdale, A. C.; Müllen, K. *Macromol. Rapid Commun.* **2007**, *28*, 1676–1702. (c) Tsuji, H.; Nakamura, E. *Acc. Chem. Res.* **2019**, *52*, 2939–2949.

[5] (a) Novoselov, K. S.; Geim, A. K.; Morozov, S. V.; Jiang, D.; Zhang, Y.; Dubonos, S. V.; Grigorieva, I. V.; Firsov, A. *Science* **2004**, *306*, 666−669. (b) Geim, A. K. *Science* **2009**, *324*, 1530−1534.

[6] (a) Shen, Y.; Chen, C.-F. *Chem. Rev.* **2012**, *112*, 1463–1535. (b) Rickhaus, M.; Mayor, M.; Juriček, M. *Chem. Soc. Rev.* **2017**, *46*, 1643–1660. (c) Saito, M.; Shinokubo, H.; Sakurai, H. *Mater. Chem. Front.* **2018**, *2*, 635–661.

[7] (a) Bühl, M.; Hirsch, A. *Chem. Rev.* **2001**, *101*, 1153–1183. (b) Umeyama, T.; Imahori, H. *Acc. Chem. Res*. **2019**, *52*, 2046–2055.

[8] (a) Fukazawa, A.; Yamaguchi, S. *Chem. Asian J.* **2009**, *4*, 1386–1400. (b) Hirai. M.; Tanaka, N.; Sakai, M.; Yamaguchi, S. *Chem. Rev*. **2019**, *119*, 8291–8331. (c) Stępien, M.; Gonḱa, E.; Żyła, M.; Sprutta, N. *Chem. Rev.* **2017**, *117*, 3479–3716.

[9] Tsuji, H.; Nakamura, E. *Acc. Chem. Res.* **2017**, *50*, 396–406.

[10] (a) Nishioka, H.; Tsuji, H.; Nakamura, E. *Macromolecules* **2018**, *51*, 2961–2968. (b) Morales-Vidal, M.; Quintana, J. A.; Villalvilla, J. M.; Boj, P. G.; Nishioka, H.; Tsuji, H.; Nakamura, E.; Whitworth, G. L.; Turnbull, G. A.; Samuel, I. D. W.; Díaz-García, M. A. *Adv. Opt. Mater.* **2018**, *6*, 1800069.

[11] (a) Salbeck, J.; Yu, N.; Bauer, J.; Weissörtel, F.; Bestgen, H. *Synth. Met.* **1997**, *91*, 209–215. (b) Saragi, T. P. I.; Spehr, T.; Siebert, A.; Fuhrmann-Lieker, T.; Salbeck, J. *Chem. Rev*. **2007**, *107*, 1011–1055.

[12] Saragi, T. P. I.; Fuhrmann-Lieker, T.; Salbeck, J. *Adv. Funct. Mater*. **2006**, *16*, 966–974.

[13] Hoffmann, R.; Imamura, A.; Zeiss, G. D. *J. Am. Chem. Soc*. **1967**, 89, 5215–5220.

[14] Simmons, H. E.; Fukunaga, T. *J. Am. Chem. Soc*. **1967**, *89*, 5208–5215.

[15] (a) Schweig, A.; Weidner, U.; Hill, R. K.; Cullison, D. A. *J. Am. Chem. Soc*. **1973**, *95*, 5426–5427. (b) Schweig, A.; Weidner, U.; Hellwinkel, D.; Krapp, W. *Angew. Chem. Int. Ed.* **1973**, *89*, 310–311.

[16] Sowa, J. K.; Mol, J. A.; Briggs, G. A. D.; Gauger, E. M. *J. Phys. Chem. Lett.* **2018**, *9* 1859–1865.

[17] Clarkson, R. G.; Gomberg, M. *J. Am. Chem. Soc.* **1930**, *52*, 2881–2891.

[18] Cheng, X.; Hou, G.-H.; Xie, J.-H.; Zhou, Q.-L. *Org. Lett.* **2004**, *14*, 2381–2383.

[19] (a) Bach, U.; Lupo, D.; Comte, P.; Moser, J. E.; Weissörtel, F.; Salbeck, J.; Spereitzer, H.; Grätzel, M. *Nature* **1998**, *395*, 583–585. (b) Hawash, Z.; Ono, L. K.; Qi, Y. *Adv. Mater. Interfaces,* **2018**, *5*,1700623. (c) Jeon, N. J.; Lee, H. G.; Kim, Y. C.; Seo, J.; Noh, J. H.; Lee, J.; Seok, S. I. *J. Am. Chem. Soc*. **2014**, *136*, 7837–7840. (d) Gao, G.; Liang, N.; Geng, H.; Jiang, W.; Fu, H.; Feng, J.; Hou, J.; Feng, X.; Wang, Z. *J. Am. Chem. Soc*. **2017**, *139*, 15914–15920. (e) Urieta-Mora, J.; Garcia-Benito, I.; Molina-Ontoria, A.; Martín N. *Chem. Soc. Rev*. **2018**, *47*, 8541–8571.

[20] Nakagawa, T.; Ku, S.-Y.; Wong, K.-T.; Adachi, C. *Chem. Commun.* **2012**, *48*, 9580–9582.

[21] (a) Yang, Z.; Mao, Z.; Xie, Z.; Zhang, Y.; Liu, S.; Zhao, J.; Xu, J.; Chi, Z.; Aldred, M. P. *Chem. Soc. Rev.* **2017**, *46,* 915–1016. (b) Tao, Y.; Yuan, K.; Chen, T.; Xu, P.; Li, H.; Chen, R.; Zheng, C.; Zhang, L.; Huang, W. *Adv. Mater.* **2014**, *26*, 7931–7958. (c) Im, Y.; Kim, M.; Cho, Y. J.; Seo, J.-A. ; Yook, K. S.; Lee, J. Y. *Chem. Mater.* **2017**, *29*, 1946–1963.

[22] Mei, J.; Leung, N. L. C.; Kwok, R. T. K.; Lam, J. W. Y.; Tang, B. Z. *Chem. Rev*. **2015**, *115*, 11718–11940.

[23] Yuan, L.; Lin, W.; Zheng, K.; Zhu, S. *Acc. Chem. Res.* **2013**, *46*, 1426–1473.

[24] (a) Sandoval-Salinas, M. E.; Carreras, A.; Casado, J.; Casanova, D. *J. Chem. Phys*. **2019**, *150*, 204306. (b) Kumarasamy, E.; Sanders, S. N.; Tayebjee, M. J. Y.; Asadpoordarvish, A.; Hele, T. J. H.; Fuemmeler, E.G.; Pun, A. B.; Yablon, L. M.; Low, J. Z.; Paley, D. W.; Dean, J. C.; Choi, B.; Scholes, G. D.; Steigerwald, M. L.; Ananth, N.; McCamey, D. R.; Sfeir, M. Y.; Campos, L. M. *J. Am. Chem. Soc*. **2017**, *139*, 12488–12494.

[25] Xie, J.-H.; Zhou, Q. L. *Acc. Chem. Res.* **2008**, *41*, 581–593.

[26] von Baeyer, A. P. *Ber. Dtsch. Chem. Ger.* **1900**, *33*, 3771–3775.

[27] Srivastava, N.; Mital, A.; Kumar, A. *Chem. Commun*. **1992**, 493–494.

[28] Alcazar, V.; Diederich, F. *Angew. Chem., Int. Ed. Engl.* **1992**, *31*, 1521−1523.

[29] (a) Prelog, V.; Bedekovic, D. *Helv. Chim. Acta* **1979**, *62*, 2285–2303. (b) Harada, N.; Ono, H.; Nishiwaki, T.; Uda, H. *J. Chem. Soc., Chem. Commun.* **1991**, 1753−1755.

[30] Haas, G.; Prelog, V. *Helv. Chim. Acta.* **1969**, *52*, 1202−1218.

[31] Haas, G.; Hulbert, P. B.; Klyne, W.; Prelog, V.; Snatzke, G. *Helv. Chim. Acta,* **1971**, *54*, 491–509.

[32] Schadt, M. *Annu. Rev. Mater. Sci.* **1997**, *27*, 305–379. (b) Peeters, E; Christiaans, M. P. T.; Janssen, R. A. J.; Schoo, H. F. M.; Dekkers, H. P. J. M.; Jeijer, E. W. *J. Am. Chem. Soc.* **1997**, *119*, 9909– 9910. (c) Grell, M.; Oda, M.; Whitehead, K. S.; Asimakis, A.; Neher, D.; Bradley, D. D. C. *Adv. Mater.* **2001**, *13*, 577–580.

[33] (a) Chen, F.; Gindre, D.; Nunzi, J. M. *Opt. Express*, **2008**, *16*, 16746–16753. (b) Furumi, S. *Chem. Rec*. **2010**, *10*, 394–408. (c) Cerdán, L.; Moreno, F.; Johnson, M.; Muller, G.; Moya, S. D. L.; Garcia-Moreno, I. *Phys. Chem. Chem. Phys*. **2017**, *19*, 22088–22093.

[34] (a) Carr, R.; Evans, N. H.; Parker, D. *Chem. Soc. Rev.* **2012**, *41*, 7673–7686. (b) Heffern, M. C.; Matosziuk, L. M.; Meade, T. J. *Chem. Rev.* **2014**, *114*, 4496–4539.

[35] (a) Murai, M.; Takeuchi, Y.; Yamauchi, K.; Kuninobu, Y.; Takai, K. *Chem. – Eur. J.* **2016**, *22*, 6048–6058. (b) Shintani, R.; Misawa, N.; Takano, R.; Nozaki, K.; *Chem. – Eur. J.* **2017**, *23*, 2660–2665.

[36] (a) Takase, K.; Noguchi, K.; Nakano, K. *Org. Lett*. **2017**, *19*, 5082–5085. (b) Takase, K.; Noguchi, K.; Nakano, K. *J. Org. Chem*. **2018**, *83*, 15057–15065. (c) Takase, K.; Noguchi, K.; Nakano, K. *Bull. Chem. Soc. Jpn.* **2019**, *92*, 1008–1017.

[37] (a) Strickler, S. J.; Berg, R. A. *J. Chem. Phys.* **1962**, *37*, 814–822. (b) Ware, W. R.; Baldwin, B. A. *J. Chem. Phys*. **1964**, *40*, 1703–1705.

[38] Bach, U.; Lupo, D.; Comte, P.; Moser, J. E.; Weissörtel, F.; Salbeck, J.; Spereitzer, H.; Grätzel, M. *Nature* **1998**, *395*, 583–585.

Chapter 2.

Tetrakis(benzo[*b*]furyl)ethene (TBFE) : Combination of Aggregation-responsive Fluorescent Behaviors

This work was initiated during my master thesis study,
and completed as a part of the Ph.D. study.

2.1. Introduction

2.1.1. Aggregation-responsive fluorescence

Aggregation-responsive fluorescence is one of the properties derived from molecular structure. In 2001, Tang *et al.* first reported aggregation-induced emission of 1-methyl-1,2,3,4,5-pentaphenylsilole, [1] where the solid-state emission is enhanced by aggregation causing the inhibition of intramolecular rotation and planarization of phenyl substituents. Since then, these aggregation-responsive phenomena have been an attractive environment-responsivity because of its potential applications[2] such as light emitting devices and environmental sensors. There are mainly two kinds of aggregation-responsive fluorescent behaviors (Figure 2.1): aggregation-caused quenching (ACQ) and aggregation-induced emission (AIE), both of which are attributed to molecular structures. ACQ materials, which are generally planer π-conjugated molecules,[3] exhibit fluorescence with high quantum yield (Φ_{FL}) in diluted solution where the intermolecular interaction is inhibited, while the quantum yields largely decrease by aggregation because of nonradiative deactivations mainly caused by intermolecular π–π interaction and charge transfer. In contrast, AIE materials, such as tetraarylethenes (TAEs),[4] undergo the quenching of photoemission due to intramolecular rotation or vibration, whereas the deactivation processes are inhibited by aggregation to result in intense luminescence. Previously, two-stage on-off fluorescence switching has been demonstrated just by utilizing ACQ of AIE system. Though three-stage on-off-on switching[5] has been also achieved by a combination of AIE and intramolecular charge transfer (ICT) that causes continuous peak shift during switching, three-stage switching at discrete wavelength is still challenging.

I envisioned that the three-stage on-off-on fluorescence switching at different wavelengths could be achieved by designing a molecule with both of ACQ and AIE moieties. I hypothesized that ACQ and AIE properties could be integrated in one molecule by incorporating ACQ units in AIE backbone. For this molecule, it is expected to show photoluminescence from an ACQ unit in solution. On the other hand, in aggregated state, the AIE backbone would activate photoemission, while the luminescence from an ACQ unit is quenched in aggregated state. Because these two processes are not involved to charge transfer, wavelength shift by ICT would not be brought on.

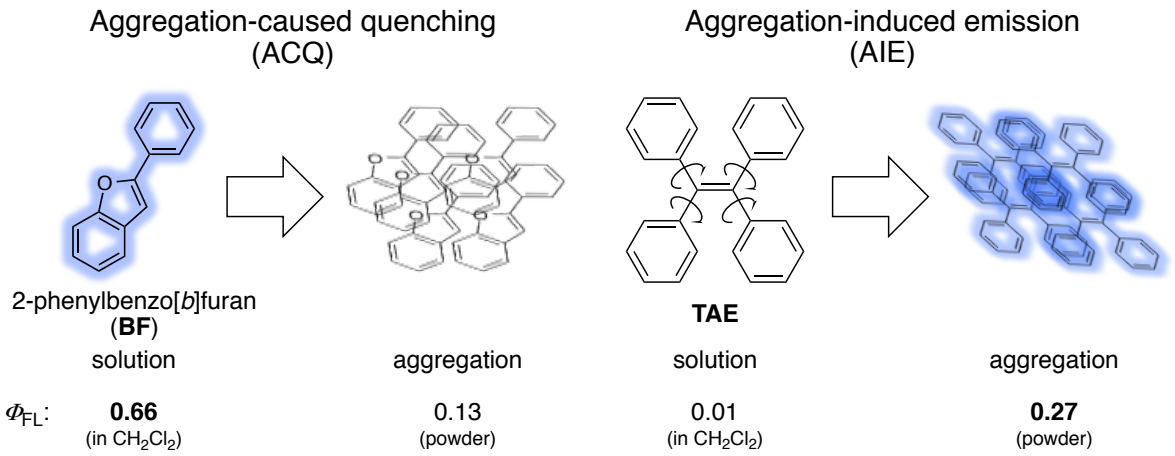

Figure 2.1. Schematic images of ACQ and AIE.

2.1.2. Tetrakis(benzo[*b*]furyl)ethene for combination of ACQ and AIE: Chapter outline

Based on this idea, tetrakis(benzo[*b*]furyl)ethene (**TBFE**, Figure 2.2), was designed by introducing a benzofuryl unit,[6] an emissive π-plane, as a subunit of TAE, a common AIE backbone. During my master course study, I have synthesized **TBFE** by developing a hafnium-mediated McMurry-type coupling reaction,[7] which was suggested to be effective for bulky ketone substrates due to a large atomic radius and a large standard electrode potential of hafnium. In this chapter, the investigation of fluorescence switching behavior of **TBFE** upon aggregation is reported. In Section 2.2, the synthesis of **TBFE** is briefly described. Section 2.3 describes the two-wavelength on-off-on fluorescence switching at first, followed by the insights of mechanism based on photophysical investigation and studies on size distribution. Section 2.4 provides the summary of this work.

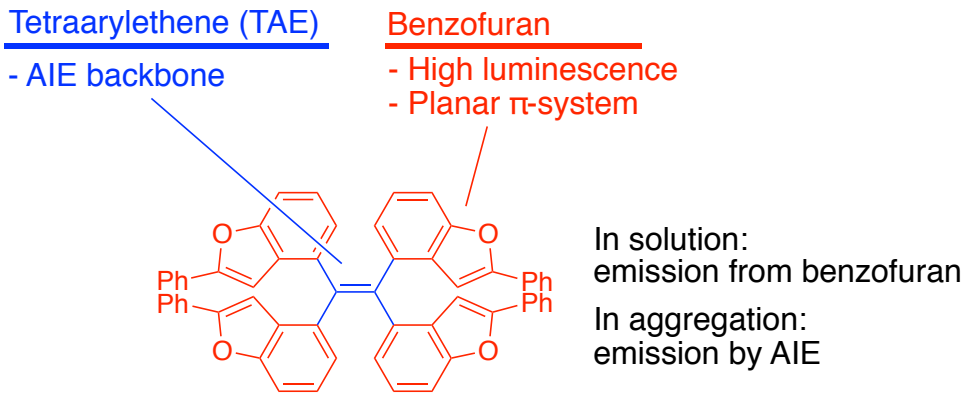

Figure 2.2. Molecular design of **TBFE** for an aggregation-responsive fluorescent material.

2.2. Synthesis

By following the previous synthetic procedure,[7] **TBFE** was synthesized via hafnium-mediated McMurry coupling reaction. Firstly, 4-bromobenzo[*b*]furan (**5**) was synthesized via the procedure reported by Sanz *et al.,*[8] followed by converting into di(benzo[b]furyl)ketone (**3**) in 2 steps. Then, **TBFE** was obtained by McMurry-type coupling of **3** with the use of hafnium chloride (Scheme2.1). Inspired by the procedure reported by Mukaiyama *et al.*,[9] metallic Zn was chosen as reducing reagent.

Noteworthily, the McMurry coupling reaction did not take place at all with the use of titanium chloride, a conventional reagent for McMurry reaction, while the use of zirconium chloride or hafnium chloride afforded the desired product (Table 2.1). I ascribed the difference of reactivity to their atomic radius and redox potentials. Considering Ti-mediated McMurry coupling is inactive for bulky ketone substrates,[10] the larger Hf and Zr radius in low-valent metals than Ti might reduce a steric hindrance between substrates to promote the coupling. Higher standard reduction potentials (M^{4+}/M) would also enhance the reaction by activating the deoxygenation step.

Scheme 2.1. Synthesis of **TBFE**.

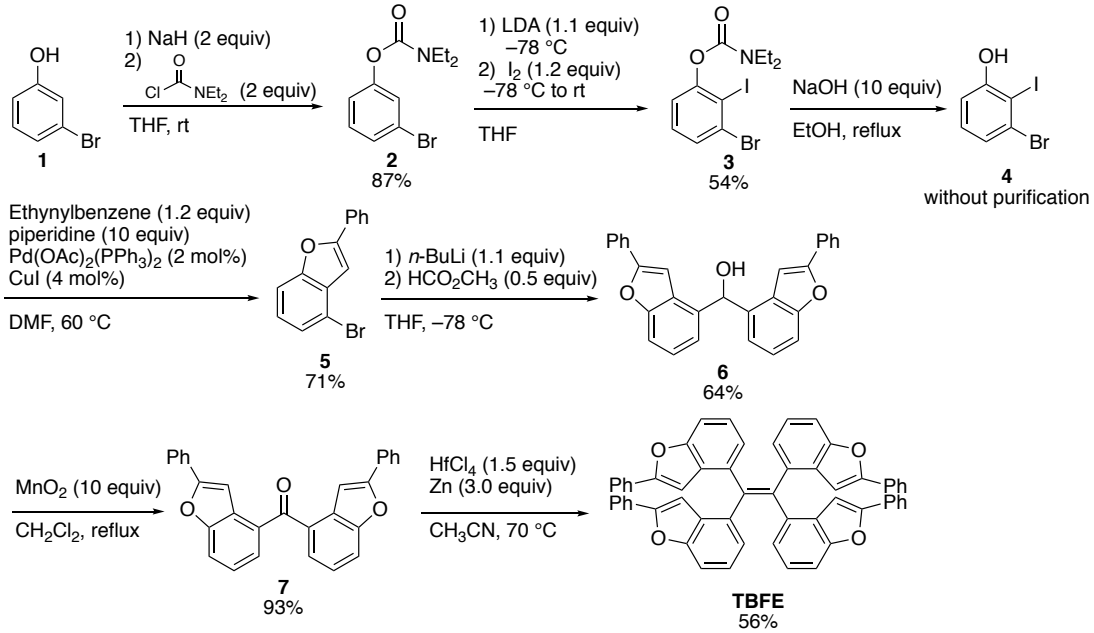

Table 2.1. McMurry-type coupling reaction of **7** mediated by group 4 metals.

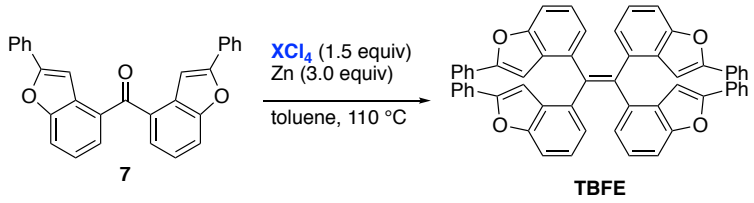

7 **TBFE**

XCl_4	r^a (pm)	$E_{M^{4+}/M}{}^b$ (V)	Yield (%)
$TiCl_4$	148	–1.37	0
$ZrCl_4$	164	–1.45	42
$HfCl_4$	164	–1.55	50

[a] Atomic radius of metal.[11] [b] Standard reduction potentials.[11]

2.3. Fluorescence switching upon aggregation

2.3.1. Photophysical properties

In order to investigate aggregation responsivity of **TBFE**, I firstly measured absorption and fluorescence spectra in THF/H_2O solvent systems. **TBFE** showed the maximum absorption peak at 317 nm in pristine THF, and no wavelength change was observed upon the change of THF/H_2O volume ratios from 0% (pure THF) to 90% of H_2O (Figure 2.3a). On the other hand, fluorescence spectra exhibited on-off and off-on fluorescence switching at the difference wavelength (Figure 2.3b, 2.4). Fluorescence peak was observed at the wavelength (λ_{FL}) of 360 nm in pure THF (blue line) with Φ_{FL} of 0.094. Addition of H_2O decreased the emission peak without any wavelength shift to reach Φ_{FL} of 0.028 at 40% H_2O solvent (reddish purple line). Further addition of H_2O caused the emergence of a new and broad emission peak at 530 nm (Φ_{FL} = 0.159) at 70% H_2O, and intensification of the peak up to Φ_{FL} = 0.263 at 90% H_2O with a gradual hypsochromic shift to λ_{FL} = 503 nm. The peak at 360 nm was totally disappeared at 80–90% H_2O solvents. Considering that no bathochromic shift of the 360 nm peak was observed at 0–40 % H_2O solvents, this on-off-on fluorescence switching is not involved to ICT process, generally accompanied by a redshift,[5] but is triggered by aggregation: ACQ at 360 nm and AIE at 510 nm. The hypsochromic shift seen in 70–90 % H_2O solution is probably because of the hydrophobic environment in the aggregation. Addition of H_2O make aggregation densely and remove solvent molecules from aggregation particles. In the other words, the dense aggregation by H_2O addition changes the surroundings of a **TBFE** molecule in aggregation from polar solvents to non-polar **TBFE**.

This make the inside of aggregation more hydrophobic and cause the blue-shift of fluorescence.

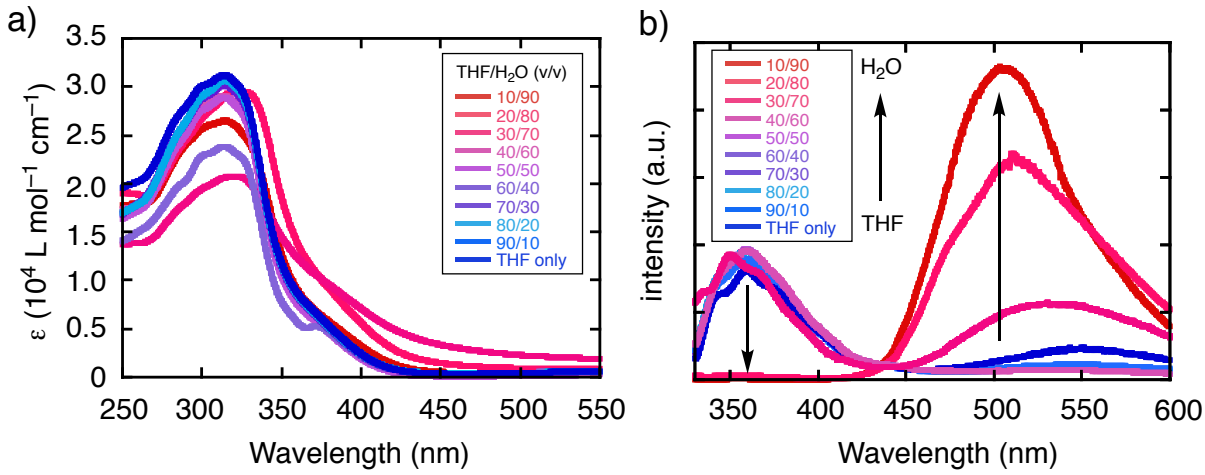

Figure 2.3. Photophysical properties of **TBFE** in THF/H_2O mixed solvent system. a) Absorption spectra (1.0×10^{-5} M). b) Fluorescence spectra (1.0×10^{-6} M).

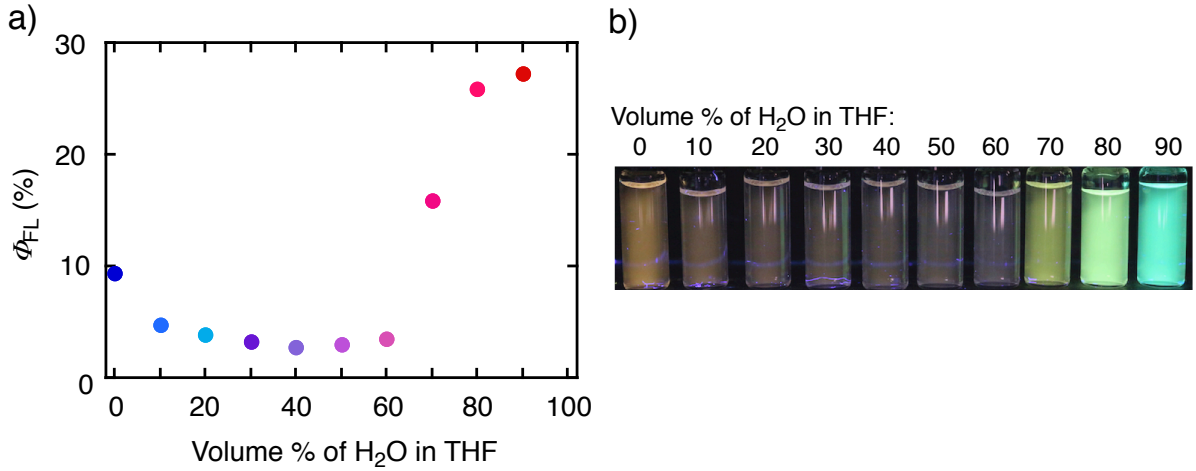

Figure 2.4. a) Φ_{FL}s of **TBFE** in THF/H_2O mixed solvent system (1.0×10^{-6} M). b) Photograph of **TBFE** in THF/H_2O mixed solvent system under 365 nm light irradiation.

Table 2.2. λ_{abs}, λ_{FL}, and Φ_{FL} of **TBFE** in THF/H_2O mixed solvents and 2-phenylbenzo[*b*]furan (**BF**) in THF.

THF/H_2O (v/v)	λ_{abs}[a] (nm)	λ_{FL}[b] (nm)	Φ_{FL}[c]
10/90	322	503	0.273
20/80	322	510	0.259
30/70	320	351/530	0.159
40/60	313	360	0.035
50/50	313	360	0.030
60/40	313	360	0.028
70/30	314	359	0.033
80/20	314	360	0.039
90/10	314	360	0.048
100/0	314	359	0.094
BF in THF	304	343	0.656

[a] The maximum absorption wavelength. [b] Fluorescence wavelength. [c] Fluorescence quantum yield determined by using the absolute method.

Further investigation of photophysical properties gave the insight on the mechanism of this fluorescence switching behavior. I measured absorption and fluorescence spectra of 2-phenylbenzo[*b*]furan (**BF**) in THF, and compared to those of **TBFE** (Figure 2.5, Table 2.2 bottom). The maximum absorption peak of **TBFE** was observed at λ_{abs} = 314 nm, while that of **BF** was at 304 nm. This similarity indicates that the electronic structure of **TBFE** in ground state concerning to absorption is attributed to a **BF** unit. Structural optimization at the B3LYP/6-31G(d) level of theory gave five conformational isomers within the small energetic difference of 4.28 kJ mol^{-1} (Figure 2.12–16 in Section 2.5). In the most stable isomer (Figure 2.14 in Section 2.5), **BF** units and the central ethenyl unit formed the torsion angle of 87.8° for each. This suggests the small electronic interaction of between each π-units to support the similarity of electronic property for **TBFE** and **BF** in their ground state. The broadness of the spectrum of **TBFE** might reflect the conformational isomers.

Fluorescence spectra of **TBFE** and **BF** showed with similar spectral configuration (Figure 2.5). It suggested that **BF** units attribute fluorescence of **TBFE** in THF, and structural conformation

hardly affects. Bathochromic shift by 16 nm was observed in **TBFE** compared to **BF**, which is possibly due to the ethenyl group that elongates π-conjugation of the furyl units in excited state.

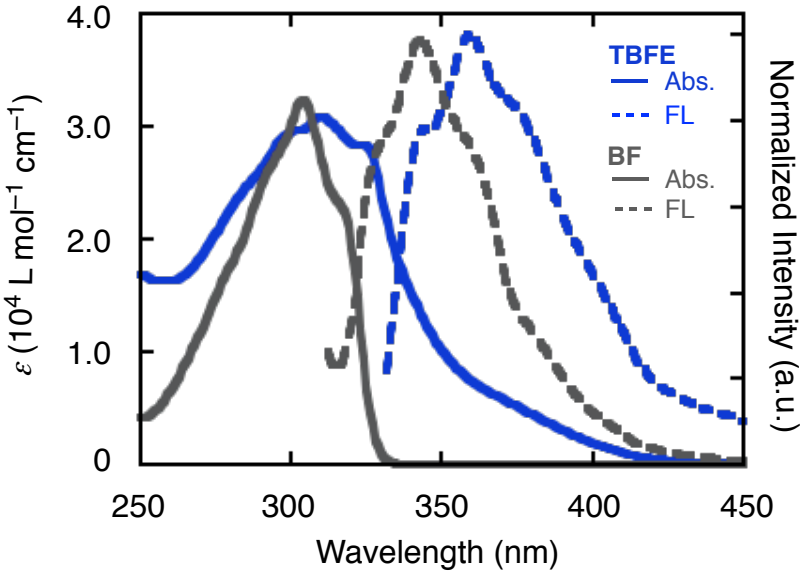

Figure 2.5. Absorption and fluorescence spectra of **TBFE** and 2-phenylbenzofuran (**BF**) in THF (1.0×10^{-5} M for absorption and 1.0×10^{-6} M for fluorescence).

The radiative and nonradiative rate constants (k_r and k_{nr}) in THF/H_2O mixed solvents (0, 50, 70, 90% H_2O) provided further insights on the fluorescence switching behavior. Both of k_r and k_{nr} were determined from average fluorescence lifetime ($<\tau>$) and Φ_{FL} (Table 2.3). The change of k_{nr} upon addition of H_2O was not observed in 0–50% H_2O (k_{nr} = 7.51–7.23 × 10^8 s^{-1}). At 70% H_2O, where the fluorescence intensification at 510 nm was observed, k_{nr} dramatically decreased to 5.15 × 10^8 s^{-1}. Further addition of H_2O resulted smaller k_{nr} of 2.52 × 10^8 s^{-1} at 90% H_2O. Considering that AIE process generally shows the significant decrease of k_{nr},[12] I accredited the fluorescence intensification at 510 nm to AIE process of **TBFE**.

Lower Φ_{FL} of **TBFE** in pure THF (0.094), compared to that of **BF** (0.656), is attributable to fast nonradiative decay and slow radiative decay of **TBFE** possibly due to structural flexibility around C–C single bonds connecting **BF** units and the central ethenyl structure. The k_{nr} at 90% H_2O, where **TBFE** is aggregated, was quite similar to that of **BF** in THF. This also implies the attribution of intramolecular rotation. The large k_{nr} at 70% H_2O indicates that **TBFE** molecules are not so densely aggregated as at 90% H_2O to allow some nonradiative deactivations.

A biexponential function fitting was used for the fluorescence decay curves at 70–90% H_2O (Table 2.4), while a monoexponential function was used for the fitting at 0–50%. This difference indicates that **TBFE** forms two conformers in aggregated state (70–90% H_2O) because of the suppression of the free rotation of **BF** units.

Table 2.3. Photophysical properties of **TBFE** and **BF**.

	TBFE				**BF**
	THF	THF/H_2O (50/50)	(30/70)	(10/90)	THF
Φ_{FL}[a]	0.094	0.050	0.159	0.273	0.656
$<\tau>$[b] (ns)	1.21	1.31	1.63	2.89	1.18
k_r[c] (10^7 s^{-1})	7.79	3.81	9.74	9.46	55.4
k_{nr}[d] (10^8 s^{-1})	7.51	7.23	5.15	2.52	2.91

[a] Fluorescence quantum yield determined using the absolute method. [b] Average fluorescence lifetime. [c] Radiative rate constant. [d] Nonradiative rate constant.

Table 2.4. Fluorescence lifetime of **TBFE** in THF/H_2O (70% and 90% H_2O).

THF/H_2O (v/v)	$<\tau>$[a] (ns)	τ_1[b] (ns)	Amp.$_1$[c]	τ_2[b] (ns)	Amp.$_2$[c]
30/70	1.63	0.382	120.6	2.56	24.4
10/90	2.89	3.58	166.1	1.03	128.2

[a] Average fluorescence lifetime. [b] Fluorescence lifetime of each component. [c] Amplitude of each component.

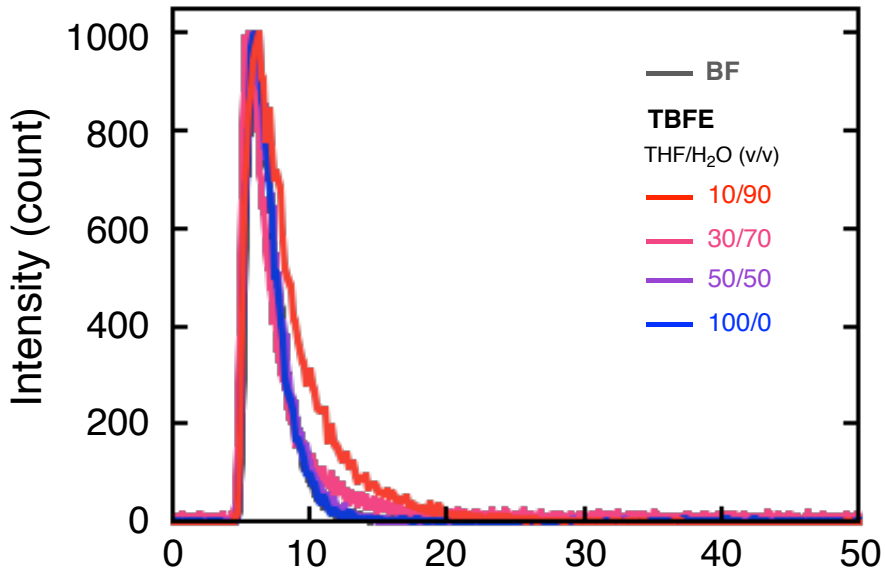

Figure 2.6. Fluorescence lifetime of **TBFE** in THF/H_2O mixed solvents and **BF** in THF (1.0×10^{-6} M).

2.3.2. Dynamic light scattering (DLS)

In order to understand the aggregation behavior, I conducted dynamic light scattering (DLS) measurement. The size distribution of **TBFE** particles changed upon H_2O addition to follow the fluorescence switching behavior (Figure 2.7). This result supports the fluorescence switching is triggered by aggregation. The size of **TBFE** particles in 0–50% H_2O are distributed on the small size region less than 10 nm, suggesting that molecules are totally dissolved to exist in units of one or a few molecules. In 60% H_2O, where the fluorescence is still off, the significant increase of size distribution to 4.8×10^3 nm was observed, and further H_2O addition (70–90% H_2O) caused the gradual size decrease to 8.3×10^2 nm. The large size in 60% H_2O and the following size decrease are possibly due to the aggregation density (Figure 2.8): the **BF** units is not adequately fixed in 60% to show similar fluorescence property to 0–50% solvents, while more aqueous environment in 70–90% make aggregates more densely by surface tension [13] to activate AIE process and cause the small hypsochromic fluorescent shift observed in Figure 2.3..

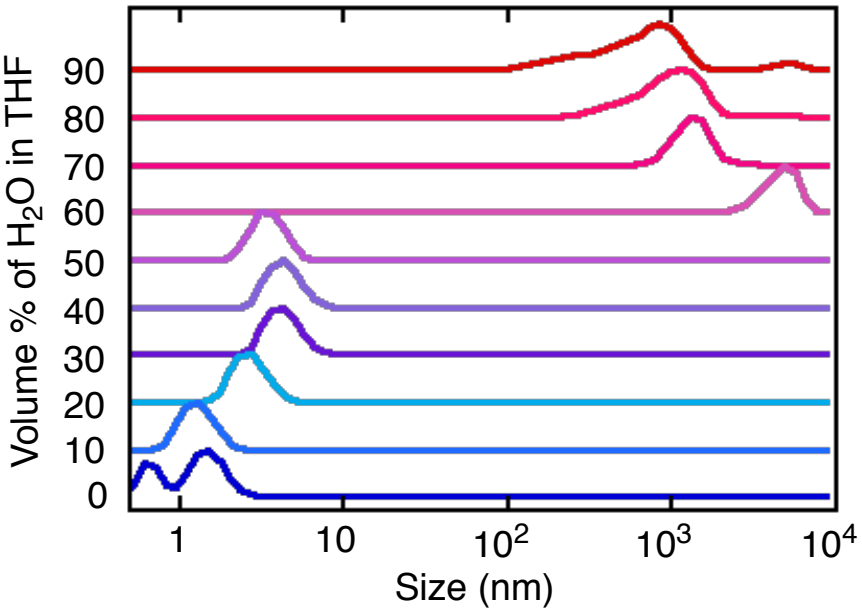

Figure 2.7. Size distribution of **TBFE** particles in THF/H_2O mixed solvents measured by DLS. The obtained correlation functions were outputted as a volume distribution.

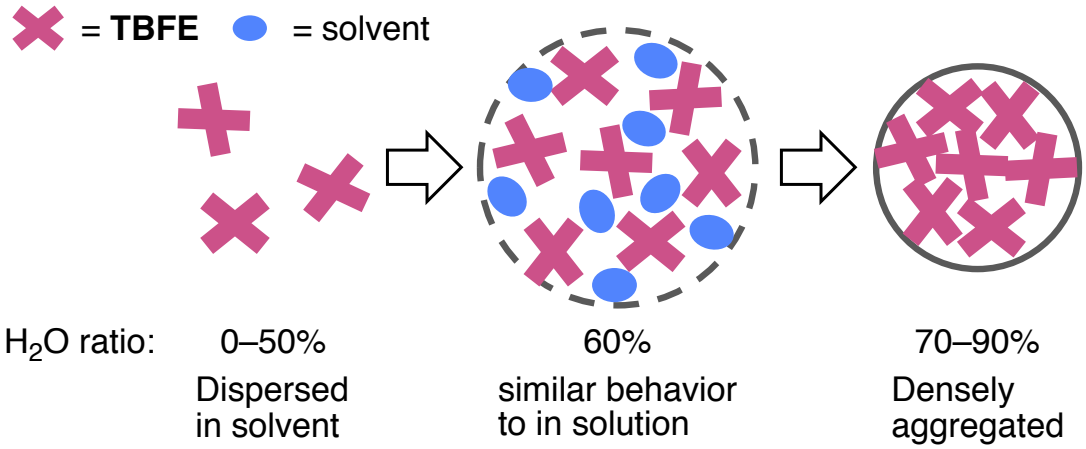

Figure 2.8. Schematic image of aggregation state of **TBFE** in THF/H_2O mixed solvents.

2.3.3. Microscopic study

The microscopic observation on scanning electron microscopy (SEM) supported the aggregation-induced fluorescence switching behavior (Figure 2.9, 2.10). The spin-coated **TBFE** in 90% H_2O solvent on ITO showed spherical aggregates, while only amorphous areas are observed for the corresponding sample from THF solution. The diameters of observed aggregates were 50–300 nm that is generally consistent with the results of DLS (Figure 2.7). In addition, the X-ray diffraction pattern of the aggregates in 90% H_2O did not show any sharp peak, indicating that the molecules form amorphous aggregates (Figure 2.11).

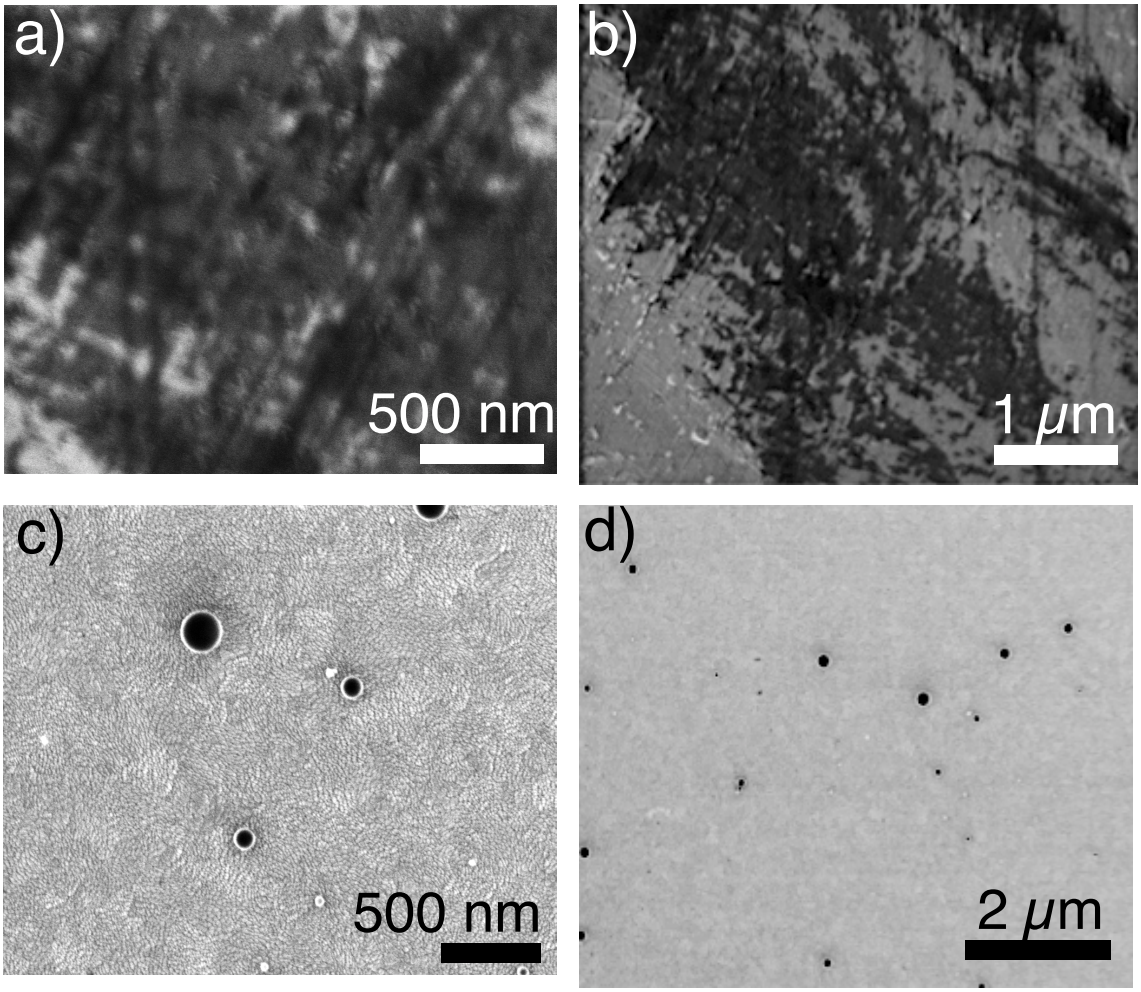

Figure 2.9. SEM images of **TBFE** spin-coated on ITO surface: a, b) THF solution, and c, d) 90% H_2O solution.

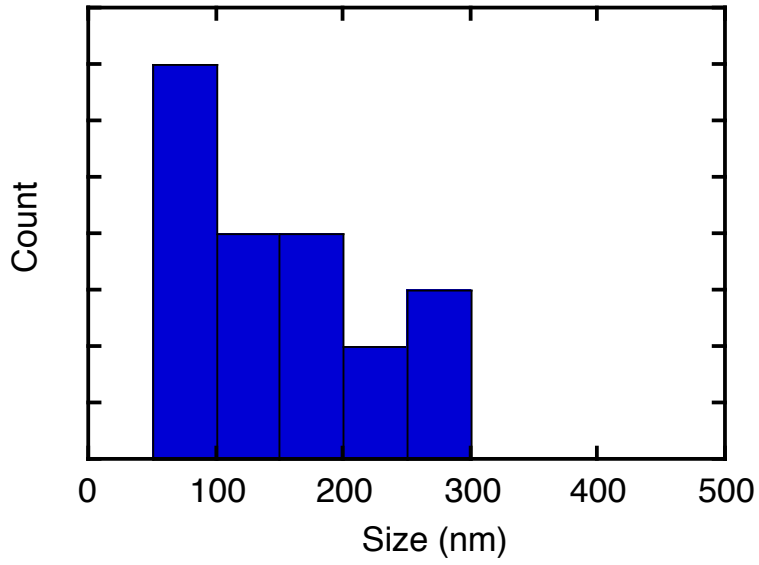

Figure 2.10. Histogram on the diameters of **TBFE** aggregates in 90% H_2O observed in Figure 2.9d.

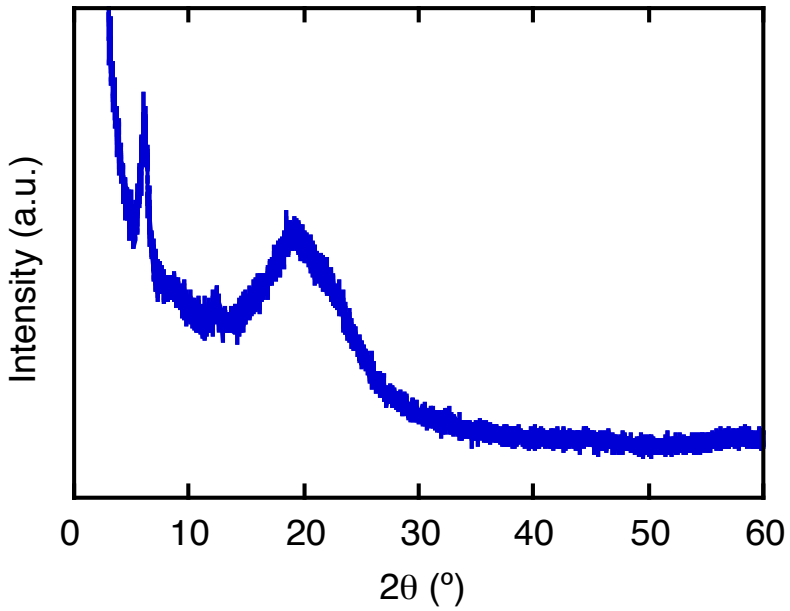

Figure 2.11. XRD pattern of the powder of **TBFE** aggregates obtained from 90% H_2O solution.

2.4. Summary

In summary, I investigated the aggregation-induced fluorescence switching behavior of **TBFE** where emissive **BF** units are utilized as subunits of TAE. Upon addition of H_2O into THF solution, fluorescence spectra of **TBFE** exhibited the on-off and off-on switching behaviors at 360 nm and 510 nm, respectively. No peak shift at 360 nm during on-off switching suggested ICT is not incorporated as the previous cases. Slow nonradiative decay, large size distribution, and SEM image suggested the on-off-on fluorescence switching is triggered by aggregation to form spherical aggregate of **TBFE** in aqueous solution. This study on **TBFE** suggested that the structure-derived properties could be compatible in one molecule by molecular design.

2.5. Experimental section

2.5.1. Synthesis

General consideration

All the reactions dealing with air- or moisture-sensitive compounds were carried out in a dry reaction vessel under a positive pressure of N_2 or Ar gas. Air- and moisture-sensitive liquids and solutions were transferred via syringe or Teflon cannula. Analytical thin-layer chromatography (TLC) was performed using glass plates pre-coated with 0.25 mm, 230–400 mesh silica gel impregnated with a fluorescent indicator (254 nm). Thin-layer chromatography plates were visualized by exposure to ultraviolet light (UV). Organic solutions were concentrated by rotary evaporation at ca. 15 Torr (evacuated with a diaphragm pump). Flash column chromatography was performed as described by Still *et al*.[14], employing Kanto Silica gel 60 (spherical, neutral, 140–325 mesh).

Unless otherwise noted, commercial reagents were purchased from Tokyo Kasei Co., Aldrich Inc., and other commercial suppliers and used as purchased. Anhydrous solvents were purchased from Kanto, and purified by a solvent purification system (GlassContour) equipped with columns of activated alumina and copper catalyst prior to use.

NMR spectra were recorded using a JEOL ECA-500 (^{1}H NMR, 500 MHz; ^{13}C NMR, 125 MHz), JEOL ECZ-500 (^{1}H NMR, 500 MHz; ^{13}C NMR, 125 MHz), and JEOL ECX-400 (^{1}H NMR, 400 MHz; ^{13}C NMR, 100 Hz) NMR spectrometer. Chemical data for protons are reported in parts per million (ppm, δ scale) downfield from tetramethylsilane and are referenced to the residual protons in the NMR solvent ($CDCl_3$: δ 7.26, THF-d_8: δ 1.72, 3.58). Chemical data for carbons are reported in parts per million (ppm, δ scale) downfield from tetramethylsilane and are referenced to the carbon resonance of the solvent ($CDCl_3$: δ 77.0, THF-d_8: δ 25.3, 67.2). The data are presented as follows: chemical shift, multiplicity (s = singlet, d = doublet, t = triplet, m = multiplet and/or multiple resonances, br = broad), coupling constant in Hertz (Hz), and integration. Melting points of solid materials were determined on a Mel-Temp II capillary melting-point apparatus and are uncorrected. Mass spectra were obtained on Bruker micrOTOF II (APCI) mass spectrometer.

Synthetic procedures

3-Bromophenyl *N*,*N*-diethylcarbamate (**2**)

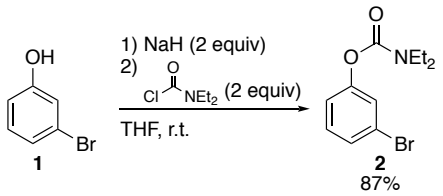

A solution of sodium hydride (2.36 g, 65 wt%, 64 mmol) in THF (20 mL) was dropwise added into a solution of 3-bromophenol (**1**) (5.26 g, 30 mmol) in THF (7.5 mL) at ambient temperature. After stirring for 2.5 h, the resulting brownish mixture was added by *N*,*N*-diethylcarbamoyl chloride (7.61 g, 60 mmol) and stirred for 8 h. The reaction mixture was added to water and organic layer was extracted with ethyl acetate, washed with brine, and dried over anhydrous Na_2SO_4. After removing the solvent *in vacuo*, the crude mixture was purified with column chromatography (eluent: EtOAc/hexane = 1/10) to afford compound **2** (7.09 g, 87%) as a colorless liquid. The ^{1}H NMR spectrum of compound **2** was in agreement with the literature.[8]

3-Bromo-2-iodophenyl *N*,*N*-diethylcarbamate (**3**)

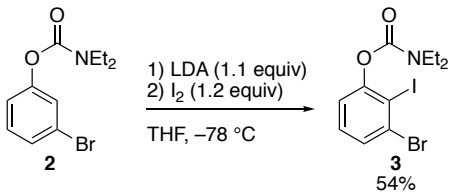

Butyllithium in hexane (13.8 mL, 1.60 mol/L, 22 mmol) was dropwise added into a solution of diisopropylamine (3.08 g, 22 mmol) in THF (60 mL) at 0 °C. After stirring for 30 min at 0 °C, the solution was cooled down to –78 °C, and **2** (5.44 g, 20 mmol) was added to the solution of LDA. The reaction mixture was stirred for 30 min and iodine (6.12 g, 24 mmol) was added at low temperature. After stirring for 30 min at –78 °C, the reaction mixture was allowed to warm to ambient temperature, and aqueous $Na_2S_2O_3$ solution was added to the mixture. Organic layer was extracted with ethyl acetate, washed with brine, dried over anhydrous Na_2SO_4, and evaporated *in vacuo*. The crude mixture was purified with column chromatography (eluent: EtOAc/hexane = 1/10) to afford compound **3** (4.26 g, 54%) as a white solid. The ^{1}H NMR spectrum of compound **3** was in agreement with the literature.[8]

4-Bromo-2-phenylbenzo[*b*]furan (**5**)

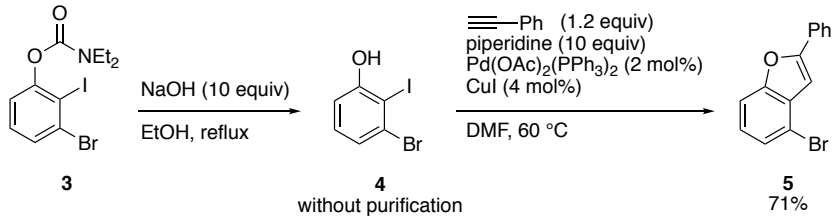

3 → **4** without purification → **5** 71%

Sodium hydroxide (2.00 g, 50 mmol) and **3** (2.00 g, 5.0 mmol) were dissolved into EtOH (40 mL) and refluxed for 4 h. After cooling down to ambient temperature, the solvent was evaporated *in vacuo*. The resulting mixture was dissolved into diethyl ether and neutralized by 1M aqueous HCl solution. Organic layer was extracted with diethyl ether, dried over anhydrous $MgSO_4$ and evaporated *in vacuo*. The crude mixture was used for the next step without further purification.

The crude material was dissolved in DMF (20 mL). Ethynylbenzene (620 mg, 6.0 mmol), piperidine (4.96 g 58 mmol), $Pd(OAc)_2(PPh_3)_2$ (74.4 mg, 2.0 mol%) and CuI (38.0 mg, 4.0 mol%) were added to the solution and stirred for 5 h at 60 °C. The resulting brown-red mixture was allowed to cool down to ambient temperature and then water was added. The organic layer was extracted with ethyl acetate, dried over anhydrous Na_2SO_4, and evaporated *in vacuo*. The crude mixture was purified with column chromatography (eluent: hexane) to afford compound **5** (976 mg, 71% over 2 steps) as a white solid. The ^{1}H NMR spectrum of compound **5** was in agreement with the literature.[8]

Bis(2-phenyl-4-benzo[*b*]furyl)methanol (**6**)

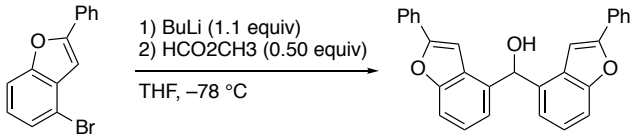

5 → **6** 64%

A solution of butyllithium in hexane (5.16 mL, 1.60 mol/L, 8.3 mmol) was added to a solution of **5** (2.04 g, 7.5 mmol) in THF (40 mL) at –78 °C and stirred for 30 min. After addition of methyl formate (586 mg, 3.8 mmol), the resulting pale-yellow solution was allowed to warm to ambient temperature and stirred for 30 min. After addition of water, organic layer was extracted three times with ethyl acetate, washed with brine, and then dried over anhydrous Na_2SO_4. After removing the solvent *in vacuo*, the crude material was purified by flash silica-gel column chromatography (eluent: EtOAc/hexane = 1/3) to afford compound **6** (991 mg, 64%) as a pale yellow solid. Mp: 84–86 °C; ^{1}H NMR (400 MHz, $CDCl_3$)

δ 2.46 (δ, *J* = 3.4 Hz, 1H, C*H*OH), 6.51 (d, *J* = 3.4 Hz, 1H, CHO*H*), 7.08 (s, 2H, Ar*H*), 7.27–7.37 (m, 6H, Ar*H*), 7.42 (t, *J* = 7.7 Hz, 4H, Ar*H*), 7.49 (dd, *J* = 1.7, 6.3 Hz, 2H, Ar*H*), 7.80–7.84 (m, 4H, Ar*H*); ^{13}C NMR (100 MHz, $CDCl_3$) δ 74.0 (>*C*HOH), 100.5, 111.0, 121.1, 124.3, 125.1, 127.5, 128.7, 128.9, 130.3, 135.4, 155.4, 156.0; HRMS (APCI+) calcd for $C_{29}H_{20}O_3$ (M): 416.1407; found: 416.1408.

Bis(2-phenyl-4-benzo[*b*]furyl)ketone (**7**)

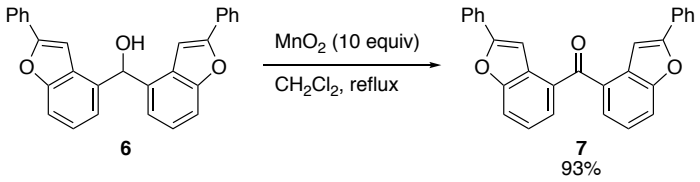

6 **7** 93%

Bis(2-phenyl-4-benzo[*b*]furyl)methanol (**6**) (832 mg, 2.0 mmol) was added to a suspension of manganese(IV) oxide (1.74 g, 20 mmol) in dichloromethane (20 mL). After refluxing for 48 h, water was added to the reaction mixture. The organic layer was extracted with ethyl acetate, and dried over anhydrous Na_2SO_4. After removing the solvent *in vacuo*, the crude mixture was purified with column chromatography (eluent: EtOAc/hexane = 1/3) and reprecipitation (CH_2Cl_2/MeOH) to afford the titled compound (774 mg, 93%) as a pale yellow solid. Mp: 205–206 °C; ^{1}H NMR (400 MHz, $CDCl_3$) δ 7.32–7.43 (m, 4H, Ar*H*), 7.47 (t, *J* = 7.6 Hz, 4H, Ar*H*), 7.53 (s, 2H, Ar*H*), 7.64 (d, *J* = 7.9 Hz, 2H, Ar*H*), 7.76 (d, *J* = 7.9 Hz, 2H, Ar*H*), 7.92 (d, *J* = 8.2 Hz, 4H, Ar*H*); ^{13}C NMR (100 MHz, $CDCl_3$) δ 102.2, 115.2, 123.3, 125.4, 126.9, 129.0, 129.2, 129.9, 130.1, 130.6, 155.5, 158.2, 196.0 (>*C*=O); HRMS (APCI+) calcd for $C_{29}H_{18}O_3$ (M): 414.1250; found: 414.1257.

Tetrakis(2-phenyl-4-benzo[*b*]furyl)ethene (**TBFE**)

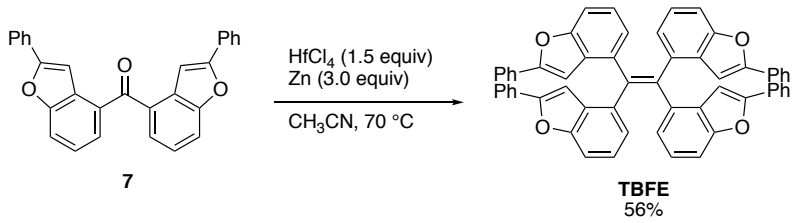

7 **TBFE** 56%

Hafnium(IV) chloride (23 mg, 0.072 mmol) and pre-washed zinc powder (9.4 mg, 0.144 mmol) were suspended in acetonitrile (0.33 mL) and stirred for 5 min at ambient temperature. After addition of **7** (20 mg, 0.048 mmol) into the suspension, the reaction mixture was heated to 70 °C. The resulting brownish red mixture was stirred for 48 h, cooled down to ambient temperature, and added water. Organic layer was extracted with ethyl acetate and dried over anhydrous Na_2SO_4. After removing the solvent *in vacuo*, the crude mixture was purified by column chromatography (eluent: toluene/hexane = 3/10) to afford **TBFE** (10.7 mg, 56%) as a yellow solid. Mp: 103–105 °C; ^{1}H NMR (500 MHz, THF-d_8) δ 6.75 (s, 4H, Ar*H*), 7.03 (t, *J* = 7.5 Hz, 4H, Ar*H*), 7.13 (d, *J* = 7.5 Hz 4H, Ar*H*), 7.20–7.29 (m, 16H, Ar*H*), 7.57 (d, *J* = 6.3 Hz, 4H, Ar*H*); ^{13}C NMR (125 MHz, THF-d_8) δ 102.2, 110.7, 124.7, 125.5, 126.8, 129.2, 129.4, 130.3, 131.1, 137.3, 140.7, 155.9, 156.4; HRMS (APCI+) calcd for $C_{58}H_{37}O_4$ (M+H): 797.2686; found: 797.2672.

2.5.2. Characterization

Computational study

The Density Functional Theory (DFT) calculations for conformers of **TBFE** were conducted at the B3LYP/6-31G (d) level on Gaussian09 packages.[15]

Conformation 1 (**TBFE**-c1):

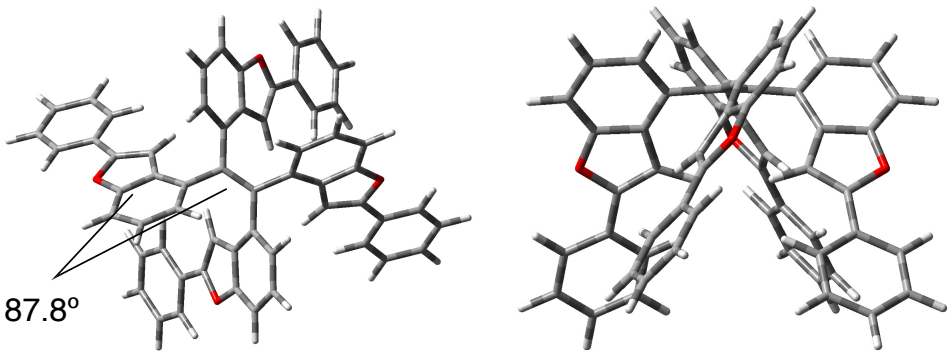

Figure 2.12. Optimized structure of **TBFE**-c1 and a dihedral angle between each BF units and the central ethenyl unit.

Table 2.5. Theoretically optimized coordinates of **TBFE**-c1 calculated at the B3LYP/6-31G(d) level of theory.

Total energy: *E*(RB3LYP/6-31G(d)) = –2532.76502081 Hartree

Center Number	Atomic Number	Atomic Type	Coordinates (Angstroms) X	Y	Z
1	6	0	0	0	-0.684465
2	6	0	0	0	0.684465
3	6	0	-1.253149	0.159253	1.478439
4	6	0	-1.580424	-0.700728	2.554399
5	6	0	-2.141525	1.214102	1.222935
6	6	0	-2.763283	-0.470873	3.284856
7	6	0	-3.306866	1.418002	1.978317
8	6	0	-3.645639	0.569783	3.032974
9	1	0	-3.955727	2.254591	1.735456
10	1	0	-4.54252	0.709092	3.627159

11	6	0	-1.253149	-0.159253	-1.478439
12	6	0	-2.141525	-1.214102	-1.222935
13	6	0	-3.306866	-1.418002	-1.978317
14	6	0	-3.645639	-0.569783	-3.032974
15	1	0	-3.955727	-2.254591	-1.735456
16	1	0	-4.54252	-0.709092	-3.627159
17	6	0	1.253149	0.159253	-1.478439
18	6	0	2.141525	1.214102	-1.222935
19	6	0	3.306866	1.418002	-1.978317
20	6	0	3.645639	0.569783	-3.032974
21	1	0	3.955727	2.254591	-1.735456
22	1	0	4.54252	0.709092	-3.627159
23	6	0	1.253149	-0.159253	1.478439
24	6	0	1.580424	0.700728	2.554399
25	6	0	2.141525	-1.214102	1.222935
26	6	0	2.763283	0.470873	3.284856
27	6	0	3.306866	-1.418002	1.978317
28	6	0	3.645639	-0.569783	3.032974
29	1	0	3.955727	-2.254591	1.735456
30	1	0	4.54252	-0.709092	3.627159
31	6	0	2.763283	-0.470873	-3.284856
32	6	0	1.580424	-0.700728	-2.554399
33	6	0	0.994865	-1.873153	-3.14548
34	1	0	0.06848	-2.347038	-2.857842
35	6	0	1.821735	-2.264891	-4.161446
36	8	0	2.909919	-1.417328	-4.25958
37	6	0	-2.763283	0.470873	-3.284856
38	6	0	-1.580424	0.700728	-2.554399
39	6	0	-0.994865	1.873153	-3.14548
40	1	0	-0.06848	2.347038	-2.857842

41	6	0	-1.821735	2.264891	-4.161446
42	8	0	-2.909919	1.417328	-4.25958
43	6	0	1.765361	-3.363713	-5.117962
44	6	0	2.765437	-3.522189	-6.093444
45	6	0	0.704454	-4.287296	-5.081559
46	6	0	2.702657	-4.574443	-7.004456
47	1	0	3.587202	-2.815512	-6.130797
48	6	0	0.647551	-5.335936	-5.993895
49	1	0	-0.078008	-4.181404	-4.335885
50	6	0	1.646105	-5.485647	-6.960413
51	1	0	3.483704	-4.68183	-7.75246
52	1	0	-0.179571	-6.039481	-5.951182
53	1	0	1.599532	-6.305275	-7.672135
54	6	0	-1.765361	3.363713	-5.117962
55	6	0	-2.765437	3.522189	-6.093444
56	6	0	-0.704454	4.287296	-5.081559
57	6	0	-2.702657	4.574443	-7.004456
58	1	0	-3.587202	2.815512	-6.130797
59	6	0	-0.647551	5.335936	-5.993895
60	1	0	0.078008	4.181404	-4.335885
61	6	0	-1.646105	5.485647	-6.960413
62	1	0	-3.483704	4.68183	-7.75246
63	1	0	0.179571	6.039481	-5.951182
64	1	0	-1.599532	6.305275	-7.672135
65	6	0	0.994865	1.873153	3.14548
66	1	0	0.06848	2.347038	2.857842
67	6	0	1.821735	2.264891	4.161446
68	6	0	-0.994865	-1.873153	3.14548
69	1	0	-0.06848	-2.347038	2.857842
70	6	0	-1.821735	-2.264891	4.161446

71	8	0	-2.909919	-1.417328	4.25958
72	8	0	2.909919	1.417328	4.25958
73	6	0	-1.765361	-3.363713	5.117962
74	6	0	-2.765437	-3.522189	6.093444
75	6	0	-0.704454	-4.287296	5.081559
76	6	0	-2.702657	-4.574443	7.004456
77	1	0	-3.587202	-2.815512	6.130797
78	6	0	-0.647551	-5.335936	5.993895
79	1	0	0.078008	-4.181404	4.335885
80	6	0	-1.646105	-5.485647	6.960413
81	1	0	-3.483704	-4.68183	7.75246
82	1	0	0.179571	-6.039481	5.951182
83	1	0	-1.599532	-6.305275	7.672135
84	6	0	1.765361	3.363713	5.117962
85	6	0	2.765437	3.522189	6.093444
86	6	0	0.704454	4.287296	5.081559
87	6	0	2.702657	4.574443	7.004456
88	1	0	3.587202	2.815512	6.130797
89	6	0	0.647551	5.335936	5.993895
90	1	0	-0.078008	4.181404	4.335885
91	6	0	1.646105	5.485647	6.960413
92	1	0	3.483704	4.68183	7.75246
93	1	0	-0.179571	6.039481	5.951182
94	1	0	1.599532	6.305275	7.672135
95	1	0	-1.914041	-1.89806	-0.411264
96	1	0	-1.914041	1.89806	0.411264
97	1	0	1.914041	1.89806	-0.411264
98	1	0	1.914041	-1.89806	0.411264

Conformation 2 (**TBFE**-c2):

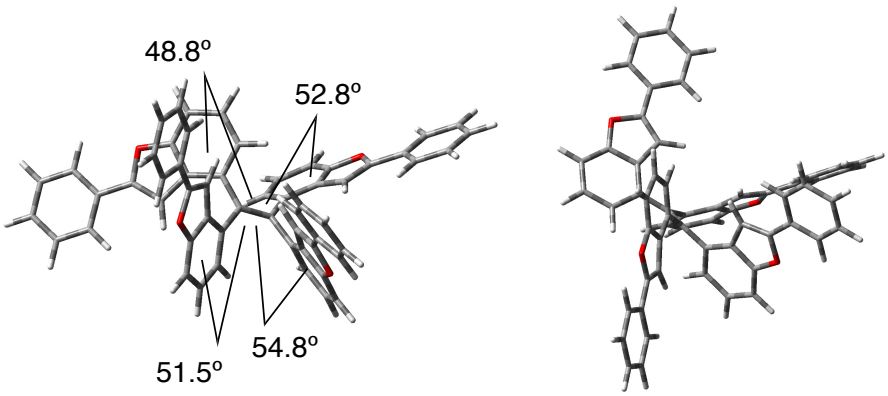

Figure 2.13. Optimized structure of **TBFE**-c2 and dihedral angles between each BF units and the central ethenyl unit.

Table 2.6. Theoretically optimized coordinates of **TBFE**-c2 calculated at the B3LYP/6-31G(d) level of theory.

Total energy: *E*(RB3LYP/6-31G(d)) = –2532.76497285 Hartree

Center Number	Atomic Number	Atomic Type	Coordinates (Angstroms) X	Y	Z
1	6	0	-0.472662	-0.954036	0.568073
2	6	0	0.734704	-1.451061	0.97805
3	6	0	1.280968	-2.735017	0.44651
4	6	0	2.585721	-2.828306	-0.093517
5	6	0	0.538919	-3.921412	0.512578
6	6	0	3.054881	-4.074481	-0.55091
7	6	0	1.043847	-5.150433	0.057534
8	6	0	2.321706	-5.251659	-0.491754
9	1	0	0.424555	-6.039158	0.137739
10	1	0	2.727566	-6.191201	-0.851596
11	6	0	-1.175424	-1.489495	-0.635443
12	6	0	-0.518073	-1.605378	-1.86874
13	6	0	-1.162286	-2.070974	-3.025865
14	6	0	-2.505038	-2.449123	-3.006526
15	1	0	-0.601328	-2.136906	-3.953686

16	1	0	-3.020067	-2.814029	-3.888834
17	6	0	-1.174582	0.142747	1.294303
18	6	0	-1.352714	0.096965	2.684403
19	6	0	-2.037045	1.098818	3.390839
20	6	0	-2.578752	2.206181	2.73842
21	1	0	-2.145523	1.006827	4.467691
22	1	0	-3.106026	2.993332	3.266743
23	6	0	1.58654	-0.792651	2.01295
24	6	0	1.970542	0.568098	1.939376
25	6	0	2.107726	-1.536316	3.081493
26	6	0	2.816271	1.1003	2.933087
27	6	0	2.936992	-0.96894	4.061352
28	6	0	3.311463	0.373808	4.006293
29	1	0	3.298523	-1.59136	4.874822
30	1	0	3.95969	0.828232	4.748044
31	6	0	-2.405402	2.246185	1.36258
32	6	0	-1.736694	1.254179	0.619079
33	6	0	-1.788093	1.708526	-0.74476
34	1	0	-1.393421	1.198918	-1.610832
35	6	0	-2.462906	2.898761	-0.745199
36	8	0	-2.84648	3.242176	0.53662
37	6	0	-3.153137	-2.330254	-1.785635
38	6	0	-2.542272	-1.857594	-0.607159
39	6	0	-3.569562	-1.912066	0.397128
40	1	0	-3.476443	-1.618183	1.431598
41	6	0	-4.697466	-2.39101	-0.209202
42	8	0	-4.459025	-2.653248	-1.545879
43	6	0	-2.835793	3.826575	-1.806642
44	6	0	-3.507963	5.025626	-1.510861
45	6	0	-2.528514	3.536729	-3.148875

46	6	0	-3.859894	5.907312	-2.530568
47	1	0	-3.75061	5.257944	-0.479721
48	6	0	-2.881955	4.421807	-4.162414
49	1	0	-2.016003	2.612108	-3.397837
50	6	0	-3.549391	5.611894	-3.859106
51	1	0	-4.379648	6.829535	-2.284857
52	1	0	-2.638178	4.181	-5.193655
53	1	0	-3.825767	6.30095	-4.6524
54	6	0	-6.04516	-2.665406	0.27478
55	6	0	-7.023048	-3.197056	-0.584311
56	6	0	-6.391679	-2.403038	1.613025
57	6	0	-8.308377	-3.458837	-0.115122
58	1	0	-6.766558	-3.401874	-1.617925
59	6	0	-7.676868	-2.667197	2.075612
60	1	0	-5.651526	-1.98779	2.290744
61	6	0	-8.642341	-3.196643	1.214656
62	1	0	-9.052048	-3.86986	-0.792682
63	1	0	-7.927081	-2.45775	3.11218
64	1	0	-9.645496	-3.4015	1.578296
65	6	0	1.740755	1.650108	1.022472
66	1	0	1.141095	1.623332	0.125912
67	6	0	2.418671	2.735126	1.504041
68	6	0	3.653316	-1.902511	-0.355847
69	1	0	3.661794	-0.845521	-0.134703
70	6	0	4.669051	-2.616018	-0.929535
71	8	0	4.318457	-3.947815	-1.056982
72	8	0	3.085035	2.415316	2.672688
73	6	0	5.994919	-2.244504	-1.40905
74	6	0	6.848484	-3.204578	-1.980573
75	6	0	6.444968	-0.915169	-1.307229

76	6	0	8.114145	-2.842101	-2.436245
77	1	0	6.511565	-4.232095	-2.063047
78	6	0	7.709786	-0.559515	-1.764619
79	1	0	5.801615	-0.159569	-0.866044
80	6	0	8.551517	-1.520593	-2.331639
81	1	0	8.761366	-3.596821	-2.875148
82	1	0	8.040638	0.471885	-1.677266
83	1	0	9.539121	-1.240578	-2.687687
84	6	0	2.559015	4.105336	1.026288
85	6	0	3.458428	4.994216	1.640802
86	6	0	1.79256	4.561435	-0.062096
87	6	0	3.590356	6.299816	1.172806
88	1	0	4.050127	4.652769	2.483249
89	6	0	1.930933	5.865834	-0.52598
90	1	0	1.075218	3.896493	-0.534188
91	6	0	2.831064	6.741504	0.087746
92	1	0	4.290449	6.974511	1.658417
93	1	0	1.32822	6.202328	-1.365157
94	1	0	2.935539	7.760433	-0.274871
95	1	0	0.528303	-1.322467	-1.927726
96	1	0	-0.461615	-3.885478	0.932316
97	1	0	-0.946297	-0.747223	3.231716
98	1	0	1.853413	-2.589739	3.153686

Conformation 3 (**TBFE**-c3):

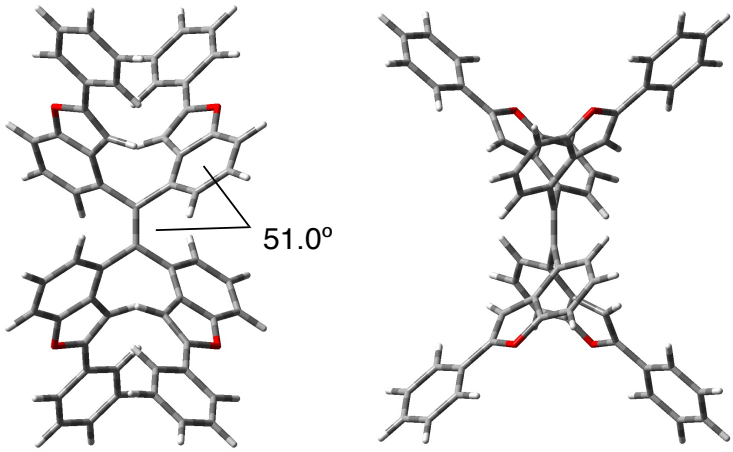

Figure 2.14. Optimized structure of **TBFE**-c3 and a dihedral angle between each BF units and the central ethenyl unit.

Table 2.7. Theoretically optimized coordinates of **TBFE**-c3 calculated at the B3LYP/6-31G(d) level of theory.

Total energy: *E*(RB3LYP/6-31G(d)) = –2532.76478938 Hartree

Center Number	Atomic Number	Atomic Type	Coordinates (Angstroms) X	Y	Z
1	6	0	0	0	-0.684465
2	6	0	0	0	0.684465
3	6	0	-1.253149	0.159253	1.478439
4	6	0	-1.580424	-0.700728	2.554399
5	6	0	-2.141525	1.214102	1.222935
6	6	0	-2.763283	-0.470873	3.284856
7	6	0	-3.306866	1.418002	1.978317
8	6	0	-3.645639	0.569783	3.032974
9	1	0	-3.955727	2.254591	1.735456
10	1	0	-4.54252	0.709092	3.627159
11	6	0	-1.253149	-0.159253	-1.478439
12	6	0	-2.141525	-1.214102	-1.222935
13	6	0	-3.306866	-1.418002	-1.978317
14	6	0	-3.645639	-0.569783	-3.032974

15	1	0	-3.955727	-2.254591	-1.735456
16	1	0	-4.54252	-0.709092	-3.627159
17	6	0	1.253149	0.159253	-1.478439
18	6	0	2.141525	1.214102	-1.222935
19	6	0	3.306866	1.418002	-1.978317
20	6	0	3.645639	0.569783	-3.032974
21	1	0	3.955727	2.254591	-1.735456
22	1	0	4.54252	0.709092	-3.627159
23	6	0	1.253149	-0.159253	1.478439
24	6	0	1.580424	0.700728	2.554399
25	6	0	2.141525	-1.214102	1.222935
26	6	0	2.763283	0.470873	3.284856
27	6	0	3.306866	-1.418002	1.978317
28	6	0	3.645639	-0.569783	3.032974
29	1	0	3.955727	-2.254591	1.735456
30	1	0	4.54252	-0.709092	3.627159
31	6	0	2.763283	-0.470873	-3.284856
32	6	0	1.580424	-0.700728	-2.554399
33	6	0	0.994865	-1.873153	-3.14548
34	1	0	0.06848	-2.347038	-2.857842
35	6	0	1.821735	-2.264891	-4.161446
36	8	0	2.909919	-1.417328	-4.25958
37	6	0	-2.763283	0.470873	-3.284856
38	6	0	-1.580424	0.700728	-2.554399
39	6	0	-0.994865	1.873153	-3.14548
40	1	0	-0.06848	2.347038	-2.857842
41	6	0	-1.821735	2.264891	-4.161446
42	8	0	-2.909919	1.417328	-4.25958
43	6	0	1.765361	-3.363713	-5.117962
44	6	0	2.765437	-3.522189	-6.093444

45	6	0	0.704454	-4.287296	-5.081559
46	6	0	2.702657	-4.574443	-7.004456
47	1	0	3.587202	-2.815512	-6.130797
48	6	0	0.647551	-5.335936	-5.993895
49	1	0	-0.078008	-4.181404	-4.335885
50	6	0	1.646105	-5.485647	-6.960413
51	1	0	3.483704	-4.68183	-7.75246
52	1	0	-0.179571	-6.039481	-5.951182
53	1	0	1.599532	-6.305275	-7.672135
54	6	0	-1.765361	3.363713	-5.117962
55	6	0	-2.765437	3.522189	-6.093444
56	6	0	-0.704454	4.287296	-5.081559
57	6	0	-2.702657	4.574443	-7.004456
58	1	0	-3.587202	2.815512	-6.130797
59	6	0	-0.647551	5.335936	-5.993895
60	1	0	0.078008	4.181404	-4.335885
61	6	0	-1.646105	5.485647	-6.960413
62	1	0	-3.483704	4.68183	-7.75246
63	1	0	0.179571	6.039481	-5.951182
64	1	0	-1.599532	6.305275	-7.672135
65	6	0	0.994865	1.873153	3.14548
66	1	0	0.06848	2.347038	2.857842
67	6	0	1.821735	2.264891	4.161446
68	6	0	-0.994865	-1.873153	3.14548
69	1	0	-0.06848	-2.347038	2.857842
70	6	0	-1.821735	-2.264891	4.161446
71	8	0	-2.909919	-1.417328	4.25958
72	8	0	2.909919	1.417328	4.25958
73	6	0	-1.765361	-3.363713	5.117962
74	6	0	-2.765437	-3.522189	6.093444

75	6	0	-0.704454	-4.287296	5.081559
76	6	0	-2.702657	-4.574443	7.004456
77	1	0	-3.587202	-2.815512	6.130797
78	6	0	-0.647551	-5.335936	5.993895
79	1	0	0.078008	-4.181404	4.335885
80	6	0	-1.646105	-5.485647	6.960413
81	1	0	-3.483704	-4.68183	7.75246
82	1	0	0.179571	-6.039481	5.951182
83	1	0	-1.599532	-6.305275	7.672135
84	6	0	1.765361	3.363713	5.117962
85	6	0	2.765437	3.522189	6.093444
86	6	0	0.704454	4.287296	5.081559
87	6	0	2.702657	4.574443	7.004456
88	1	0	3.587202	2.815512	6.130797
89	6	0	0.647551	5.335936	5.993895
90	1	0	-0.078008	4.181404	4.335885
91	6	0	1.646105	5.485647	6.960413
92	1	0	3.483704	4.68183	7.75246
93	1	0	-0.179571	6.039481	5.951182
94	1	0	1.599532	6.305275	7.672135
95	1	0	-1.914041	-1.89806	-0.411264
96	1	0	-1.914041	1.89806	0.411264
97	1	0	1.914041	1.89806	-0.411264
98	1	0	1.914041	-1.89806	0.411264

Conformation 4 (**TBFE**-c4):

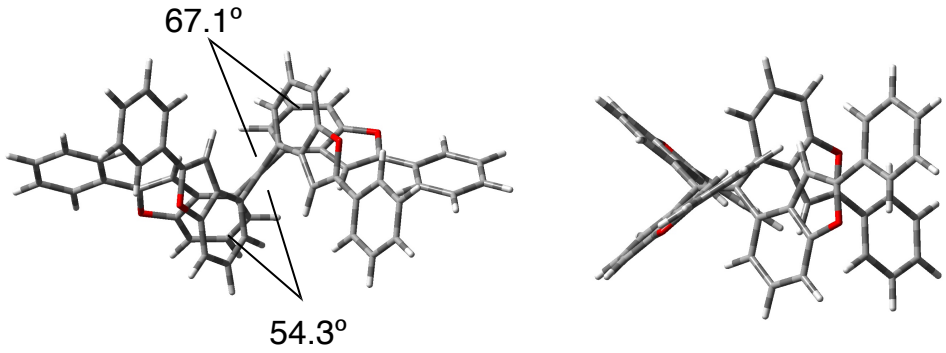

Figure 2.15. Optimized structure of **TBFE**-c4 and dihedral angles between each BF units and the central ethenyl unit.

Table 2.8. Theoretically optimized coordinates of **TBFE**-c4 calculated at the B3LYP/6-31G(d) level of theory.

Total energy: *E*(RB3LYP/6-31G(d)) = –2532.76440056 Hartree

Center Number	Atomic Number	Atomic Type	Coordinates (Angstroms) X	Y	Z
1	6	0	-0.000067	-2.165376	0.00005
2	6	0	-0.000043	-0.796416	0.000024
3	6	0	-0.717644	-0.003	1.039935
4	6	0	-1.560476	1.085209	0.70547
5	6	0	-0.553146	-0.272624	2.406115
6	6	0	-2.198507	1.805191	1.734368
7	6	0	-1.194501	0.476525	3.405463
8	6	0	-2.041421	1.537927	3.086601
9	1	0	-1.026568	0.221289	4.44782
10	1	0	-2.551095	2.12426	3.843692
11	6	0	-0.909744	-2.98	0.861411
12	6	0	-0.39626	-4.011452	1.661231
13	6	0	-1.214679	-4.8236	2.460708
14	6	0	-2.600926	-4.663566	2.476637
15	1	0	-0.758745	-5.596036	3.073367
16	1	0	-3.252015	-5.288337	3.078883

17	6	0	0.909591	-2.980067	-0.861284
18	6	0	0.396086	-4.011558	-1.661031
19	6	0	1.214482	-4.82379	-2.460449
20	6	0	2.600731	-4.663794	-2.476387
21	1	0	0.758521	-5.59626	-3.073045
22	1	0	3.251812	-5.288632	-3.078572
23	6	0	0.717614	-0.003063	-1.039898
24	6	0	1.560533	1.085082	-0.705438
25	6	0	0.553105	-0.272696	-2.406077
26	6	0	2.198641	1.804981	-1.734347
27	6	0	1.194535	0.476376	-3.40543
28	6	0	2.041548	1.537709	-3.086575
29	1	0	1.026592	0.221139	-4.447784
30	1	0	2.55129	2.123984	-3.843665
31	6	0	3.107548	-3.661443	-1.662623
32	6	0	2.314884	-2.815214	-0.860989
33	6	0	3.247382	-1.962456	-0.178187
34	1	0	3.014719	-1.185784	0.533733
35	6	0	4.498181	-2.317377	-0.599049
36	8	0	4.431492	-3.358938	-1.506704
37	6	0	-3.107724	-3.661275	1.662789
38	6	0	-2.315031	-2.815124	0.861096
39	6	0	-3.247508	-1.962419	0.178201
40	1	0	-3.014846	-1.185897	-0.533884
41	6	0	-4.498313	-2.317259	0.5991
42	8	0	-4.431661	-3.358753	1.50684
43	6	0	5.829489	-1.82014	-0.273574
44	6	0	6.979032	-2.503401	-0.707589
45	6	0	5.985348	-0.644437	0.483571
46	6	0	8.247409	-2.026409	-0.384239

47	1	0	6.868376	-3.408297	-1.295269
48	6	0	7.255033	-0.174847	0.805245
49	1	0	5.109099	-0.088894	0.804893
50	6	0	8.392517	-0.863595	0.374532
51	1	0	9.126074	-2.566963	-0.726192
52	1	0	7.356934	0.737005	1.387415
53	1	0	9.382915	-0.493413	0.625034
54	6	0	-5.829596	-1.82004	0.273496
55	6	0	-6.979174	-2.503824	0.70659
56	6	0	-5.985368	-0.643838	-0.48289
57	6	0	-8.247513	-2.02686	0.383048
58	1	0	-6.86857	-3.409099	1.293699
59	6	0	-7.255017	-0.174289	-0.804779
60	1	0	-5.109083	-0.087887	-0.803406
61	6	0	-8.392536	-0.863564	-0.375003
62	1	0	-9.126214	-2.567818	0.724271
63	1	0	-7.356865	0.737949	-1.386352
64	1	0	-9.382905	-0.49341	-0.625659
65	6	0	2.015944	1.692554	0.516309
66	1	0	1.729372	1.41791	1.520342
67	6	0	2.865339	2.706557	0.166969
68	6	0	-2.015886	1.692668	-0.516286
69	1	0	-1.729405	1.417936	-1.520323
70	6	0	-2.865187	2.706751	-0.166962
71	8	0	-2.988288	2.788263	1.20664
72	8	0	2.988494	2.788008	-1.206623
73	6	0	-3.631417	3.671988	-0.946717
74	6	0	-4.515027	4.565567	-0.316114
75	6	0	-3.501496	3.724087	-2.346844
76	6	0	-5.248195	5.481384	-1.067558

77	1	0	-4.621538	4.533886	0.762642
78	6	0	-4.237523	4.640232	-3.09164
79	1	0	-2.815891	3.049189	-2.850942
80	6	0	-5.114976	5.523626	-2.456505
81	1	0	-5.92707	6.164777	-0.564463
82	1	0	-4.123409	4.667784	-4.171964
83	1	0	-5.687338	6.239332	-3.040165
84	6	0	3.631602	3.671766	0.946726
85	6	0	4.51498	4.565554	0.31609
86	6	0	3.501939	3.723641	2.346883
87	6	0	5.248165	5.481358	1.067531
88	1	0	4.621298	4.534042	-0.76269
89	6	0	4.237973	4.639784	3.091677
90	1	0	2.816548	3.048554	2.851019
91	6	0	5.115189	5.523388	2.456509
92	1	0	5.92686	6.164911	0.56441
93	1	0	4.12406	4.667158	4.172026
94	1	0	5.687562	6.239087	3.040167
95	1	0	0.676511	-4.181667	1.664221
96	1	0	0.094432	-1.092616	2.69888
97	1	0	-0.676691	-4.181742	-1.664027
98	1	0	-0.094539	-1.092641	-2.698822

Conformation 5 (**TBFE**-c5):

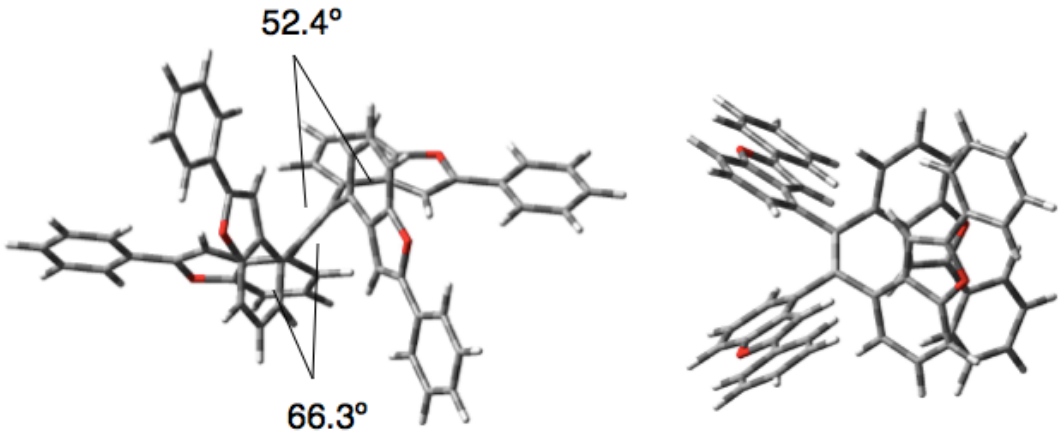

Figure 2.16. Optimized structure of **TBFE**-c5 and dihedral angles between each BF units and the central ethenyl unit.

Table 2.9. Theoretically optimized coordinates of **TBFE**-c5 calculated at the B3LYP/6-31G(d) level of theory.

Total energy: *E*(RB3LYP/6-31G(d)) = –2532.76338993 Hartree

Center Number	Atomic Number	Atomic Type	Coordinates (Angstroms) X	Y	Z
1	6	0	0.460103	-0.678823	-0.505498
2	6	0	-0.460195	-0.678822	0.505858
3	6	0	-1.10091	0.557382	1.043793
4	6	0	-1.746145	1.514012	0.223514
5	6	0	-1.15447	0.779702	2.427851
6	6	0	-2.366013	2.628965	0.824112
7	6	0	-1.768086	1.909303	2.989818
8	6	0	-2.39152	2.867178	2.190173
9	1	0	-1.763944	2.034332	4.068735
10	1	0	-2.883052	3.741094	2.604184
11	6	0	1.100794	0.557407	-1.043418
12	6	0	1.154259	0.779759	-2.427476
13	6	0	1.767883	1.909345	-2.989471

14	6	0	2.391418	2.867178	-2.18986
15	1	0	1.763678	2.034384	-4.068387
16	1	0	2.882958	3.741078	-2.603897
17	6	0	0.877707	-1.942154	-1.184845
18	6	0	-0.062546	-2.801647	-1.767327
19	6	0	0.309129	-3.974697	-2.444705
20	6	0	1.647034	-4.347868	-2.570191
21	1	0	-0.46371	-4.601517	-2.880137
22	1	0	1.95301	-5.25152	-3.08664
23	6	0	-0.877877	-1.942184	1.185094
24	6	0	-2.239708	-2.30336	1.317677
25	6	0	0.062277	-2.801762	1.767613
26	6	0	-2.575537	-3.491804	1.993714
27	6	0	-0.309525	-3.974846	2.444851
28	6	0	-1.647464	-4.347979	2.570155
29	1	0	0.463233	-4.601745	2.880313
30	1	0	-1.95352	-5.251673	3.086485
31	6	0	2.575209	-3.491769	-1.993791
32	6	0	2.239512	-2.30336	-1.317627
33	6	0	3.491629	-1.750787	-0.879089
34	1	0	3.635784	-0.834584	-0.325922
35	6	0	4.474395	-2.601757	-1.30316
36	8	0	3.930187	-3.673126	-1.987777
37	6	0	2.366026	2.628927	-0.8238
38	6	0	1.746165	1.513984	-0.223179
39	6	0	2.016779	1.647426	1.181966
40	1	0	1.702334	0.976975	1.966129
41	6	0	2.738569	2.796962	1.345328
42	8	0	2.959482	3.411443	0.126895
43	6	0	5.92608	-2.586341	-1.16818

44	6	0	6.709362	-3.62807	-1.695678
45	6	0	6.570134	-1.525998	-0.504268
46	6	0	8.095812	-3.607095	-1.560256
47	1	0	6.222865	-4.449921	-2.209508
48	6	0	7.954937	-1.511192	-0.371908
49	1	0	5.982937	-0.710399	-0.092602
50	6	0	8.725624	-2.551427	-0.898835
51	1	0	8.686246	-4.420365	-1.973896
52	1	0	8.435091	-0.683886	0.143753
53	1	0	9.80705	-2.537522	-0.794565
54	6	0	3.29761	3.458898	2.517871
55	6	0	4.077342	4.621265	2.384365
56	6	0	3.06894	2.94277	3.806656
57	6	0	4.614149	5.244254	3.508948
58	1	0	4.257589	5.028613	1.395574
59	6	0	3.609221	3.568489	4.925597
60	1	0	2.460039	2.052076	3.930444
61	6	0	4.385216	4.722279	4.783206
62	1	0	5.214611	6.14196	3.388008
63	1	0	3.42199	3.156045	5.913413
64	1	0	4.805213	5.209967	5.658569
65	6	0	-3.491742	-1.750692	0.879024
66	1	0	-3.63579	-0.834307	0.326129
67	6	0	-4.474588	-2.60172	1.302791
68	6	0	-2.016616	1.647505	-1.181652
69	1	0	-1.702457	0.976877	-1.965782
70	6	0	-2.738252	2.797132	-1.345054
71	8	0	-2.959308	3.411559	-0.126628
72	8	0	-3.930524	-3.673137	1.987442
73	6	0	-3.297128	3.459111	-2.517651

74	6	0	-4.080069	4.619293	-2.383909
75	6	0	-3.065075	2.945209	-3.806717
76	6	0	-4.616798	5.242253	-3.508542
77	1	0	-4.262867	5.024966	-1.394896
78	6	0	-3.605375	3.570832	-4.925706
79	1	0	-2.453328	2.05649	-3.930671
80	6	0	-4.384623	4.722398	-4.783081
81	1	0	-5.219774	6.138249	-3.387423
82	1	0	-3.415496	3.160143	-5.913748
83	1	0	-4.804577	5.210053	-5.658485
84	6	0	-5.926255	-2.586207	1.167624
85	6	0	-6.709902	-3.626443	1.697518
86	6	0	-6.56993	-1.527244	0.501143
87	6	0	-8.096342	-3.605322	1.562001
88	1	0	-6.223696	-4.447248	2.213292
89	6	0	-7.954728	-1.512254	0.368756
90	1	0	-5.982432	-0.712944	0.08734
91	6	0	-8.725783	-2.550977	0.898118
92	1	0	-8.68706	-4.417424	1.977524
93	1	0	-8.434581	-0.686033	-0.148922
94	1	0	-9.807201	-2.536952	0.793785
95	1	0	0.700766	0.045647	-3.087576
96	1	0	-0.701047	0.045563	3.087965
97	1	0	-1.115593	-2.548973	-1.690312
98	1	0	1.115343	-2.549125	1.690711

Photophysical properties

UV-Vis absorption spectra were measured with a JASCO V-670 spectrometer. Fluorescence spectra were measured with a HITACHI F-4500 spectrometer. Photoluminescence quantum yields were measured on Hamamatsu Photonics C9920–02 Absolute PL Quantum Yield Measurement System, and absolute quantum yields were determined by using a calibrated integrating sphere system. Fluorescence lifetimes were measured on Hamamatsu Photonics C11367-02 Quantaurus-Tau. The absorption maximum wavelengths were used as excitation wavelengths. Spectral grade solvent (THF) and milli-Q water were used as solvents for UV-Vis absorption fluorescence measurements.

Dynamic Light scattering

Dynamic laser light scattering (DLS) study on size distribution was carried out on a Malvern Zetasizer Nano ZS machine.

TBFE (31 mg, 38.9 μmol) was dissolved in THF (10 mL). 1 mL of the solution was added in 10 mL measuring flasks and diluted with water and THF to make the sample solutions (0.39 mM, THF/H_2O = 100/0–10/90). After sonication for 10 min, each solution was put in glass cells and the measurement took place at 25 °C. Viscosity and refractive index of the mixed solvents at ambient temperature (Table 2.10) were estimated from their mole fraction of THF by linear interpolations of the values previously reported by Walter *et al*.[16] The estimated values were used for transformation of the resulting correlation function into volume distribution. The correlation functions obtained in the measurements were output as volume distribution through the treatment of a Malvern Zetasizer Nano ZS software.

Table 2.10. Estimated viscosity and refractive index of THF/H_2O at 25 °C.

THF/H_2O (v/v)	Mole fraction of THF	Viscosity (cps)	Refractive index ($n^{25}D$)
10/90	0.283	1.47	1.384
20/80	0.470	1.02	1.395
30/70	0.604	0.796	1.399
40/60	0.703	0.676	1.401
50/50	0.780	0.604	1.402
60/40	0.842	0.558	1.403
70/30	0.892	0.529	1.403
80/20	0.934	0.506	1.404
90/10	0.970	0.486	1.404
100/0	1.000	0.470	1.405

Scanning Electron Microscopy

SEM observation was performed on an FEI Magellan 400L instrument scanning electron microscope equipped with AMETEK/EDAZ Genesis APEX4 instrument at a landing voltage of 1 kV under a reduced pressure of 5×10^{-5} Pa.

X-ray diffraction

XRD experiment was performed on a Rigaku SmartLab X-ray diffractometer equipped with a scintillation counter. The measurement employed Cu Kα (λ = 1.5419 Å) radiation at 9 kW (45 kV, 200mA) power.

2.6. References

[1] Luo, J.; Xie, Z.; Lam, J. W. Y.; Chen, L.; Chen, H.; Qui, C.; Kwok, H. S.; Zhan, X.; Liu, Y.; Zhu, D.; Tang, B. Z. *Chem. Commun*. **2001**, 1740–1741.

[2] Mei, J.; Hong, Y.; Lam, J. W. Y.; Qin, A.; Tang, Y.; Tang, B. Z. *Adv. Mater.* **2014**, *26*, 5429–5479.

[3] Tong, H.; Dong, Y.; Hong, Y.; Häussler, M.; Lam, J. W. Y.; Sung, H. H.-Y.; Yu, X.; Sun, J.; Williams,I. D.; Kwok , H. S.; Tang, B. Z. *J. Phys. Chem. C* **2007**, *111*, 2287–2294.

[4] Mei, J.; Leung, N. L. C.; Kwok, R. T. K.; Lam, J. W. Y.; Tang, B. Z. *Chem. Rev.* **2015**, *115*, 11718–11940.

[5] (a) Ananhakrishnan, S. J.; Varathan, E.; Ravindran, E.; Somanathan, N.; Subramanian, V.: Mandal, A. B.; Sudha, D. J.; Ramakrishnan, R. *Chem. Commun*. **2013**, *49*, 10742–10744. (b) Li, Y.; Wu, Y.; Chang, J.; Chen, J.; Liu, L.; Li, F. *Chem. Commun.* **2013**, *49*, 11335–11337. Wang, E.; Lam, J. W. Y.; Hu, R.; Zhang, C.; Zhao, Y. S.; Tang, B. Z. *J. Mater. Chem. C* **2014**, *2*, 1801–1807. (d) Hu, R.; Lager, E.; Afuilar-Aguilar, A.; Liu, J.; Lam, J. W. Y.; Sung, H. H. Y.; Williams, I. D.; Zhong, Y.; Wong, K. S.; Peña-Cabrera, E.; Tang, B. Z. *J. Phys. Chem. C* **2009**, *113*, 15845–15853.

[6] Tsuji, H.; Nakamura, E. *Acc. Chem. Res.* **2017**, *50*, 396–406.

[7] Hiroyoshi, H. Master Thesis **2017**.

[8] Sanz, R.; Castroviejo, M. P.; Fernández, Y.; Fañanás, F. J. *J. Org. Chem.* **2005**, *70*, 6548–6551.

[9] Mukaiyama,T.; Sato, T.; Hanna, J. *Chem. Lett.,* **1973**, 1041–1044.

[10] (a) McMurry, J. E. Chem. Rev., 1989, 89, 1513–1524. (b) Ephritikhine, M. *Chem. Commun.* **1998**, 2549–2554.

[11] *CRC Handbook of Chemistry and Physics, 97th Edition;* Haynes, W. M., Ed.; Boca Raton, CRC Press, 2016.

[12] Ren, Y.; Lam, J. W. Y.; Dong, Y.; Tang, B. Z.; Wong, K. S. *J. Phys. Chem. B* **2005**, *109*, 1135–1140.

[13] Chalikian, T. V. *J. Phys. Chem. B* **2001**, *105*, 12566–12578.

[14] Still, W. C.; Kahn, M.; Mitra, A. *J. Org. Chem. 1978,* **43**, 2923–2925.

[15] Gaussian 09, Revision B.01, Frisch, M. J.; Trucks, G. W.; Schlegel, H. B.; G. E. Scuseria, ; Robb, M. A.; Cheeseman, J. R.; Scalmani, G.; Barone, V.; Mennucci, B.; Petersson, G. A.; Nakatsuji, H.; Caricato, M.; Li, X.; Hratchian, H. P.; Izmaylov, A. F.; Bloino, J.; Zheng, G.; Sonnenberg, J. L.; Hada, M.; Ehara, M.; Toyota, K.; Fukuda, R.; Hasegawa, J.; Ishida, M.; Nakajima, T.; Honda, Y.; Kitao, O.; Nakai, H.; Vreven, T.; Montgomery Jr. J. A.; , Peralta, J. E.; Ogliaro, F.; Bearpark, M.; Heyd, J. J.; Brothers, E.;

Kudin, K. N.; Staroverov, V. N.; Keith, T.; Kobayashi, R.; Normand, J.; Raghavachari, K.; Rendell, A.; Burant, J. C.; Iyengar, S. S.; Tomasi, J.; Cossi, M.; Rega, N.; Millam, J. M.; Klene, M.; Knox, J. E.; Cross, J. B.; Bakken, V.; Adamo, C.; Jaramillo, J.; Gomperts, R.; Stratmann, R. E.; Yazyev, O.; Austin, A. J.; Cammi, R.; Pomelli, C.; Ochterski, J. W.; Martin, R. L.; Morokuma, K.; Zakrzewski, V. G.; Voth, G. A.; Salvador, P.; Dan nenberg, J. J.; Dapprich, S.; Daniels, A. D.; Farkas, O.; Foresman, J. B.; Ortiz, J. V.; Cioslowski, J.; Fox, D. J. Gaussian, Inc., Wallingford CT, 2010.

[16] Haydu, W.; Laudie, H.; Smith, O, H. *J. Chem. Eng. Data* **1973**, *18*, 373–376.

Chapter 3.

Synthesis, Optical Resolution, and Materials Properties of Spiro-conjugated Carbon-bridged *p*-Phenylenevinylene

3.1. Introduction

3.1.1. Spiro compounds

Spiro structure is one of the most important scaffolds for organic functional materials, where two π-conjugated planes are perpendicularly fixed via a spiro-central tetrahedral atom. The two π-conjugated systems connected by spiro-linkage are theoretically and experimentally found to electronically interact each other via through-space homoconjugation, so-called "spiroconjugation".[1] Because of this inter-subunit electronic interaction, spiro compounds show the increase or decrease of molecular orbital (MO) levels as a result of quantum interference of MOs of each π-units. For example, spiro[4,4]nonatetracene shows small energy splitting of HOMO–1 and HOMO, so-called "spiro-splitting", due to the constructive and destructive interferences of HOMOs of 1,3-butadiene units, respectively (Figure 3.1).

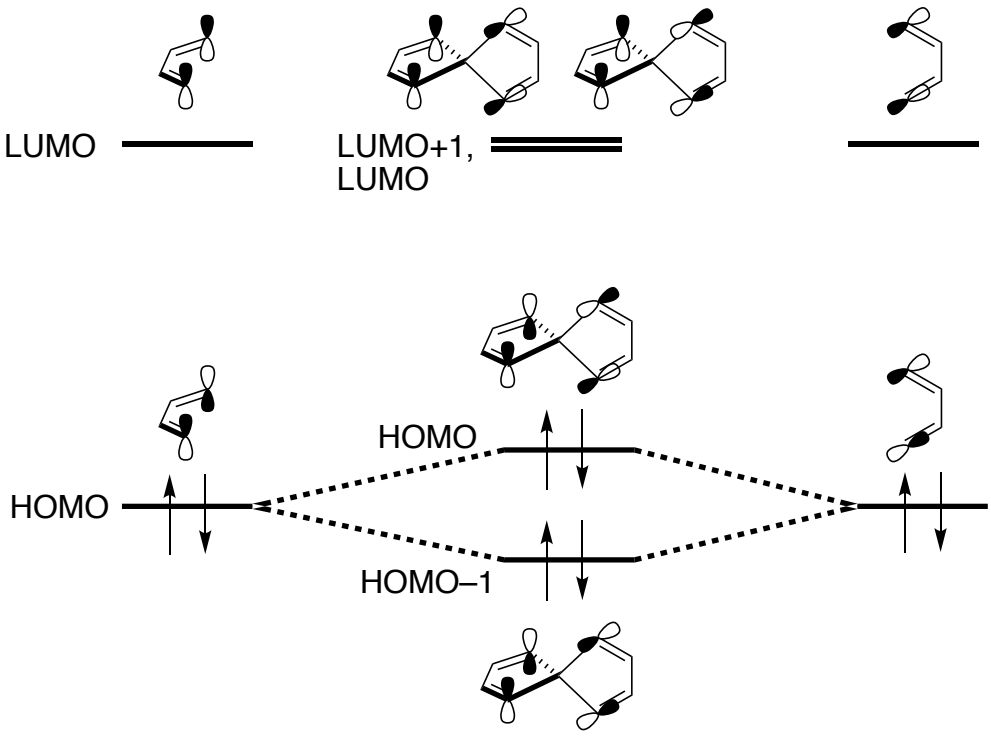

Figure 3.1. Spiroconjugation in spiro[4,4]nonatetracene.

Since the first report on synthesis of 9,9'-spirobifluorene by Clarkson and Gomberg in 1930 (Scheme 3.1),[2] many spiro compounds have been synthesized and investigated their materials properties. Spiro compounds have been utilized experimentally as carrier transporting materials in semiconducting devices[3,4] because of small reorganization energy, high morphological stability, and

solubility attributed by spiroconjugation and three-dimensional structure. The perpendicular spiro-conjugated π-systems also provide their potential use as single molecular junction[5] and singlet fission materials[6] because of the unique inter-subunit electronic coupling via spiroconjugation. The compounds are also applied as light-emitting scaffolds for thermally activated delayed fluorescence (TADF) materials,[7] where the spatial separation of HOMO and LUMO efficiently achieved thanks to perpendicular structure. Intramolecular charge separation via spiro-linkage is utilized to environment-sensing dyes[8] and biological probes[9] as well. In addition, spiro compounds can be chiral to be utilized in asymmetric synthesis.[10] In 1900, von Baeyer utilized spiro structure for the backbone of axially chiral phosphorus ligands.[11] The chirality and rigidness of spiro structure is suggested to efficiently improve the axial chirality and inhibit racemization by restriction of two connected rings. In 1992, Kumar *et al.* first demonstrated asymmetric reduction reaction by using chiral *cis,cis*-spiro[4,4]nonane-1,6-diol as a chiral auxiliary.[12] The application for molecular recognition is demonstrated by Alcazar *et al.* in 1992.[13]

Scheme 3.1. Synthesis of 9,9'-spirobifluorene reported by Clarkson and Gomberg.

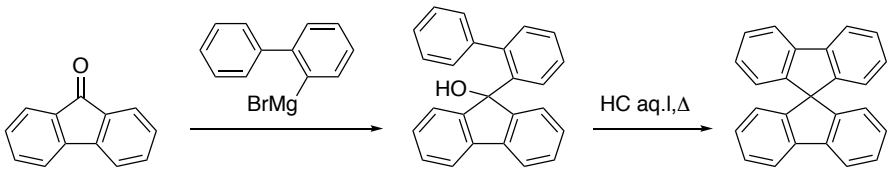

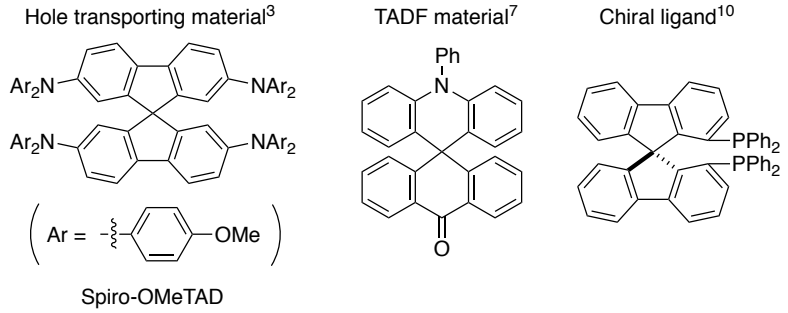

Figure 3.2. Examples of conventional organic spiro compounds for various applications.

Optically, spiro compounds have been investigated on their optical rotation and circular dichroism (CD)[3,14] since the measurements on 9,9'-spirobifluorene derivatives reported by Haas *et al.* in 1969[15] and 1971.[16] However, to the best of my knowledge, spiro compounds exhibiting circularly

polarized luminescence (CPL), one of the attractive photonic phenomena due to potential applications such as display devices,[17] CPL lasers,[18] and biological probes,[19] had been reported only in two papers[20] (Figure 3.3a) until 2017, when Nakano *et al.* developed the first carbon-centered spiro CPL compounds[21] based on thiophene and pyrrole (Figure 3.3b). While a simple chiral spiro hydrocarbon backbone had been desired for the potential of wide application, there still has been no report.

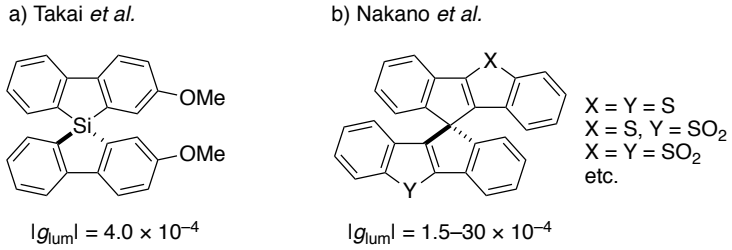

Figure 3.3. Examples of conventional chiral spiro CPL compounds.

3.1.2. Carbon-bridged oligo(*p*-phenylenevinylene)s

Organic π-conjugated molecules have been developed for the various purposes such as semiconducting[22] and optoelectronic materials.[23] The simple π-conjugated systems, such as polyacetylenes[24] and polyphenylenes,[25] can be constructed by connecting ethylene units or aromatic rings via chemical bonds and have applied in semiconducting devices. However, these compounds suffer from intramolecular rotation and structural disorder of π-units around single bonds to cause nonradiative deactivation, reduction of effective conjugation length, inefficient charge transfer, and insolubility.

An effective strategy to solve these problems is incorporation of bridging structures that fixes each π-unit by a bridging atom to inhibit the single bond rotations.[26] Our laboratory has developed a series of carbon-bridged oligo(*p*-phenylenevinylene)s (COPVs, Figure 3.4),[27] designed by bridging each units of oligo(*p*-phenylenevinylene) by sp^3 carbon atoms. Because of their rigid and flat π-conjugated system and full hydrocarbon backbone, COPVs exhibit very high fluorescence quantum yields ($\Phi_{FL} \sim 1.0$), high stability against thermal and photo stimuli, and fast carrier transport ability. Therefore, COPVs have been utilized in various applications such as hole transporting materials[28] and solid-state lasers.[29] However, high crystallinity and structural anisotropy of COPVs obstruct their applications in solution-processable devices.

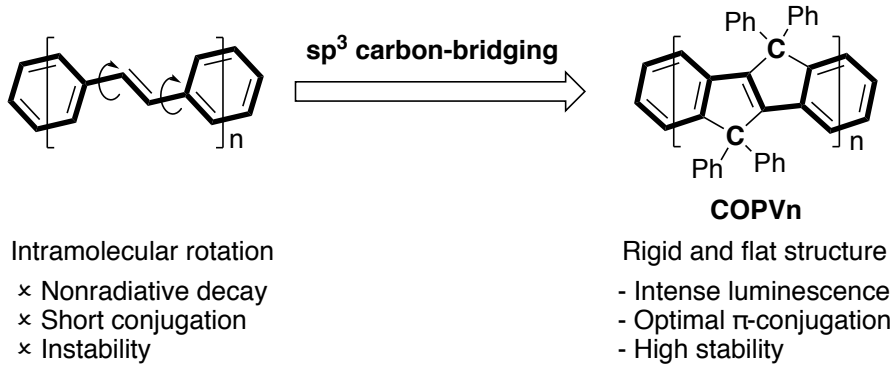

Figure 3.4. Structure and properties of oligo(*p*-phenylenevinylene) and COPVn.

3.1.3. Spiro-conjugated carbon-bridged *p*-phenylenevinylene: Chapter outline

Inspired by the concept that the materials properties derived from molecular structure can be summed up as suggested in Chapter 2, I hypothesized that a new hydrocarbon π-scaffold possessing the advantages of both of spiro compound and COPV could be achieved by combining these molecular structure in one molecule. Considering the spiro central atom is sp^3 carbon, I realized that COPV backbone and spiro-linkage structure could be combined via the bridging carbon atom.

Based on this idea, I envisioned the design and synthesis of spiro-conjugated carbon-bridged *p*-phenylenevinylene (spiro-CPV, Figure 3.5), a C_2-symmetric spiro-conjugated carbocyclic framework, where two COPV units are connected in perpendicular via a sp^3 carbon atom. Because of the axial chirality and rigid π-planer units, spiro-CPV would exhibit chiroptical properties with high Φ_{FL} as well as the properties derived from each structure, such as high stability, inter-subunit electronic interaction via spiroconjugation, and high solubility. In this chapter, the synthesis and properties of spiro-CPV is reported. To the best of my knowledge, spiro-CPV is the first chiral spiro hydrocarbon investigated on CPL property. In section 3.2, the synthesis, optical resolution, and derivatization of spiro-CPV are described with its crystal structure. Photophysical properties, molecular orbital energy levels, and stabilities are described in Section 3.3–3.5 respectively, to demonstrate the properties expected in molecular design. Section 3.6 provides the summary of this chapter.

It should be noted here that the crystal structure in Section 3.2.1 is obtained collaboratively with Dr. Yuki Itabashi. I appreciate very much for his help.

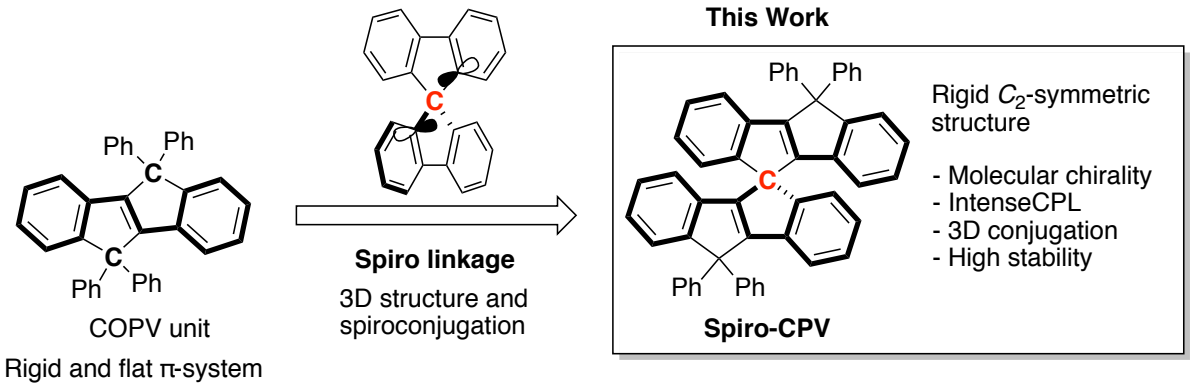

Figure 3.5. Molecular design of spiro-CPV.

3.2. Synthesis and derivatization

3.2.1. Synthesis and optical resolution of spiro-CPV

For the efficient synthesis of compound **A**, I chose the convergent retrosynthetic route (Scheme 3.2) via nucleophilic addition of 3-lithioindene to ketone intermediate that can also be synthesized from 3-lithioindene. Although Dr. Qifan Yan previously tried the synthesis of the ketone by using Friedel-Crafts type intramolecular cyclization of indeno-3-carboxylic acid in acidic condition (Scheme 3.3),[30] undesired products were mainly obtained because of rearrangement of phenyl group and addition of hydroxyl group by aqueous quenching. In order to avoid these problems, therefore, I utilized palladium-catalyzed cyclocarbonylation reaction (Scheme 3.4) developed by Larock *et al.*[31] where is basic condition to cause no migration of phenyl group.

Scheme 3.2. Retrosynthetic route of spiro-CPV.

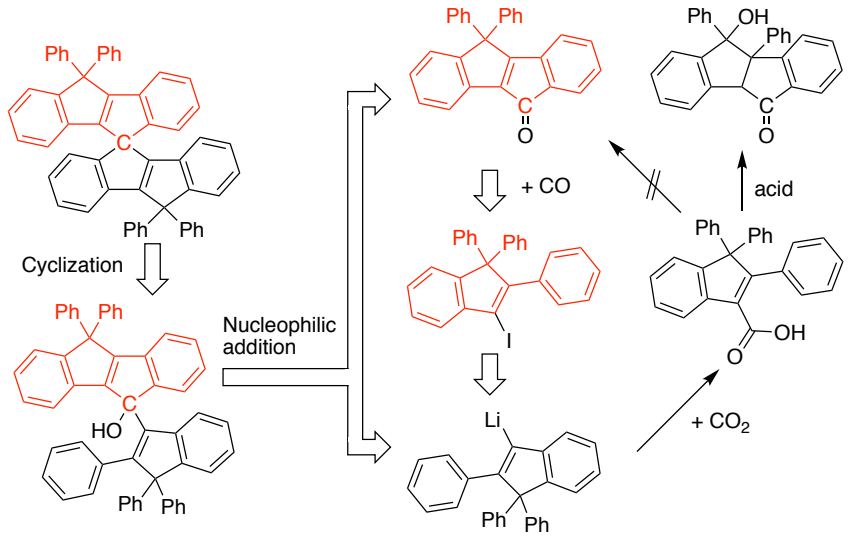

Scheme 3.3. Friedel-Crafts type cyclization of 2-phenylindeno-3-carboxylic acid and 1,2-migration.

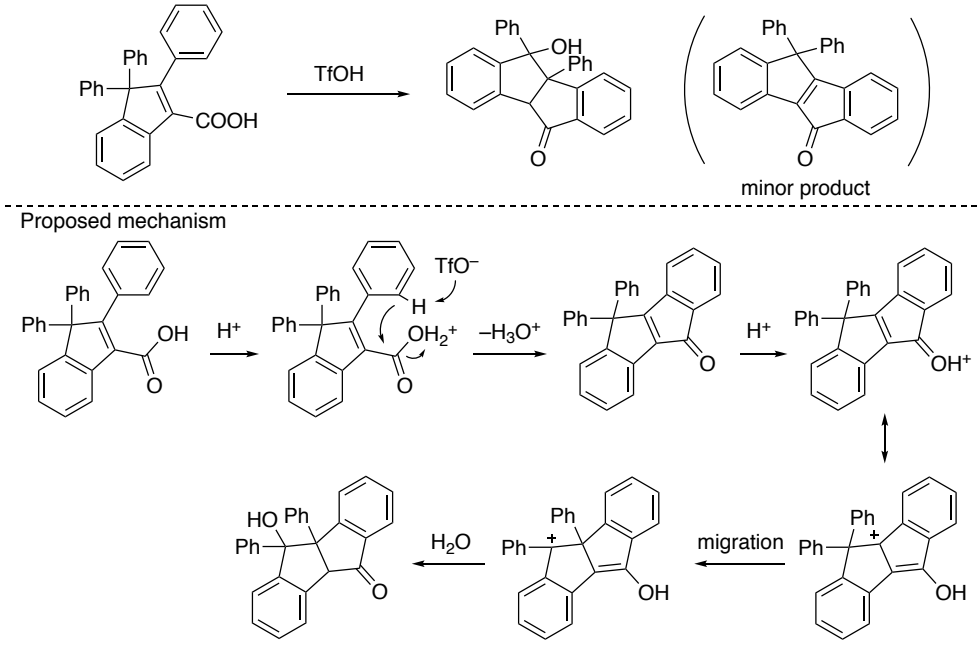

Scheme 3.4. Palladium-catalyzed cyclocarbonylation reported by Larock *et al.* and proposed mechanism.

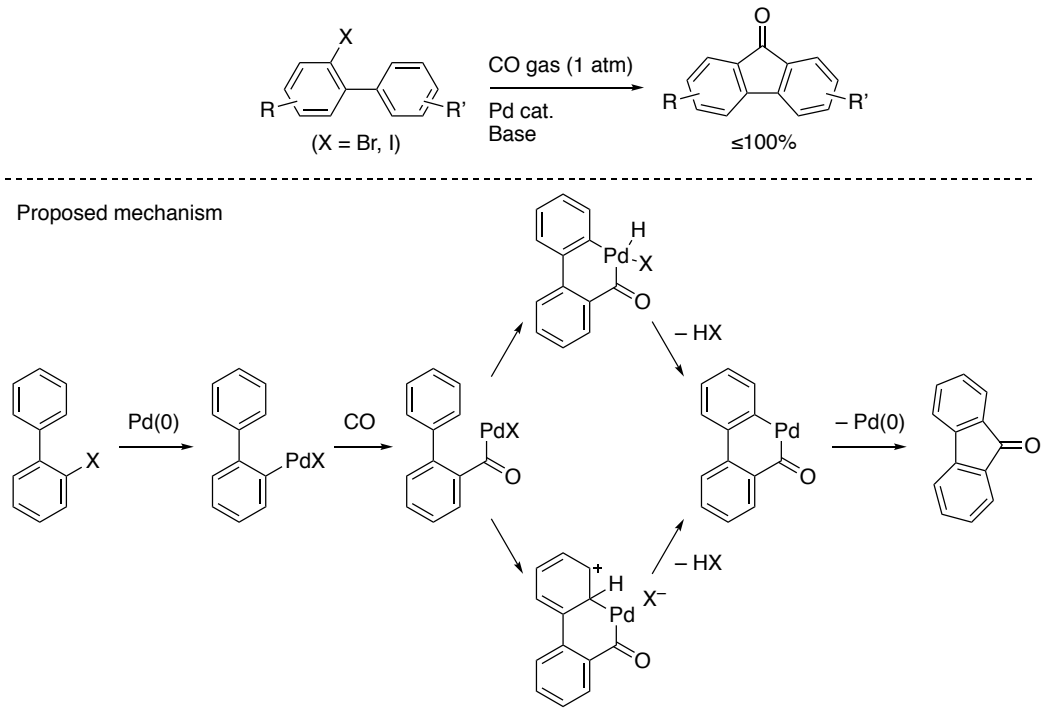

Based on the retrosynthetic route, I successfully obtained the target compound **A** in seven steps from commercially available materials (Scheme 3.5a). Firstly, I synthesized **11** from the commercially available 2-bromo-1-iodobenzene in three steps. Then, cyclization of **11** gave

3-lithioindene **12** by using lithium naphthalenide (LiNaph), as previously described.[27] The addition of 1,2-diiodoethane to **12** afforded **13**, which is used for palladium-catalyzed cyclocarbonylation to access the ketone **14**. Nucleophilic addition of **12** to **14** and following intramolecular cyclization with BF_3•Et_2O afforded spiro-CPV (**A**) in the yield of 67%. Noteworthily, the whole steps of this synthetic route can be conducted without column chromatographic purification, enabling gram-scale synthesis of **A** up to 7 g. Noteworthily, the 1,2-migration of phenyl group of **14** takes place under Lewis acidic and Brønsted acidic condition (Scheme 3.6), suggesting the expediency of this synthetic route.

Scheme 3.5. a) Synthesis of spiro-CPV (**A**) and b) optical resolution via dihydroxy derivative **10**.

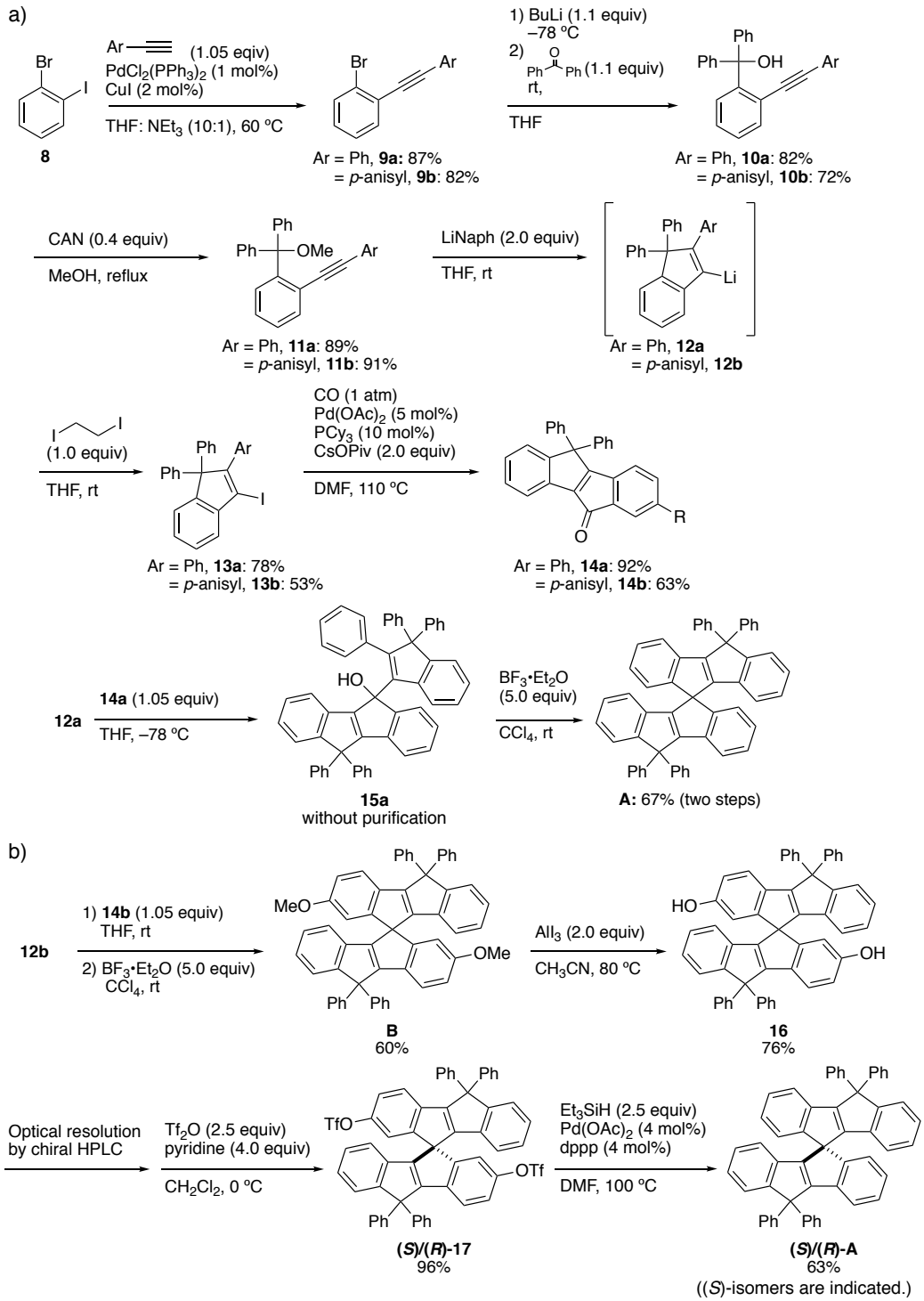

Scheme 3.6. Rearrangement of **14a** in acidic conditions.

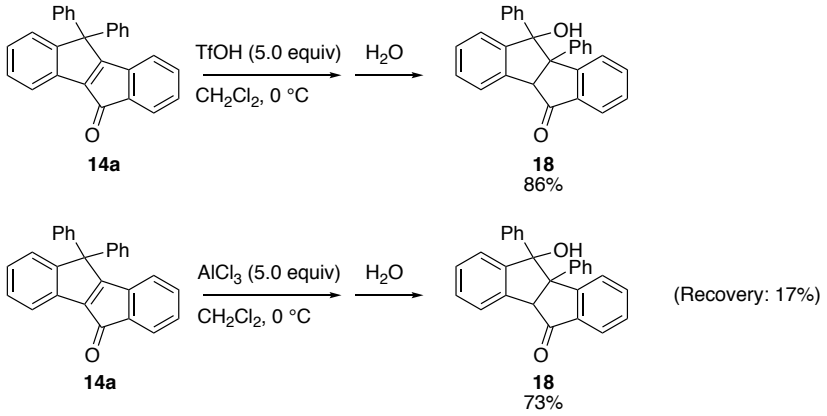

Enantiomerically pure **A** was obtained via optical resolution of racemic dihydroxy derivative **16**, synthesized from dimethoxy derivative **B**, with preparative chiral HPLC (Scheme 3.5b), which is scalable up to a hundred mg-scale. Triflation of chiral **16** and palladium-catalyzed hydration of triflate groups[32] on **17** afforded chiral **A**, used for further investigation on chiroptical properties of spiro-CPV.

X-ray single crystal analysis of a single crystal of compound **A**, obtained from racemic solution as a conglomerate, confirmed that the spiro structure fixes two COPV units via a bridging sp^3 carbon to form an perpendicular dihedral angle of 89.8° (Figure 3.6). The molecules in crystal are packed by intermolecular CH–π interaction, as reflected in an intermolecular C(–H)/π-plane distance of 2.63 Å.

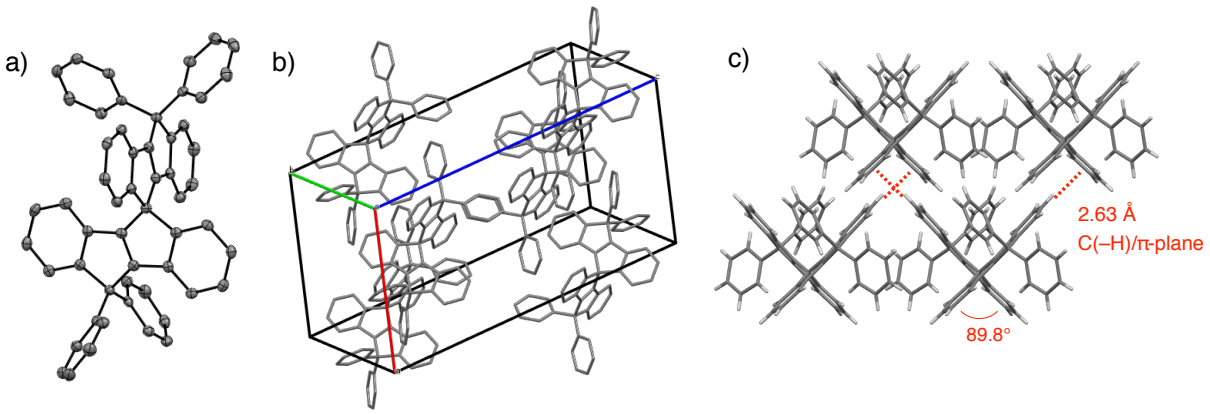

Figure 3.6. Crystal structure of (*R*)-**A**. a) Oak Ridge thermal ellipsoid plot (ORTEP) drawing with thermal ellipsoids set to 50% probability. Hydrogen atoms and solvent molecules are omitted for clarity. b) Packing structure of (*R*)-**A** in crystal. Hydrogen atoms and solvent molecules are omitted for clarity. c) Intermolecular C(–H)/π-plane distance and the dihedral angle of two COPV units.

3.2.2. Regioselective derivatization of spiro-CPV

The simple functionalization protocols improve the utility of spiro-CPV backbone as a spiro-conjugated building block for various applications. Bromination[33] and iodination[34] proceeded regioselectively at 2 and 7 positions for each COPV units to afford compound **19** and **20** in excellent yields. Miyaura borylation[35] of the tetra-bromide took place to afford **21** in moderate yield (Scheme 3.7a), which allows further functionalization. The dimethoxy derivative **B** undergoes dibromination to afford **22** quantitatively (Scheme 3.7b) as well, and following triflation to compound **24** allows regioselective and flexible derivatization by the choice of reaction condition.[36]

Scheme 3.7. Derivatization of spiro-CPV. a) Tetra-bromination, iodination, and borylation of **A**. b) Dibromination and triflation of **B**.

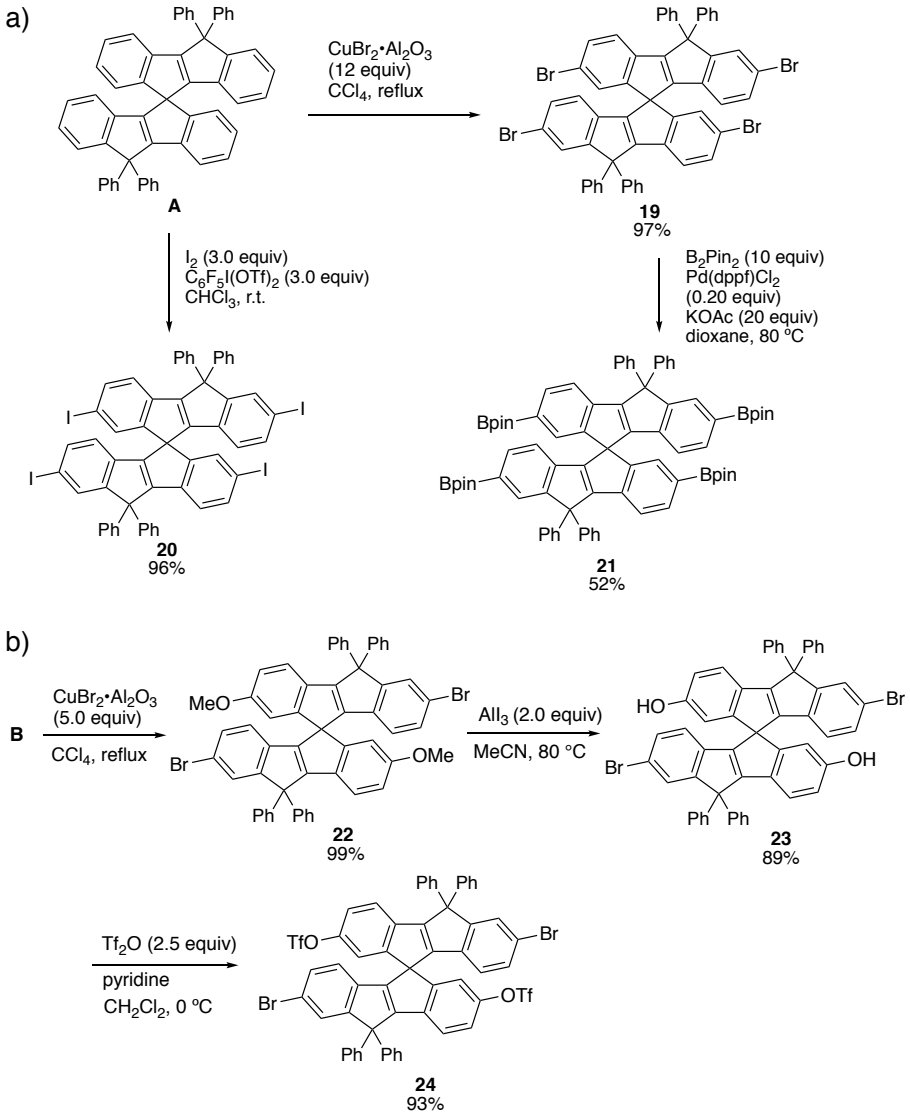

3.3. Photophysical properties

Spiro-CPV **A** exhibited similar absorption and fluorescence spectra to COPV1 (Figure 3.7). Small Stokes shift indicates that compound **A**, as well as COPV1, is so rigid that it undergoes little geometry reorganization upon excitation. The maximum absorption peak (λ_{abs}) showed small bathochromic shift by 3 nm from that of COPV1, which suggests the orbital interaction between the two π-planes of **A**. The larger extinction coefficient of **A**, compared to that of COPV1, is possibly attributed to the doubled π-systems and the lower symmetry of C_2-symmetric **A** that activate the forbidden electron transition in C_{2h}-symmetric COPV1. Compound **A** exhibits intense fluorescence with a quantum yield of $\Phi_{FL} = 0.74$ in dichloromethane. Taking account its fluorescence lifetime of $\tau_{FL} = 5.88$ ns (Table 3.1**,** Figure 3.8), I attribute this intense photoemission to the rigid and all-carbon structure, suppressing nonradiative thermal deactivation pathways. A rather intense emission ($\Phi_{FL} = 0.12$) was observed for the powder of **A**, suggesting the possibility of application in a solid-state laser, where the parent COPVs already demonstrated its utility.[29]

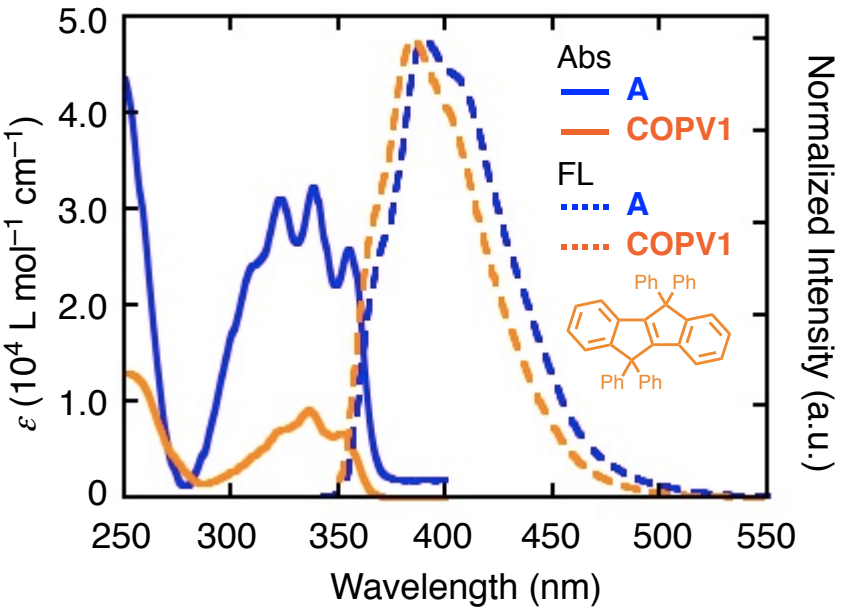

Figure 3.7. Absorption and fluorescence spectra of **A** and COPV1 in dichloromethane (1.0×10^{-5} M for absorption and 1.0×10^{-6} M for fluorescence).

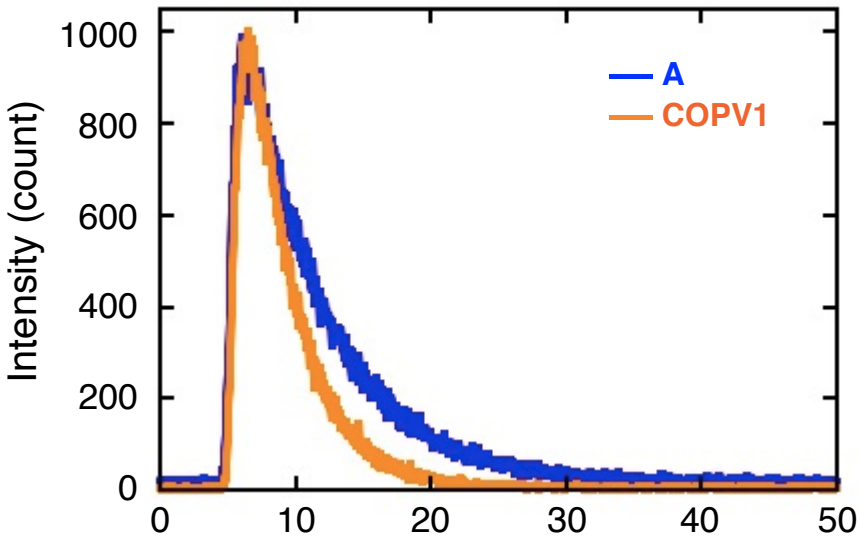

Figure 3.8. Fluorescence lifetime of **A** and COPV1 in dichloromethane (1.0×10^{-6} M).

Table 3.1. Photophysical properties of **A** and COPV1 in dichloromethane

	λ_{abs}[a] (nm)	λ_{FL}[b] (nm)	$\Delta\nu$[c] (nm)	Φ_{FL}[d]	τ[e] (ns)	k_r[f] (10^8 s^{-1})	k_{nr}[g] (10^7 s^{-1})	$\lvert g_{abs}\rvert$[h] (10^{-4})	$\lvert g_{lum}\rvert$[h] (10^{-4})	$\lvert[\alpha]_D^{20}\rvert$ (*c*)[i]
A	355, 338, 324	388	64	0.74	5.68	1.30	4.58	8.4	6.3	350 (0.052)
COPV1	352, 336, 324	384	60	1.00	3.06	3.27	0	-	-	-

[a] Absorption maximum wavelengths. [b] Fluorescence maximum wavelengths. [c] Stokes shift. [d] Fluorescence quantum yield determined by using the absolute method. [e] Fluorescence lifetime. [f] Radiative rate constant. [g] Nonradiative rate constant. [h] The dissymmetric factors. Wavelength for $|g_{abs}|$ is 339 nm; wavelength for $|g_{lum}|$ is 416 nm. [i] Specific rotation. Concentration (g mL^{-1}) in parentheses.

Enantiomerically pure **A** is CD and CPL active. The (+)-isomer of **A** (Figure 3.9, red) exhibited three large positive Cotton effects at 355, 338, and 251 nm, and several negative ones at 315–260 nm in CD measurement. Its (–)-enantiomer (Figure 3.9, blue) showed a mirror image CD spectrum. Based on the observed Cotton effect, *R* and *S* stereochemistry were assigned to the (+) and (–) isomers, respectively.[21] The absorption dissymmetry factor ($|g_{abs}|$) of **A** was found to be 8.4×10^{-4} (Table 3.1). The dissymmetry factor in luminescence ($|g_{lum}| = 6.3 \times 10^{-4}$) is comparable to the conventional organic CPL small molecules (e.g., helicenes and binaphthyls).[37]

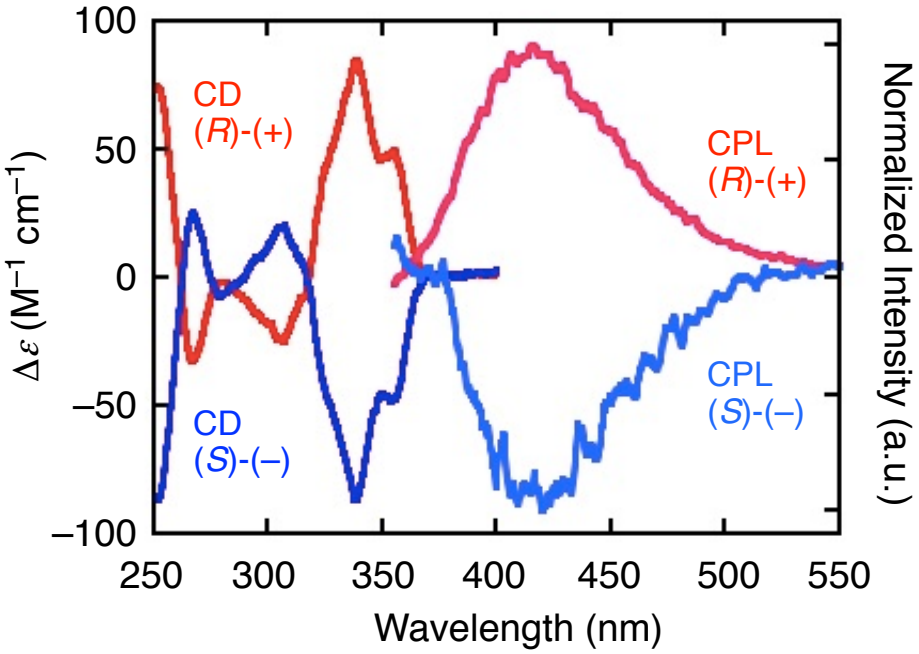

Figure 3.9. CD and CPL spectra of **A** in dichloromethane (1.0×10^{-5} M).

3.4. Spiroconjugation: investigation on energy levels

In order to confirm the electronic interaction between two COPV units of **A**, electrochemical properties were investigated (Table 3.2). Photoelectron yield spectroscopy (PYS, Figure 3.10) measurement of a spin-coated film on an ITO substrate gave a smaller ionization potential (IP) for **A** (5.96 eV) than that of COPV1 (6.11 eV). This result suggests that a radical cation gets stabilized by introduction of spiro moiety, possibly thanks to spiroconjugation. In cyclic voltammetry (CV) and differential pulse voltammetry (DPV), the first oxidation peak of **A** (Figure 3.11) appeared at 0.89 V vs Fc/Fc^+, while that of COPV1 was at a lower potential of 0.86 V vs Fc/Fc^+ (Table 3.2). The optical bandgap of **A** (3.32 eV), determined from the offset of absorption spectrum, was smaller than that of COPV1 (3.35 eV). It also suggests the destabilization of HOMO by the quantum interference around spiro-linkage.[1]

Table 3.2. Electrochemical properties and calculated HOMO–LUMO energies of **A** and COPV1

	IP[a] (eV)	E_{OX}[b] (V vs Fc/Fc^+)	OBG[c] (eV)	$E_{H,\,calc}$[d] (eV)	$E_{L,\,calc}$[e] (eV)	ΔE_{H-L}[f] (eV)	$\Delta E_{H(H-1)-H}$,[g] (eV)
A	5.96	0.89	3.32	–5.13	–1.25	3.89	0.25
COPV1	6.11	0.86	3.35	–5.24	–1.25	3.99	1.06

[a] Ionization potential. [b] Oxidation potential (0.5 mM in dichloromethane with 0.1 M Bu_4NPF_6 electrolyte). [c] Optical bandgap. [d] Calculated HOMO level. [e] Calculated LUMO level. [f] HOMO–LUMO gap calculated at the B3LYP/6-31G(d,p) level of theory. [g] (HOMO–1)–HOMO gap calculated at the B3LYP/6-31G(d,p) level of theory.

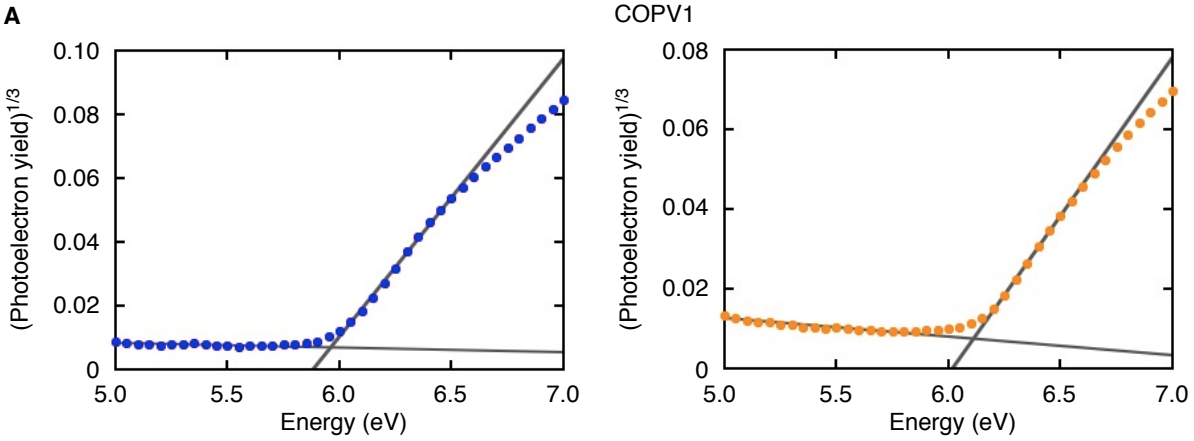

Figure 3.10. PYS data of **A** and COPV1 films spin-coated on ITO surface.

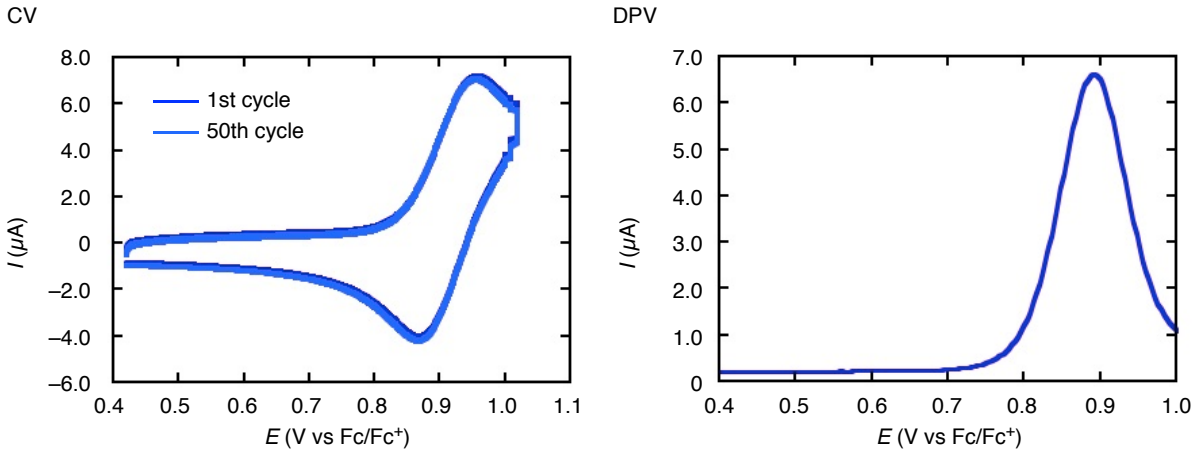

Figure 3.11. Cyclic voltammogram and differential pulse voltammogram of **A** in dichloromethane (0.5 mM solution with 0.1 M Bu_4NPF_6 electrolyte)

Computational molecular orbitals for an optimized structure at the B3LYP/6-31G(d,p) level of theory (Figure 3.12) supported spiroconjugation between two COPV1 units. The pair of molecular orbitals in opposite signs for the two π-planes in HOMO causes destructive interference to destabilize HOMO level of **A**, while the orbitals in HOMO–1 have the same symmetry to afford stabilization of HOMO–1 level via constructive interference[1] (Table 3.2, Figure 3.13). Compared to those of COPV1, the higher HOMO level and smaller HOMO–LUMO gap of **A** accord with the experimental IP and optical bandgap, which supports the inter-subunit electronic interaction via spiroconjugation. In contrast to the large calculated (HOMO–1)–HOMO gap of 1.06 eV for COPV1, the energy splitting for **A** (0.25 eV) is close to the values previously reported for spiro compounds such as 9,9′-spirobifluorene (0.30 eV)[38] and the sulfur-bridged spiro compounds[21] (0.27–0.22 eV).

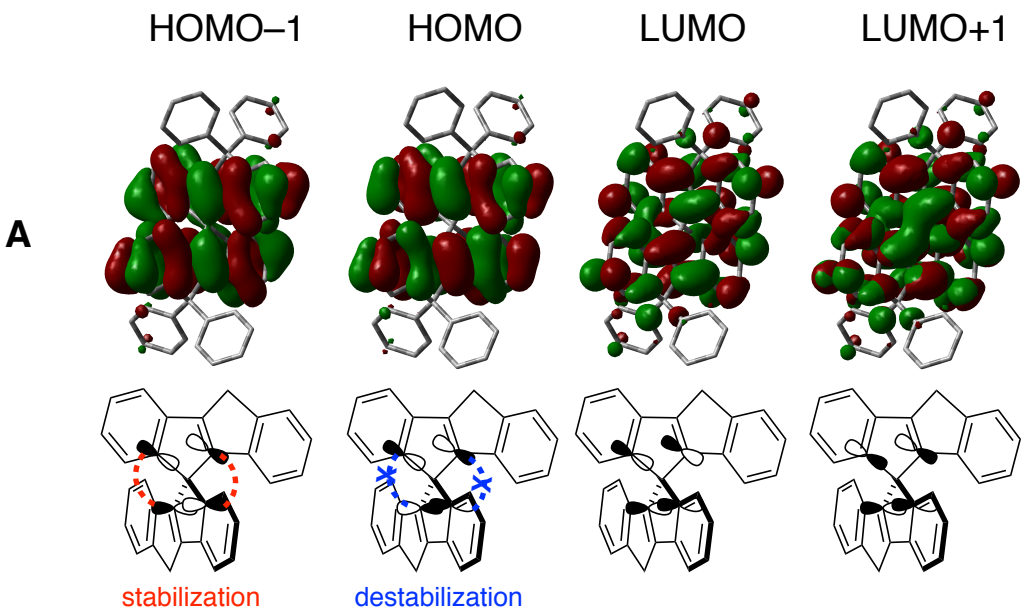

Figure 3.12. Computational distributions of each molecular orbitals in **A** and quantum interferences around spiro center.

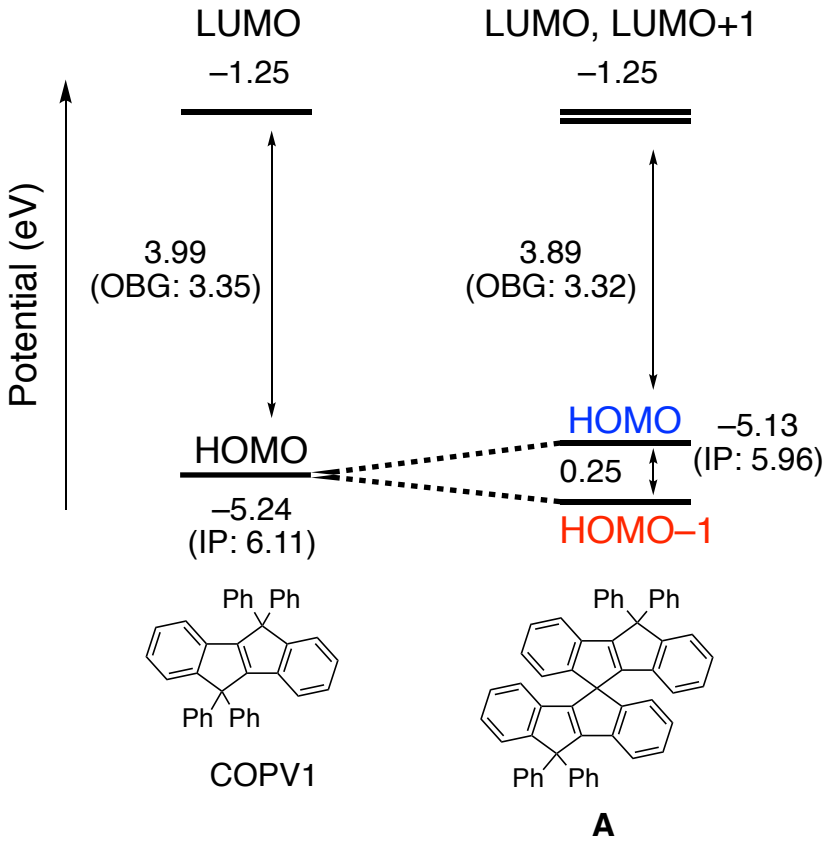

Figure 3.13. Calculated and experimental (in parentheses) HOMO–LUMO energies of **A** and COPV1.

3.5. Thermal- and photo-stability

Spiro-CPV is highly stable against thermal and photo-stimuli. Compound **A** can be stored in air for at least 22 months with no change (based on ^{1}H-NMR data). Thermogravimetric analysis (TGA) and differential scanning calorimetry (DSC) under nitrogen atmosphere (Figure 3.14a) indicated that **A** undergoes neither isomerization nor phase transition before decomposition (5% weight loss at T_{d5} = 335 °C). Considering T_{d5} of COPV1 at 328 °C,[27] the spiro linkage does not affect on thermal stability, or rather increase slightly. The trace of absorbance change of **A** and COPV1 in dichloromethane under irradiation with a Xe lamp (Figure 3.14b, Figure 3.15), revealed that **A** has better photostability than COPV1. Considering that COPVs are applicable for solid-state lasers,[29] spiro-CPV and its derivatives would be a promising candidate for laser applications as well.

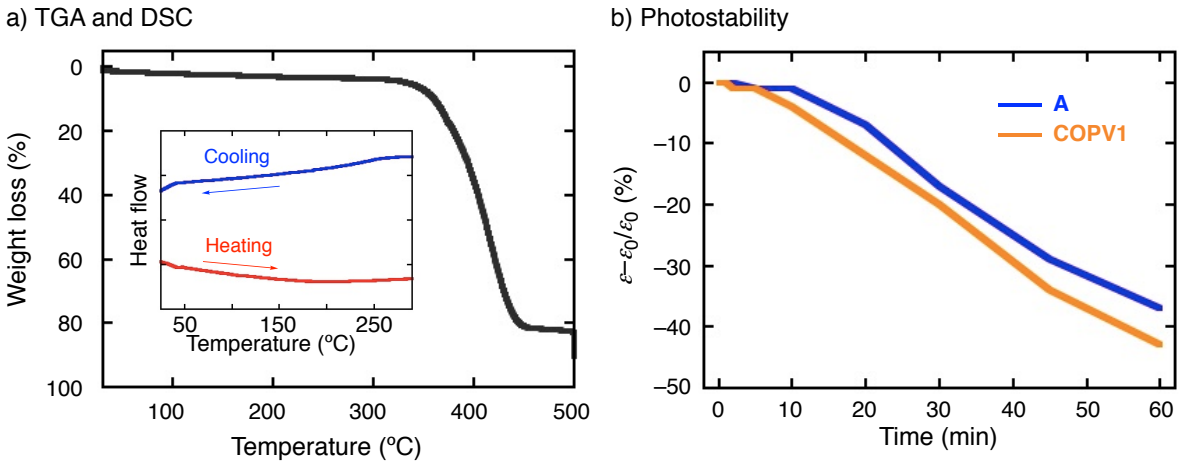

Figure 3.14. a) TGA and DSC (inset) curve of **A** under N_2 atmosphere. b) Photostability of **A** and COPV1 in dichloromethane under irradiation with a Xe lamp (300W).

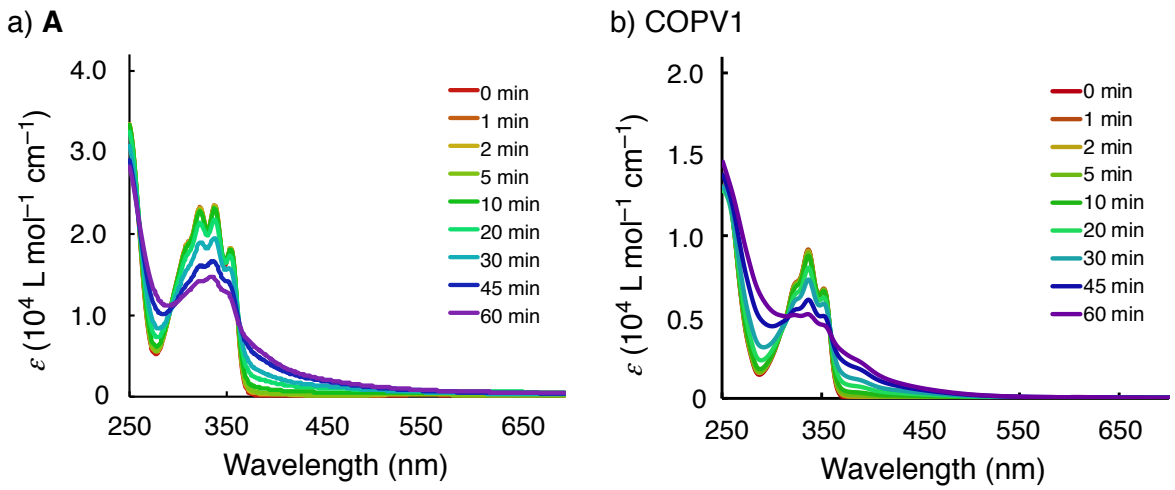

Figure 3.15. The trace of absorption spectra of a) **A** and b) COPV1 in dichloromethane (1.0×10^{-5} M) under irradiation with a Xe lamp (300 W).

3.6. Summary

In summary, I have synthesized spiro-CPV to prove that the properties derived from both spiro structure and COPV could be compatible in one molecule. Spiro-CPV **A** was successfully obtained through the synthetic route via Pd-catalyzed cyclocarbonylation that afforded the ketone intermediates without the problematic rearrangement. The novel spiro backbone undergoes regioselective halogenation to allow further derivatizations. Enantiomerically pure **A** exhibited CD and CPL with high fluorescence quantum yield thanks to its molecular chirality and rigid COPV moiety. The investigation on molecular orbital energy levels of **A** showed smaller HOMO–LUMO gap and higher HOMO level than COPV1, suggesting the inter-subunit electronic interaction between two COPV units via spiroconjugation. The spiro-conjugated carbocycle showed high thermal and photostability, allowing the applications into optoelectronic device materials.

3.7. Experimental section

3.7.1. Synthesis

General consideration

All the reactions dealing with air- or moisture-sensitive compounds were carried out in a dry reaction vessel under a positive pressure of N_2 or Ar gas. Air- and moisture-sensitive liquids and solutions were transferred via syringe or Teflon cannula. Analytical thin-layer chromatography (TLC) was performed using glass plates pre-coated with 0.25 mm, 230–400 mesh silica gel impregnated with a fluorescent indicator (254 nm). Thin-layer chromatography plates were visualized by exposure to ultraviolet light (UV). Organic solutions were concentrated by rotary evaporation at ca. 15 Torr (evacuated with a diaphragm pump). Flash column chromatography was performed as described by Still *et al*.[39], employing Kanto Silica gel 60 (spherical, neutral, 140–325 mesh).

Unless otherwise noted, commercial reagents were purchased from Tokyo Kasei Co., Aldrich Inc., and other commercial suppliers and used as purchased. Anhydrous solvents were purchased from Kanto, and purified by a solvent purification system (GlassContour) equipped with columns of activated alumina and copper catalyst prior to use.

NMR spectra were recorded using a JEOL ECZ-500 (^{1}H NMR, 500 MHz; ^{13}C NMR, 125 MHz) NMR spectrometer. Chemical data for protons are reported in parts per million (ppm, δ scale) downfield from tetramethylsilane and are referenced to the residual protons in the NMR solvent ($CDCl_3$: δ 7.26, CD_2Cl_2: δ 5.32). Chemical data for carbons are reported in parts per million (ppm, δ scale) downfield from tetramethylsilane and are referenced to the carbon resonance of the solvent ($CDCl_3$: δ 77.0, CD_2Cl_2: δ 54.0). The data are presented as follows: chemical shift, multiplicity (s = singlet, d = doublet, t = triplet, m = multiplet and/or multiple resonances, br = broad), coupling constant in Hertz (Hz), and integration. Melting points of solid materials were determined on a Mel-Temp II capillary melting-point apparatus and are uncorrected. Mass spectra were obtained on JEOL AccuTOF JMS-T100LC (APCI) mass spectrometer. High-resolution mass spectra were obtained with a calibration standard of reserpine. HPLC analyses were conducted with a SHIMADZU Prominence (HPLC pump: LC-20AD; auto sampler: SIL-20AC; degasser: DGU-20A; column oven: CTO-20AC; diode array detector detector: SPD-M30A) equipped with DAICEL CHIRALPAK IF columns (4.6 mm x 250 mm).

Synthetic procedures

3-Iodo-1,1,2-triphenyl-1*H*-indene (**13a**)

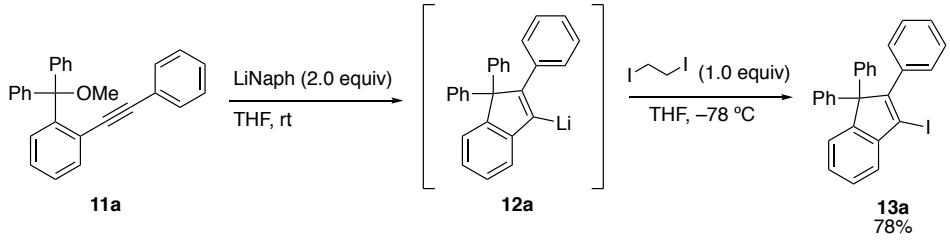

11a **12a** **13a** 78%

A mixture of granular lithium (140 mg, 20 mmol) and naphthalene (19.2 g, 18 mmol) in THF (20 mL) was stirred at room temperature under argon atmosphere for 4 h. The LiNaph/THF was added to a solution of 1-phenylethynyl-2-diphenylhydroxymethylbenzene (**11a**, 3.36 g, 9.0 mmol) in THF (20 mL) at room temperature, and the resulting mixture was stirred for 1 h. The resulting mixture was cooled down and 1,2-diiodoethane (3.04 g, 10.8 mmol) was added at –78 ºC. The reaction mixture was gradually warmed to ambient temperature, stirred another 1 h, and then quenched with aqueous $Na_2S_2O_3$ solution. The organic layer was extracted with EtOAc, dried over anhydrous Na_2SO_4, and evaporated *in vacuo*. The crude mixture was purified with reprecipitation from $CHCl_3$/MeOH to afford compound **13a** (3.31 g, 78%) as a white solid. The ^{1}H NMR spectrum of compound **13a** was in agreement with the literature.[27]

10,10-Diphenylindeno[2,1-*a*]inden-5(10*H*)-one (**14a**)

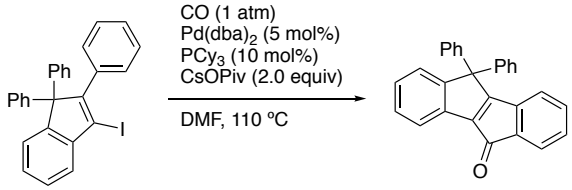

13a **14a** 92%

A solution of 3-iodo-1,1,2-triphenyl-1*H*-indene (**13a**, 920 mg, 2.0 mmol), $Pd(dba)_2$ (92 mg, 0.1 mmol), tricyclohexylphosphine (56 mg, 0.2 mmol) and anhydrous cesium pivalate (936 mg, 4.0 mmol) in DMF (20 mL) was stirred under CO gas atmosphere at 110 ºC for 5 h. The resulting red mixture was allowed to cooled down to ambient temperature and quenched with water. The organic layer was extracted with Et_2O, washed with brine, dried over anhydrous $MgSO_4$ and evaporated *in vacuo*. The crude mixture was purified by reprecipitation from DMF/H_2O afforded compound **14a** (681 mg, 92%) as a reddish orange powder. Mp: 186–188 ºC; ^{1}H NMR (500 MHz, $CDCl_3$) δ 6.92 (dd, J = 6.3, 1.1 Hz, 1H), 7.13–7.25 (m,

3H), 7.27–7.29 (m 10H), 7.33 (td, J = 7.4, 1.1 Hz, 1H), 7.39 (d, J = 8.0 Hz, 1H), 7.45 (dd J = 6.3, 1.7 Hz, 1H), 7.75 (d, J = 7.4 Hz, 1H); ^{13}C NMR (125 MHz, CD_2Cl_2) δ 64.8, 121.1, 121.6, 123.1, 125.4, 126.9, 127.5, 127.8, 128.5, 128.7, 128.9, 123.2, 134.8, 136.4, 139.6, 139.8, 141.4, 155.7, 175.7, 190.9; HRMS (APCI+) calcd for $C_{28}H_{18}O$ (M+H): 371.1436; found: 371.1423.

10,10,10',10'-tetraphenyl-10*H*,10'*H*-5,5'-spirobi[indeno[2,1-*a*]indene] (spiro-CPV, **A**)

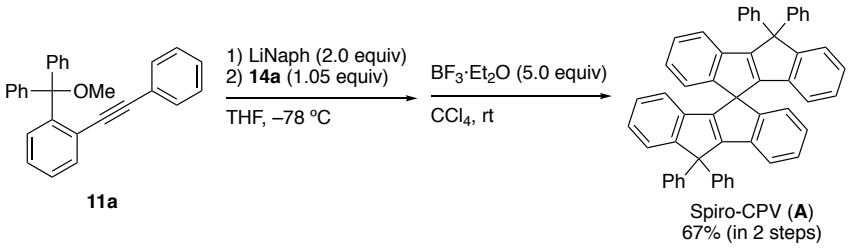

A mixture of granular lithium (208 mg, 30 mmol) and naphthalene (3.19 g, 30 mmol) in THF (60 mL) was stirred at room temperature under argon atmosphere for 4 h. The LiNaph/THF was added to a solution of 1-phenylethynyl-2-diphenylhydroxymethylbenzene (**11a**, 5.60 g, 15 mmol) in THF (100 mL) at room temperature, and the resulting mixture was stirred for 1 h. The resulting mixture was cooled down and added 10,10-diphenylindeno[2,1-*a*]inden-5(10*H*)-one (**14a**, 5.83 g, 15.8 mmol) at room temperature. The reaction mixture was gradually warmed to ambient temperature, stirred for another 1 h, and then quenched with water. The organic layer was extracted with CH_2Cl_2, dried over anhydrous Na_2SO_4, and evaporated *in vacuo*. The resulting crude mixture was dissolved in CH_2Cl_2 and added $BF_3 \cdot Et_2O$ (213 mg, 1.5 mmol) at room temperature. After stirred for 10 min, the resulting mixture was quenched a few drops of MeOH and evaporated *in vacuo*. The crude mixture was purified by reprecipitation from CH_2Cl_2/MeOH to afford spiro-CPV (**A**, 7.00 g, 67% in 2 steps) as a white solid. Mp: > 315 ºC (decomposition); ^{1}H NMR (500 MHz, $CDCl_3$) δ 6.18 (d, J = 7.4 Hz, 2H), 6.83 (t, J = 7.7 Hz, 2H), 6.87 (d, J = 7.4 Hz, 2H), 7.00 (q, J = 7.1 Hz, 4H), 7.20 (t J = 7.4 Hz, 2H), 7.28–7.38 (m, 18H), 7.39 (d, J = 8.0 Hz, 2H), 7.52 (d, J = 8.0 Hz, 4H); ^{13}C NMR (125 MHz, CD_2Cl_2) δ59.8, 64.0, 119.8, 120.8, 123.2, 124.8, 125.8, 125.9, 127.0, 127.09, 127.14, 127.7, 128.3, 128.4, 128.6, 137.5, 140.3, 142.6, 143.0, 149.1, 149.7, 156.7, 158.9; HRMS (APCI+) calcd for $C_{55}H_{36}$ (M): 696.2817; found: 696.2846.

1-(4-Methoxyphenyl)ethynyl-2-diphenylhydroxybenzene (**10b**)

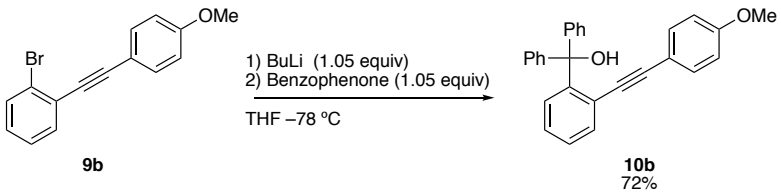

9b **10b** 72%

Butyllithium (8.49 mL, 1.60 M) was dropwisely added into a solution of 1-bromo-2-((4-methoxyphenyl)ethynyl)benzene (**9b**, 3.60 g, 12.6 mmol) in THF (100 mL) at –78 ºC and stirred for 30 min. The resulting mixture was added benzophenone (2.40 g, 13.2 mmol) and stirred for 1 h. The reaction mixture was allowed to warm gradually to ambient temperature and then was added water. The organic layer was extracted with dichloromethane, dried over anhydrous Na_2SO_4, and evaporated *in vacuo*. The crude material was purified by reprecipitation in $CHCl_3$/MeOH to afford the compound **10b** (3.54 g, 72%) as a white solid. Mp: 118–120 ºC; ^{1}H NMR (500 MHz, CD_2Cl_2) δ 3.79 (s, 3H), 4.95 (s, 1H), 6.67 (d, *J* = 8.0 Hz, 1H), 6.79 (dd, *J* = 6.9, 2.3 Hz, 2H), 7.03 (d, *J* = 8.6 Hz, 2H), 7.17 (td, *J* = 7.7, 1.1 Hz, 1H), 7.27–7.38 (m, 11H), 7.59 (dd, *J* = 7.4, 1.1 Hz, 1H); ^{13}C NMR (125 MHz, CD_2Cl_2) δ 56.6, 82.7, 87.3, 97.7, 144.2, 144.3, 122.0, 127.5, 127.7, 127.76, 127.83, 128.1, 128.3, 129.6, 133.1, 134.2, 146.7, 149.7, 149.3, 160.4; HRMS (APCI+) calcd for $C_{28}H_{22}O_2$ (M): 390.1620; found: 390.1609.

1-(4-Methoxyphenyl)ethynyl-2-diphenylhydroxymethylbenzene (**11b**)

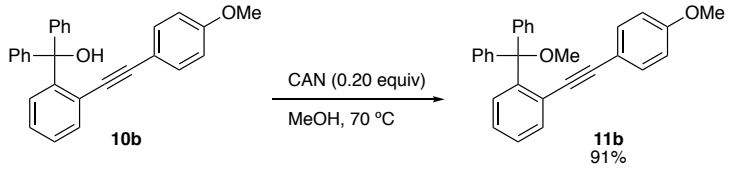

10b **11b** 91%

A suspension of 1-(4-methoxyphenyl)ethynyl-2-diphenylhydroxybenzene (**10b**, 600 mg, 1.54 mmol) in MeOH (20 mL) was treated with ceric ammonium nitrate (CAN, 168 mg, 0.20 mmol) and heated to 70 ºC for 12 h. The resulting mixture was allowed to cool down to ambient temperature. The precipitation in the mixture was collected by filtration and then washed with MeOH to afford compound **11b** (567 mg, 91%) as a white solid. Mp: 133–134 ºC; ^{1}H NMR (500 MHz, CD_2Cl_2) δ 3.04 (s, 3H), 3.78 (s, 3H), 6.77 (dt, *J* = 9.4, 2.4 Hz, 2H), 6.90 (dt, *J* = 9.4, 2.4 Hz, 2H), 7.03 (d, *J* = 8.6 Hz, 2H), 7.21–7.33 (m, 7H), 7.36 (td, *J* = 7.7, 1.1 Hz, 1H), 7.50 (dd, *J* = 7.4, 1.7 Hz, 1H), 7.52–7.58 (m, 4H), 7.86 (dd, *J* = 8.0, 1.1 Hz, 1H); ^{13}C NMR (125 MHz, CD_2Cl_2) δ 52.3, 55.6, 87.3, 89.1, 96.8, 114.0, 115.6, 123.4, 127.2, 127.4,

127.9, 128.0, 128.8, 129.2, 133.0, 134.9, 143.0, 145.3, 159.9; HRMS (APCI+) calcd for $C_{29}H_{24}O_2$ (M): 404.1776; found: 404.1762.

3-Iodo-2-(4-methoxyphenyl)-1,1-diphenyl-1*H*-indene (**13b**)

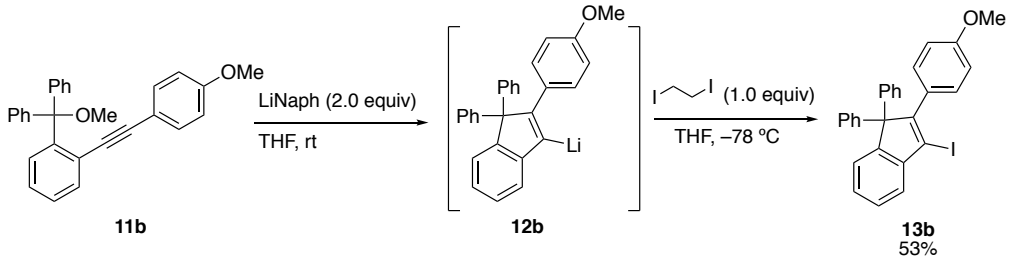

11b **12b** **13b** 53%

A mixture of granular lithium (34.6 mg, 4.99 mmol) and naphthalene (507 mg, 3.96 mmol) in THF (10 mL) was stirred at room temperature under argon atmosphere for 4 h. The LiNaph/THF was added to a solution of 1-(4-methoxyphenyl)ethynyl-2-diphenylhydroxymethylbenzene (**11b**, 800 mg, 1.98 mmol) in THF (10 mL) at room temperature, and the resulting mixture was stirred for 1 h. The resulting mixture was cooled down and added 1,2-diiodoethane (562 mg, 2.00 mmol) at room temperature. The reaction mixture was gradually warmed to ambient temperature, stirred another 1 h, and then quenched with aqueous $Na_2S_2O_3$ solution. The organic layer was extracted three times with EtOAc, dried over anhydrous Na_2SO_4, and evaporated *in vacuo*. The crude mixture was purified with column chromatography (eluent: EtOAc/hexane = 1/10) to afford compound **13b** (530 mg, 53%) as a white solid. Mp: 149–152 °C; ^{1}H NMR (500 MHz, CD_2Cl_2) δ 3.77 (s, 3H), 4.96 (s, 1H), 6.66 (dd, J = 8.0, 1.1 Hz, 1H), 6.78 (dt, J = 9.4, 2.3 Hz, 2H), 7.02 (dt, J = 9.4, 2.4 Hz, 2H), 7.15 (td, J = 7.7, 1.5 Hz, 1H), 7.24–7.35 (m, 11H), 7.57 (dd, J = 7.7, 1.4 Hz, 1H); ^{13}C NMR (125 MHz, CD_2Cl_2) δ 55.4, 71.9, 98.3, 113.3, 123.9, 124.9, 127.4, 127.5, 127.8, 128.4, 128.9, 129.3, 131.4, 141.2, 144.1, 151.8, 158.2, 159.7; HRMS (APCI+) calcd for $C_{28}H_{21}O$ (M–I): 373.1592; found: 373.1717.

7-Methoxy-10,10-diphenylindeno[2,1-*a*]inden-5(10*H*)-one (**14b**)

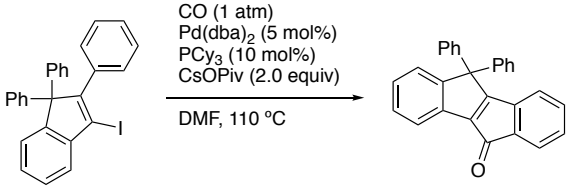

13b **14b** 63%

A solution of 3-iodo-2-(4-methoxyphenyl)-1,1-diphenyl-1*H*-indene (**13b**, 500 mg, 2.00 mmol),

$Pd(dba)_2$ (29 mg, 0.05 mmol), tricyclohexylphosphine (28 mg, 0.10 mmol) and anhydrous cesium pivalate (468 mg, 2.00 mmol) in DMF (20 mL) was stirred under CO gas atmosphere at 110 ºC for 5 h. The resulting red mixture was allowed to cooled down to ambient temperature and quenched with water. The organic layer was extracted with Et_2O, washed with brine, dried over anhydrous $MgSO_4$ and evaporated *in vacuo*. The crude mixture was purified by column chromatography (EtOAc/hexane = 1/4) and reprecipitation in CH_2Cl_2/MeOH to afford compound **14b** (251 mg, 63%) as a purplish red powder. Mp: 217–220 ºC; ^{1}H NMR (500 MHz, CD_2Cl_2) δ 3.78 (s, 3H), 6.62 (dd, *J* = 8.0, 2.9 Hz, 1H), 6.83 (d, *J* = 8.0 Hz, 1H), 7.05 (d, *J* = 2.3 Hz, 1H), 7.21 (td, *J* = 7.7, 1.1 Hz, 1H), 7.25–7.31 (m, 10H), 7.33 (t, *J* = 7.2 Hz, 1H), 7.38 (d, *J* = 7.4 Hz, 1H), 7.38 (d, *J* = 7.4 Hz, 1H), 7.66 (d, *J* = 7.4 Hz, 1H); ^{13}C NMR (125 MHz, CD_2Cl_2) δ 56.1, 65.1, 112.2, 115.1, 121.3, 122.4, 125.6, 126.7, 127.8, 128.1, 128.8, 129.0, 131.4, 135.4, 138.7, 139.2, 141.8, 155.5, 161.5, 177.3, 190.3; HRMS (APCI+) calcd for $C_{29}H_{20}O_2$ (M+H): 401.1542; found: 401.1482.

7,7'-Dimethoxy-spiro-CPV (**B**)

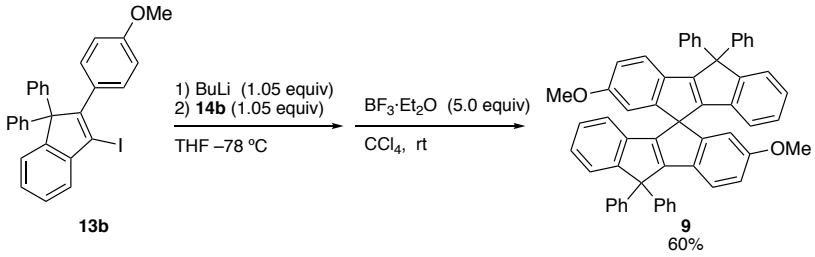

Butyllithium (0.26 mL, 1.57 M) was added into a solution of 3-iodo-2-(4-methoxyphenyl)-1,1-diphenyl-1*H*-indene (**13b**, 200 mg, 0.40 mmol) in THF (10 mL) dropwisely at –78 °C and stirred for 30 min. The resulting mixture was added ketone **14b** (168 mg, 0.42 mmol) and stirred for 1 h. The reaction mixture was allowed to warm gradually to ambient temperature and then was added water. The organic layer was extracted with dichloromethane, dried over anhydrous Na_2SO_4, and evaporated *in vacuo*. The crude mixture was dissolved in CCl_4 followed by addition of BF_3•Et_2O (282 mg, 2.0 mmol) at room temperature. After stirring for 5 min, water was added. The organic layer was extracted with chloroform, dried over anhydrous Na_2SO_4 and evaporated *in vacuo*. The crude material was purified by column chromatography (eluent: CH_2Cl_2/hexane = 1/2) to afford compound **B** (180 mg, 60%) as a white solid. Mp: 278–281 ºC; ^{1}H NMR (500 MHz, CD_2Cl_2) δ 3.60 (s, 3H), 6.20 (d, *J* = 7.4 Hz, 2H), 6.42 (d, *J* = 2.3 Hz, 2H), 6.75 (dd, *J* = 8.3, 2.6 Hz, 2H), 6.88 (t, *J* = 7.4 Hz, 2H), 7.01 (td, *J* = 7.4, 1.1 Hz, 2H), 7.23 (d, *J* = 8.6 Hz, 2H), 7.27–7.43 (m, 18H), 7.49 (dt, *J* = 6.5, 1.7 Hz,

4H); ^{13}C NMR (125 MHz, CD_2Cl_2) δ 55.6, 59.9, 64.2, 110.5, 112.6, 119.5, 121.4, 125.0, 125.7, 127.4, 127.5, 128.6, 128.7, 128.8, 128.9, 133.3, 138.2, 143.2, 143.3, 147.9, 152.1, 156.6, 159.06, 159.12; HRMS (APCI+) calcd for $C_{57}H_{40}O_2$ (M): 756.3028; found: 756.3028.

Hydrodemethylation of methoxy group

7,7'-Dihydroxy-spiro-CPV (**16**)

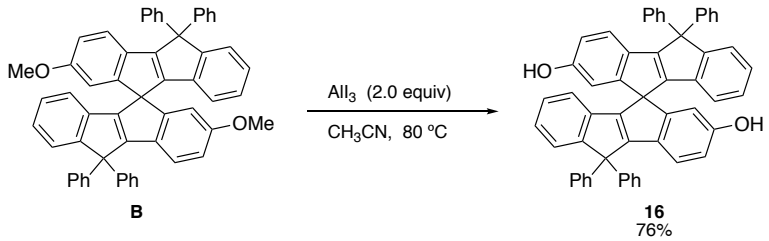

The dispersion of aluminum iodide (130 mg, 0.318 mmol) and 7,7'-dimethoxy-spiro-CPV (**B**, 120 mg, 0.159 mmol) in acetonitrile (5 mL) was stirred overnight at 80 ºC. The mixture was cooled down to room temperature and water was added. The organic layer was extracted with chloroform, dried over Na_2SO_4 and evaporated in vacuo. The crude mixture was purified by column chromatography (eluent: EtOAc/hexane = 1/3) to afford compound **16** (88.3 mg, 76%) as a white solid. The racemic compound can be separated into (*R*)- and (*S*)-**16** by chiral HPLC equipped with a DAICEL CHIRALPAK IF-3 (4.6 mm x 250 mm) column. t_R = 14.88 min for (+)-**16**, 21.30 min for (–)-**16** (flow rate: 1.0 mL/min, eluent: $CHCl_3$/Hexane = 9/1). Mp: 238–239 ºC; ^{1}H NMR (500 MHz, CD_2Cl_2) δ 4.79 (s, 2H), 6.20 (d, *J* = 7.4 Hz, 2H), 6.37 (d, *J* = 2.3 Hz, 2H), 6.68 (dd, *J* = 8.0, 2.3 Hz, 2H), 6.88 (td, *J* = 7.4, 1.1 Hz, 2H), 6.99–7.04 (m, 2H), 7.18 (d, *J* = 8.6 Hz, 2H), 7.29–7.41 (m, 20H), 7.50 (dt, *J* = 6.7, 1.6 Hz, 4H); ^{13}C NMR (125 MHz, CD_2Cl_2) δ 64.2, 111.5, 114.5, 119.5, 121.7, 125.1, 125.8, 127.4, 127.49, 127.54, 128.7, 128.8, 128.9, 133.3, 138.0, 143.0, 143.3, 147.7, 152.2, 155.0, 156.6, 159.1; HRMS (APCI+) calcd for $C_{55}H_{36}O_2$ (M): 728.2715; found: 728.2708.

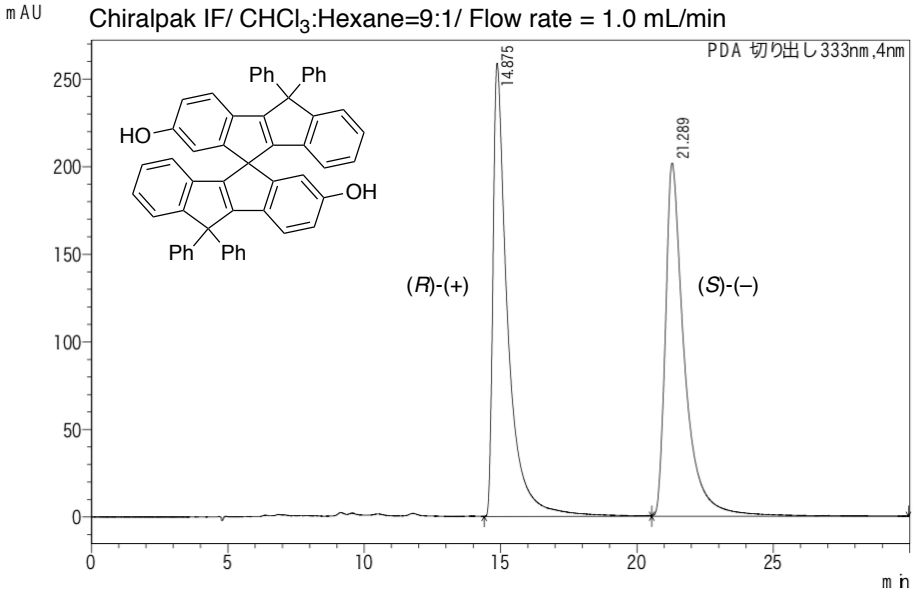

2,2'-Dibromo-7,7'-dihydroxy-spiro-CPV (**23**)

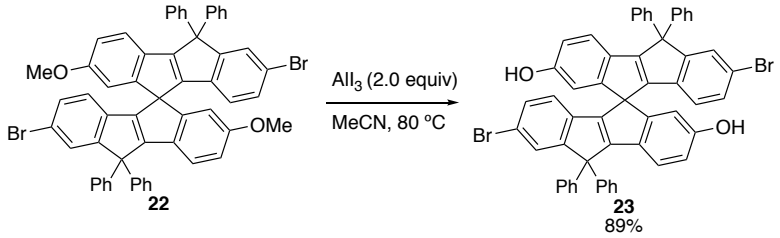

Using **22** (701 mg, 0.766 mmol) in the hydromethylation procedure afforded **23** (606 mg, 89%) as a white solid. Mp: 268–271 ºC; ^{1}H NMR (500 MHz, CD_2Cl_2) δ 4.91 (s, 2H), 5.99 (d, J = 8.0 Hz, 2H), 6.38 (d, J = 2.3 Hz, 2H), 6.69 (dd, J = 8.3, 2.6 Hz, 2H), 7.01 (dd, J = 8.0, 1.7 Hz, 2H), 7.18 (d, J = 8.0 Hz, 2H), 7.26–7.41 (m, 16H), 7.45–7.49 (m, 4H), 7.50 (d, J = 1.7 Hz, 2H); ^{13}C NMR (125 MHz, CD_2Cl_2) δ 59.6, 64.5, 111.7, 114.8, 119.6, 120.6, 122.0, 127.78, 127.82, 128.5, 128.6, 128.7, 128.9, 129.2, 130.6, 132.9, 136.9, 142.0, 142.5, 146.5, 151.8, 155.3, 158.5, 159.7; HRMS (APCI+) calcd for $C_{55}H_{34}Br_2O_2$ (M): 844.0926; found 844.0899.

Triflation of hydroxy group

Spiro-CPV-7,7'-Ditriflate (**17**)

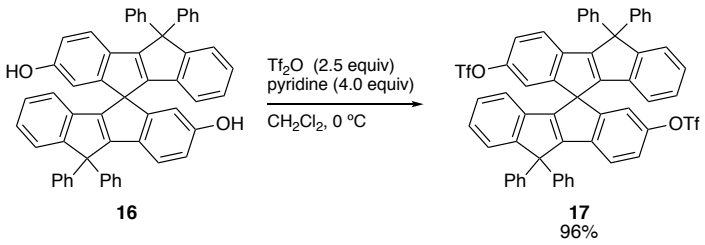

Trifluoromethanesulfonic anhydride (Tf_2O, 193 mg, 0.6.89 mmol), pyridine (87 mg, 1.098 mmol) and **16** (200 mg, 0.275 mmol) were dissolved in dichloromethane (2.0 mL) and stirred for 18 h at 0 ºC. The reaction mixture was allowed to warm gradually to ambient temperature and then was added 1M aqueous HCl solution. The organic layer was extracted with dichloromethane, dried over anhydrous Na_2SO_4, and evaporated *in vacuo*. The crude mixture was purified by column chromatography (eluent: CH_2Cl_2/hexane = 1/4) to afford compound **17** (271 mg, 96%) as a white solid. Mp: 150–152 ºC; ^{1}H NMR (500 MHz, CD_2Cl_2) δ 6.26 (d, J = 7.4 Hz, 2H), 6.71 (s, 2H), 6.94 (t, J = 8.0 Hz, 2H), 7.12 (td, J = 7.4, 1.1 Hz, 2H), 7.19 (dd, J = 8.0, 2.3 Hz, 2H), 7.33–7.46 (m, 24H); ^{13}C NMR (125 MHz, CD_2Cl_2) δ 60.1, 64.5, 116.9, 120.2, 121.8, 122.0, 125.4, 127.4, 127.9, 128.3, 128.7, 129.0, 129.2, 136.6, 140.6, 142.3, 142.4, 148.2, 150.6, 151.0, 157.1, 158.4; HRMS (APCI+) calcd for $C_{57}H_{34}F_6S_2O_6$ (M+H): 993.1779; found: 993.1779.

2,2'-Dibromo-spiro-CPV-7,7'-ditriflate (**24**)

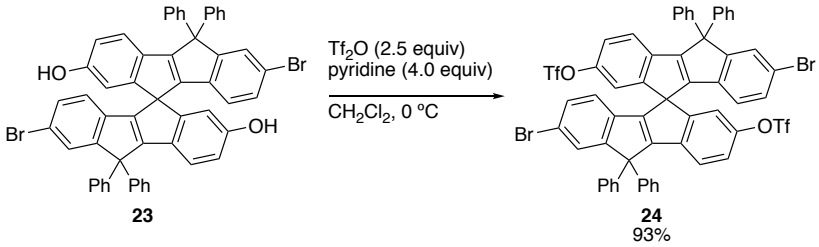

Using **23** (13 mg, 0.0147 mmol) in the triflation procedure afforded **24** (15.7 mg, 93%) as a white solid. Mp: 250–254 ºC; ^{1}H NMR (500 MHz, CD_2Cl_2) δ 6.05 (d, J = 8.0 Hz, 2H), 6.72 (d, J = 2.3 Hz, 2H), 7.07 (dd, J = 8.0, 1.7 Hz, 2H), 7.21 (dd, J = 8.6, 2.3 Hz, 2H), 7.29–7.34 (m, 4H), 7.36–7.43 (m, 18H), 7.56 (d, J = 1.7 Hz, 2H); ^{13}C NMR (125 MHz, CD_2Cl_2) δ60.0, 64.7, 117.1, 121.2, 121.4, 122.1, 122.3, 128.2, 128.3, 128.6, 128.9, 129.2, 129.4, 131.0, 135.5, 140.2, 141.3, 141.5, 148.4, 149.6, 150.2, 158.9, 159.0; HRMS (APCI+) calcd for $C_{57}H_{32}Br_2F_6S_2O_6$ (M+H): 1148.9989; found: 1149.0042.

Spiro-CPV (**A**) from **17**

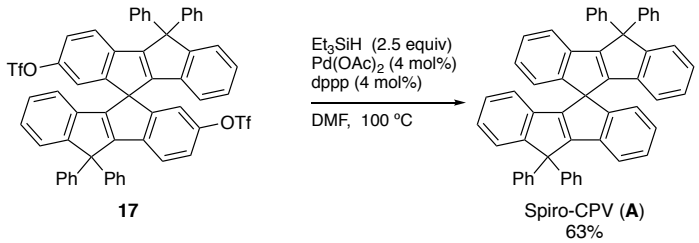

Triethylsilane (6.16 mg, 0.053 mmol), $Pd(OAc)_2$ (0.19 mg, 0.84 μmol), 1,3-bis(diphenylphosphino)propane (0.35 mg, 0.84 μmol), and **17** (21 mg, 0.021 mmol) were dissolved in DMF (1.0 mL). After stirring for 12 h at 100 ºC, the mixture was allowed to cool down to ambient temperature and water was added to the mixture. Organic layer was extracted with chloroform, dried over anhydrous Na_2SO_4, and evaporated *in vacuo*. The crude mixture was filtrated through a pad of silica-gel with chloroform and further purified by reprecipitation (CH_2Cl_2/MeOH) to afford spiro-CPV (**A**, 9.23 mg, 63%) as a white solid.

Bromination

2,2',7,7'-Tetrabromo-spiro-CPV (**19**)

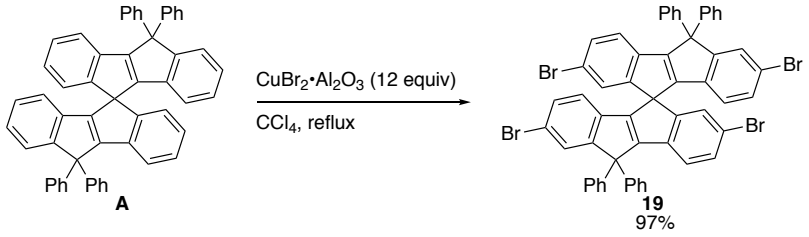

The suspension of $CuBr_2$•Al_2O_3 (69.3 g, 10.3 mmol, 33 wt%) and **A** (6.0 g, 8.62 mmol) in CCl_4 was refluxed for 15 h. The reaction mixture was cooled to ambient temperature and passed through a pad of celite with dichloromethane. After evaporation of the solvent, the residue was purified by reprecipitation (CH_2Cl_2/MeOH) to afford **19** (9.86 g, 97%) as a white solid. Mp: 361–366 ºC; ^{1}H NMR (500 MHz, CD_2Cl_2) δ 5.99 (d, J = 8.0 Hz, 2H), 6.99 (d, J = 1.7 Hz, 2H), 7.04 (dd, J = 8.0, 1.7 Hz, 2H), 7.22 (d, J = 8.0 Hz, 2H), 7.24–7.30 (m, 4H), 7.31–7.46 (m, 18H), 7.54 (d, J = 1.7 Hz, 2H); ^{13}C NMR (125 MHz, CD_2Cl_2) δ 59.8, 64.6, 120.6, 120.8, 121.2, 122.6, 126.9, 128.0, 128.1, 128.5, 128.6, 128.7, 129.0, 129.3, 130.8, 131.7, 139.0, 141.5, 141.9, 148.4, 150.3, 158.8, 159.3; HRMS (APCI+) calcd for $C_{55}H_{32}Br_4$ (M): 1007.9238; found: 1007.9243.

2,2'-Dibromo-7,7'-dimethoxy-spiro-CPV (**22**)

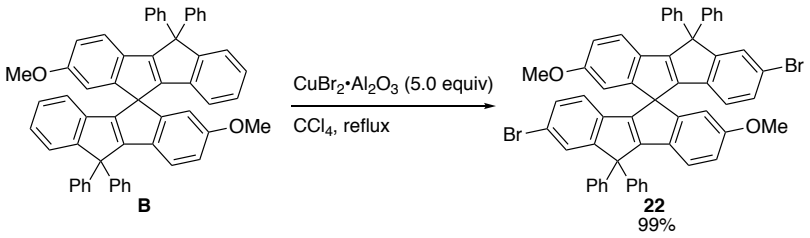

Using **B** (200 mg, 0.264 mmol) in the bromination procedure afforded **22** (241 mg, 99%) as a white solid. Mp: 306–308 ºC; ^{1}H NMR (500 MHz, CD_2Cl_2) δ 3.61 (s, 6H), 5.99 (d, *J* = 8.0 Hz, 2H), 6.42 (d, *J* = 2.3 Hz, 2H), 6.75 (dd, *J* = 8.6, 2.3 Hz, 2H), 7.00 (dd, *J* = 8.0, 1.7 Hz, 2H), 7.23 (d, *J* = 8.6 Hz, 2H), 7.28–7.40 (m, 18H), 7.46 (dt, *J* = 8.2, 1.9 Hz, 4H), 7.49 (d, *J* = 1.7 Hz, 2H); ^{13}C NMR (125 MHz, CD_2Cl_2) δ 53.9, 64.2, 110.3, 112.5, 119.2, 120.2, 121.5, 127.5, 128.1, 128.3, 128.4, 128.6, 128.8,130. 3, 132.5, 136.7, 141.9, 142.2, 146.3, 151.4, 158.2, 159.1, 159.5; HRMS (APCI+) calcd for $C_{57}H_{38}Br_2O_2$ (M+H): 913.1317; found: 913.1304.

Iodination

2,2'-7,7'-Tetraiodo-spiro-CPV (**20**)

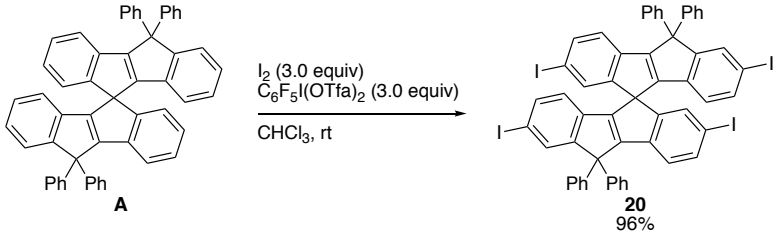

Iodine (326 mg, 1.29 mmol), [bis(trifluoroacetoxy)iodo]pentafluorobenzene (671 mg, 1.29 mmol), and **A** (300 mg, 0.430 mmol) were dissolved in chloroform (10 mL) and stirred for 18 h at ambient temperature. The reaction mixture added saturated aqueous solution of $Na_2S_2O_3$. The organic layer was extracted with chloroform, dried over anhydrous Na_2SO_4, and evaporated *in vacuo*. The crude mixture was purified by reprecipitation (CH_2Cl_2/MeOH) to afford compound **20** (494 mg, 96%) as a white solid. Mp: 322–324 ºC; ^{1}H NMR (500 MHz, CD_2Cl_2) δ 5.87 (d, *J* = 8.0 Hz, 2H), 7.09 (d, *J* = 8.0 Hz, 2H), 7.15 (d, *J* = 1.1 Hz, 2H), 7.21–7.29 (m, 6H), 7.31–7.46 (m, 16H), 7.59 (dd, *J* = 8.0, 1.7 Hz, 2H), 7.73 (d, *J* = 1.7 Hz, 2H); ^{13}C NMR (125 MHz, CD_2Cl_2) δ 64.5, 77.9, 91.8, 92.1, 121.6, 123.0, 127.99, 128.02, 128.5, 128.6, 129.0, 129.3, 132.5, 134.3, 136.5, 136.9, 137.7, 139.4, 141.4, 141.9, 148.3, 150.4, 158.9, 159.3, ;

HRMS (APCI+) calcd for $C_{55}H_{32}I_4$ (M): 1199.8683; found: 1199.8740.

Borylation

2,2',7,7'-Tetrakis(4,4,5,5-tetramethyl-1,3,2-dioxaboran-2-yl)-spiro-CPV (**21**)

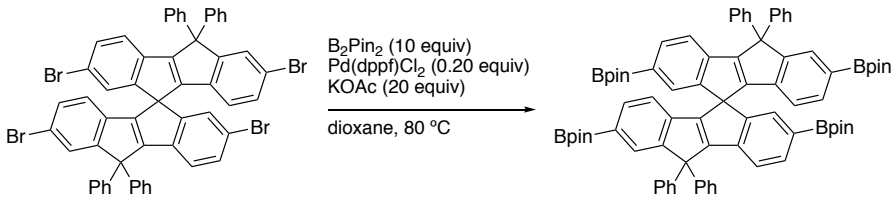

19 **21** 52%

Bis(pinacolato)diborone (1.01 g, 4.0 mmol), $Pd(dppf)Cl_2$ (65.3 mg, 0.080 mmol), potassium acetate (785 mg, 8.0 mmol), and **19** (400 mg, 0.40 mmol) was dissolved in dioxane (16 mL) and heated to 80 ºC. After stirring for 22 h, the reaction mixture was cooled to ambient temperature and added water. The organic layer was extracted with chloroform, dried over anhydrous Na_2SO_4, and evaporated *in vacuo*. The crude mixture was purified by column chromatography (eluent: EtOAc/hexane = 1/1) to afford **21** (251 mg, 52%) as a white solid. Mp: 332–335 ºC; ^{1}H NMR (500 MHz, CD_2Cl_2) δ 1.19 (s, 24H), 1.23 (s, 24H), 6.22 (d, J = 8.0 Hz, 2H), 7.16 (s, 2H), 7.30 (d, J = 7.4 Hz, 2H), 7.31–7.40 (m, 18H), 7.53 (dt, J = 6.9, 1.6 Hz, 4H), 7.65 (dd, J = 7.4, 1.1 Hz, 2H), 7.74 (s, 2H); ^{13}C NMR (125 MHz, CD_2Cl_2) δ 24.9, 25.0, 64.3, 84.0, 119.6, 121.0, 127.57, 127.61, 128.7, 128.8, 128.9, 129.0, 130.6, 134.5, 134.9, 140.5, 142.5, 142.6, 143.1, 148.8, 150.9, 156.6, 161.3; HRMS (APCI+) calcd for $C_{79}H_{80}B_4O_8$ (M+H): 1201.6344; found: 1201.6314.

Rearrangement of ketone **14a**

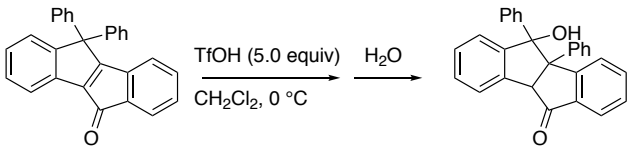

14a **18** 86%

The ketone **14a** (111 mg, 0.30 mmol) was dissolved in dichloromethane followed by addition of TfOH (225 mg, 1.5 mmol) at 0 °C. After stirring for 3 h, water was added. The organic layer was extracted with dichloromethane, dried over anhydrous $MgSO_4$ and evaporated *in vacuo*. The crude material was purified by column chromatography (eluent: CH_2Cl_2/hexane = 1/1) to afford compound **18** (100 mg, 86%) as a white solid. Mp: 232–233 °C; ^{1}H NMR (500 MHz, $CDCl_3$) δ 2.81 (s, 1H), 4.94 (s, 1H), 6.93

(tt, J = 7.4, 1.5 Hz, 1H), 6.96–7.03 (m, 3H), 7.06 (t, J = 7.7 Hz, 2H), 7.12–7.21 (m, 3H), 7.23 (t, J = 7.4 Hz, 1H), 7.27–7.37 (m, 4H), 7.54–7.61 (m, 1H), 7.66 (t, J = 7.2 Hz, 2H), 8.14 (d, J = 8.0 Hz, 1H); ^{13}C NMR (125 MHz, $CDCl_3$) δ 63.0, 67.4, 88.6, 124.6, 124.66, 126.68, 125.9, 126.0, 126.5, 127.3, 127.5, 127.9, 128.4, 129.0, 129.3, 129.6, 134.0, 134.8, 136.9, 142.4, 144.3, 148.2, 156.8, 203.8; HRMS (APCI–) calcd for $C_{28}H_{20}O_2$ (M–H): 387.1391; found: 387.1381.

3.7.2. Characterization

Crystallographic study

The diffraction images for X-ray crystallographic analysis were collected on a Rigaku Rapid II diffractometer equipped with an imaging plate using Cu Kα (λ = 1.5419 Å) radiation. The positional and thermal parameters were refined by the full-matrix least-squares method using SHELXL-2014/7 program.[40] The Yadokari-XG software was used for refinement of the structure.[41]

CCDC 1951838 contains the supplementary crystallographic data for this paper.

Table 3.3. Crystallographic data for Spiro-CPV (**A**) (CCDC 1951838)

Formula	$C_{57}H_{40}Cl_4$
Formula weight	866.69
Measurement temperature	123(2) K
Crystal system	monoclinic
Space group	C 2/c
Lattice parameters	a = 11.9001(3) Å
	b = 15.8666(4) Å
	c = 22.74.72(5) Å
	α = 90°
	β = 102.900(7)°
	γ = 90°
Volume	4186.6(2)
Z value	4
Density (calculated)	1.375 g/cm^3
F(000)	1800.0
Number of reflections measured	23863
Number of unique reflections	3828
R_{int}	0.0442
Number of observed reflections ($I > 2\sigma(I)$)	3230
Goodness of fit indicator	1.040

Final R_1 indices [$I > 2\sigma(I)$] (R_{obs}, wR_{obs})	0.0360, 0.0867
R indices [all data] (R_{all}, wR_{all})	0.0457, 0.0907
Largest diff. peak and hole	0.332/−0.393 e·Å^{-3}

Computational study

The Density Functional Theory (DFT) calculation for compound **A** was conducted at the B3LYP/6-31G (d,p) level on Gaussian09 packages.[42]

Table 3.4. Theoretically optimized coordinates of **A** calculated at the B3LYP/6-31G(d,p) level of theory.

Total energy: E(RB3LYP/6-31G(d,p)) = –2117.58545606 Hartree

Center Number	Atomic Number	Atomic Type	Coordinates (Angstroms) X	Y	Z
1	6	0	1.938326	2.93705	2.045285
2	1	0	1.941171	4.006761	1.867669
3	6	0	2.824541	2.370433	2.966903
4	1	0	3.516884	3.01102	3.505516
5	6	0	2.832485	0.993407	3.201304
6	1	0	3.529944	0.572016	3.919133
7	6	0	1.947582	0.148506	2.516523
8	6	0	1.053854	2.101203	1.359668
9	6	0	1.066933	0.705374	1.603626
10	1	0	1.954364	-0.922653	2.69719
11	6	0	0.042972	2.348225	0.334819
12	6	0	-0.533252	1.180376	-0.045741
13	6	0	-0.588351	3.550087	-0.367332
14	6	0	-1.593671	2.812607	-1.288747
15	6	0	-1.540717	1.414374	-1.06729
16	6	0	-2.465629	3.33481	-2.232397
17	6	0	-3.292444	2.462607	-2.954982
18	6	0	-3.239147	1.084149	-2.735349
19	6	0	-2.361727	0.547004	-1.789675

20	1	0	-2.311103	-0.52458	-1.627098
21	1	0	-3.882869	0.422554	-3.307668
22	1	0	-3.977347	2.864923	-3.695492
23	1	0	-2.510911	4.402964	-2.419658
24	6	0	0.389219	4.369146	-1.227982
25	6	0	1.655911	3.878236	-1.567173
26	6	0	0	5.612922	-1.75138
27	6	0	2.505683	4.601705	-2.406921
28	1	0	1.987907	2.927427	-1.165177
29	6	0	0.845143	6.334695	-2.592188
30	1	0	-0.966422	6.028339	-1.484177
31	6	0	2.103822	5.831075	-2.92591
32	1	0	3.484965	4.20008	-2.651305
33	1	0	0.520462	7.294782	-2.983276
34	1	0	2.764669	6.394404	-3.5781
35	6	0	-1.294348	4.405633	0.714523
36	6	0	-2.589275	4.090187	1.150531
37	6	0	-0.620278	5.456968	1.35232
38	6	0	-3.192247	4.806569	2.184611
39	1	0	-3.13316	3.280965	0.675715
40	6	0	-1.223249	6.175164	2.38582
41	1	0	0.37904	5.729043	1.029618
42	6	0	-2.513082	5.854173	2.807286
43	1	0	-4.198692	4.545435	2.499376
44	1	0	-0.680369	6.988119	2.859717
45	1	0	-2.98409	6.414698	3.609417
46	6	0	0	0	0.742559
47	6	0	-1.066933	-0.705374	1.603626
48	6	0	0.533252	-1.180376	-0.045741
49	6	0	-1.053854	-2.101203	1.359668

50	6	0	-0.042972	-2.348225	0.334819
51	6	0	1.540717	-1.414374	-1.06729
52	6	0	0.588351	-3.550087	-0.367332
53	6	0	1.593671	-2.812607	-1.288747
54	6	0	1.294348	-4.405633	0.714523
55	6	0	0.620278	-5.456968	1.35232
56	6	0	2.589275	-4.090187	1.150531
57	6	0	1.223249	-6.175164	2.38582
58	1	0	-0.37904	-5.729043	1.029618
59	6	0	3.192247	-4.806569	2.184611
60	1	0	3.13316	-3.280965	0.675715
61	6	0	2.513082	-5.854173	2.807286
62	1	0	0.680369	-6.988119	2.859717
63	1	0	4.198692	-4.545435	2.499376
64	1	0	2.98409	-6.414698	3.609417
65	6	0	-0.389219	-4.369146	-1.227982
66	6	0	-1.655911	-3.878236	-1.567173
67	6	0	0	-5.612922	-1.75138
68	6	0	-2.505683	-4.601705	-2.406921
69	1	0	-1.987907	-2.927427	-1.165177
70	6	0	-0.845143	-6.334695	-2.592188
71	1	0	0.966422	-6.028339	-1.484177
72	6	0	-2.103822	-5.831075	-2.92591
73	1	0	-3.484965	-4.20008	-2.651305
74	1	0	-0.520462	-7.294782	-2.983276
75	1	0	-2.764669	-6.394404	-3.5781
76	6	0	-1.938326	-2.93705	2.045285
77	6	0	-1.947582	-0.148506	2.516523
78	6	0	-2.832485	-0.993407	3.201304
79	1	0	-3.529944	-0.572016	3.919133

80	6	0	-2.824541	-2.370433	2.966903
81	1	0	-3.516884	-3.01102	3.505516
82	1	0	-1.954364	0.922653	2.69719
83	1	0	-1.941171	-4.006761	1.867669
84	6	0	2.465629	-3.33481	-2.232397
85	6	0	2.361727	-0.547004	-1.789675
86	6	0	3.239147	-1.084149	-2.735349
87	1	0	3.882869	-0.422554	-3.307668
88	6	0	3.292444	-2.462607	-2.954982
89	1	0	3.977347	-2.864923	-3.695492
90	1	0	2.311103	0.52458	-1.627098
91	1	0	2.510911	-4.402964	-2.419658

Photophysical properties

UV-Vis absorption spectra were measured with a JASCO V-670 spectrometer. Fluorescence spectra were measured with a HITACHI F-4500 spectrometer. Photoluminescence quantum yields were measured on Hamamatsu Photonics C9920–02 Absolute PL Quantum Yield Measurement System, and absolute quantum yields were determined by using a calibrated integrating sphere system. Fluorescence lifetimes were measured on Hamamatsu Photonics C11367-02 Quantaurus-Tau. CD spectra were measured on a JASCO J-1500 spectropolarimeter. CPL spectra were measured on a JASCO CPL-200 spectrometer. Optical rotations were measured on a JASCO P-1030 polarimeter using a 50-mm cell. The absorption maximum wavelengths were used as excitation wavelengths. Spectral grade solvent (dichloromethane) was used as a solvent for UV-Vis absorption fluorescence, CD, CPL, and optical rotation measurements.

Electrochemical properties

CV and DPV were conducted with HOKUTO DENKO HZ-7000 voltammetric analyzer. Measurements were carried out in a one-compartment cell under argon gas, equipped with a platinum counter electrode, a glassy-carbon working electrode, and an Ag/Ag^+ reference electrode. The supporting electrolyte was a 0.5 M dichloromethane solution of tetrabutylammonium

hexafluorophosphate. All potentials were collected against Fc/Fc^+.

Ionization potential

PYS measurement was performed with PYS-201 (Sumitomo Heavy Industries, Ltd).

Thermal stabilities

TGA was performed on a Rigaku ThermoPlus 2 thermal analyzer (TG 8120). Sample was placed in an aluminum pan and heated to 500 ºC at the rate of 10 K/min under N_2 purge at a flow rate of 10 mL/min. Al_2O_3 was used as reference material. DSC was performed on a SII Nanotechnology (DSC6220) instrument. Samples were placed in aluminum pans and heated at 10 K/min, under N_2 gas at a flow rate of 50 mL/min.

3.8. References

[1] (a) Hoffmann, R.; Imamura, A.; Zeiss, G. D. *J. Am. Chem. Soc.* **1967**, 89, 5215–5220. (b) Simmons, H. E.; Fukunaga, T. *J. Am. Chem. Soc.* **1967**, *89*, 5208–5215. (c) Schweig, A.; Weidner, U.; Hellwinkel, D.; Krapp, W. *Angew. Chem. Int. Ed.* **1973**, *89*, 310–311.

[2] Clarkson, R. G.; Gomberg, M. *J. Am. Chem. Soc.* **1930**, *52*, 2881–2891.

[3] Saragi, T. P. I.; Spehr, T.; Siebert, A.; Fuhrmann-Lieker, T.; Salbeck, J. *Chem. Rev.* **2007**, *107*, 1011–1055.

[4] (a) Bach, U.; Lupo, D.; Comte, P.; Moser, J. E.; Weissörtel, F.; Salbeck, J.; Spereitzer, H.; Grätzel, M. *Nature* **1998**, *395*, 583–585. (b) Hawash, Z.; Ono, L. K.; Qi, Y. *Adv. Mater. Interfaces,* **2018**, *5*,1700623. (c) Jeon, N. J.; Lee, H. G.; Kim, Y. C.; Seo, J.; Noh, J. H.; Lee, J.; Seok, S. I. *J. Am. Chem. Soc.* **2014**, *136*, 7837–7840. (d) Gao, G.; Liang, N.; Geng, H.; Jiang, W.; Fu, H.; Feng, J.; Hou, J.; Feng, X.; Wang, Z. *J. Am. Chem. Soc.* **2017**, *139*, 15914–15920. (e) Urieta-Mora, J.; Garcia-Benito, I.; Molina-Ontoria, A.; Martín N. *Chem. Soc. Rev.* **2018**, *47*, 8541–8571.

[5] Sowa, J. K.; Mol, J. A.; Briggs, G. A. D.; Gauger, E. M. *J, Phys. Chem. Lett.* **2018**, *9*, 1859–1865.

[6] (a) Sandoval-Salinas, M. E.; Carreras, A.; Casado, J.; Casanova, D. *J. Chem. Phys.* **2019**, *150*, 204306. (b) Kumarasamy, E.; Sanders, S. N.; Tayebjee, M. J. Y.; Asadpoordarvish, A.; Hele, T. J. H.; Fuemmeler, E.G.; Pun, A. B.; Yablon, L. M.; Low, J. Z.; Paley, D. W.; Dean, J. C.; Choi, B.; Scholes, G. D.; Steigerwald, M. L.; Ananth, N.; McCamey, D. R.; Sfeir, M. Y.; Campos, L. M. *J. Am. Chem. Soc.* **2017**, *139*, 12488–12494.

[7] (a) Yang, Z.; Mao, Z.; Xie, Z.; Zhang, Y.; Liu, S.; Zhao, J.; Xu, J.; Chi, Z.; Aldred, M. P. *Chem. Soc. Rev.* **2017**, *46,* 915–1016. (b) Tao, Y.; Yuan, K.; Chen, T.; Xu, P.; Li, H.; Chen, R.; Zheng, C.; Zhang, L.; Huang, W. *Adv. Mater.* **2014**, *26*, 7931–7958. (c) Im, Y.; Kim, M.; Cho, Y. J.; Seo, J.-A. ; Yook, K. S.; Lee, J. Y. *Chem. Mater.* **2017**, *29*, 1946–1963.

[8] Mei, J.; Leung, N. L. C.; Kwok, R. T. K.; Lam, J. W. Y.; Tang, B. Z. *Chem. Rev.* **2015**, *115*, 11718–11940.

[9] Yuan, L.; Lin, W.; Zheng, K.; Zhu, S. *Acc. Chem. Res.* **2013**, *46*, 1426–1473.

[10] Xie, J.-H.; Zhou, Q. L. *Acc. Chem. Res.* **2008**, *41*, 581–593.

[11] von Baeyer, A. P. *Ber. Dtsch. Chem. Ger.* **1900**, *33*, 3771–3775.

[12] Srivastava, N.; Mital, A.; Kumar, A. *Chem. Commun.* **1992**, 493–494.

[13] Alcazar, V.; Diederich, F. *Angew. Chem., Int. Ed. Engl.* **1992**, *31*, 1521−1523.

[14] (a) Prelog, V.; Bedekovic, D. *Helv. Chim. Acta* **1979**, *62*, 2285–2303. (b) Harada, N.; Ono, H.; Nishiwaki, T.; Uda, H. *J. Chem. Soc., Chem. Commun.* **1991**, 1753−1755.

[15] Haas, G.; Prelog, V. *Helv. Chim. Acta.* **1969**, *52*, 1202−1218.

[16] Haas, G.; Hulbert, P. B.; Klyne, W.; Prelog, V.; Snatzke, G. *Helv. Chim. Acta,* **1971**, *54*, 491–509.

[17] Schadt, M. *Annu. Rev. Mater. Sci.* **1997**, *27*, 305–379. (b) Peeters, E; Christiaans, M. P. T.; Janssen, R. A. J.; Schoo, H. F. M.; Dekkers, H. P. J. M.; Jeijer, E. W. *J. Am. Chem. Soc.* **1997**, *119*, 9909– 9910. (c) Grell, M.; Oda, M.; Whitehead, K. S.; Asimakis, A.; Neher, D.; Bradley, D. D. C. *Adv. Mater.* **2001**, *13*, 577–580.

[18] (a) Chen, F.; Gindre, D.; Nunzi, J. M. *Opt. Express*, **2008**, *16*, 16746–16753. (b) Furumi, S. *Chem. Rec*. **2010**, *10*, 394–408. (c) Cerdán, L.; Moreno, F.; Johnson, M.; Muller, G.; Moya, S. D. L.; Garcia-Moreno, I. *Phys. Chem. Chem. Phys*. **2017**, *19*, 22088–22093.

[19] (a) Carr, R.; Evans, N. H.; Parker, D. *Chem. Soc. Rev.* **2012**, *41*, 7673–7686. (b) Heffern, M. C.; Matosziuk, L. M.; Meade, T. J. *Chem. Rev.* **2014**, *114*, 4496–4539.

[20] (a) Murai, M.; Takeuchi, Y.; Yamauchi, K.; Kuninobu, Y.; Takai, K. *Chem. – Eur. J.* **2016**, *22*, 6048–6058. (b) Shintani, R.; Misawa, N.; Takano, R.; Nozaki, K.; *Chem. – Eur. J.* **2017**, *23*, 2660–2665.

[21] (a) Takase, K.; Noguchi, K.; Nakano, K. *Org. Lett*. **2017**, *19*, 5082–5085. (b) Takase, K.; Noguchi, K.; Nakano, K. *J. Org. Chem*. **2018**, *83*, 15057–15065. (c) Takase, K.; Noguchi, K.; Nakano, K. *Bull. Chem. Soc. Jpn.* **2019**, *92*, 1008–1017.

[22] (a) Anthony, J. E. *Angew. Chem. Int. Ed.* **2008**, *47*, 452–485. (b) Mazzio, K. A.; Luscombe, C. K. *Chem. Soc. Rev.* **2015**, *44*, 78.

[23] (a) Kraft, A.; Grimsdale, A. C.; Holmes, A. B. *Angew. Chem. Int. Ed.* **1998**, *37*, 402–428. (b) Samuel, I. D.; Turnbull, G. A. *Chem. Rev.* **2007**, *107*, 1272–1295.

[24] (a) Shirakawa, H.; Louis, E. J.; MacDiarmid, A. G.; Chiang, C. K.; Heeger, A. J. *J. Chem. Soc., Chem. Commun.* **1977**, **16**, 578−580. (b) Burroughes, J. H.; Bradley, D. D. C.; Brown, A. R.; Marks, R. N.; Mackay, K.; Friend, R. H.; Burns, P. L.; Holmes, A. B. *Nature* **1990**, *347*, 539–541.

[25] Berresheim, A. J.; Müller, M.; Müllen, K. *Chem. Rev.* **1999**, *99*, 1747–1785.

[26] (a) Scherf, U. *J. Mater. Chem.* **1999**, *9*, 1853–1864. (b) Grimsdale, A. C.; Müllen, K. *Macromol. Rapid Commun.* **2007**, *28*, 1676–1702. (c) Fukazawa, A.; Yamaguchi, S. *Chem. Asian J.* **2009**, *4*, 1386–1400. (d) Wu, J.-S.; Cheng, S.-W.; Cheng, Y.-J.; Hsu, C.-S. *Chem. Soc. Rev.* **2015**, *44*, 1113–1154.

[27] (a) Zhu, X.; Mitsui, C.; Tsuji, H.; Nakamura, E. *J. Am. Chem. Soc*. **2009**, *131*, 13596–13597. (b) Zhu,

X.; Tsuji, H.; Navarrete, J. T. L.; Casado, J.; Nakamura, E. *J. Am. Chem. Soc*. **2012**, *134*, 19254–19259. (c) Tsuji, H.; Nakamura, E. *Acc. Chem. Res.* **2019**. *52*, 2939–2949.

[28] Yan, Q.; Guo, Y.; Ichimura, A.; Tsuji, H.; Nakamura, E. *J*. *Am*. *Chem*. *Soc*. **2016**, *138*, 10897–10904.

[29] Morales-Vidal, M.; Boj, P. G.; Villalvilla, J. M.; Quintana, J. A.; Yan, Q.; Lin, N.-T.; Zhu, X.; Ruangsupapichat, N.; Casado, J.; Tsuji, H.; Nakamura, E.; Díaz-García, M. A. *Nat. Commun.* **2015**, *6*, 8458.

[30] Yan, Q. Unpublished data.

[31] (a) Campo, M. A.; Larock, R. C. *Org. Lett*. **2000**, *2*, 3675–3677. (b) Campo, M. A.; Larock, R. C. *J. Org. Chem*. **2002**, *67*, 5616–5620.

[32] Kotsuki, H.; Datta, P. K.; Hayakawa, H.; Suenaga, H. *Synthesis* **1995**, *11*, 1348–1350.

[33] Kodomari, M.; Satoh, H.; Yoshitomi, S. *J. Org. Chem.* **1988**, *53*, 2093–2094.

[34] Kotagiri, R.; Adepu, R. *Eur. J. Org. Chem*. **2018**, *33*, 4556–4564.

[35] Ishiyama, T.; Miyaura, N. *Chem. Rec*. **2004**, *3*, 271–280.

[36] Espino, G.; Kurbangalieva, A.; Brown, J. M. *Chem. Commun*. **2007**, *17*, 1742–1744.

[37] (a) Sánchez-Carnerero, E. M.; Agarrabeitia, A. R.; Moreno, F.; Maroto, B. L.; Muller, G.; Ortiz, M. J.; Moya, S. *Chem. Eur. J.* **2015**, *21*, 13488–13500. (b) Tanaka, H.; Inoue, Y.; Mori, T. *ChemPhotoChem* **2018**, *2,* 386–402.

[38] Schweig, A.; Weidner, U.; Hellwinkel, D.; Krapp, W. *Angew. Chem. Int. Ed. Engl*. **1973**, *12*, 310–311.

[39] Still, W. C.; Kahn, M.; Mitra, A. *J. Org. Chem. 1978,* **43**, 2923–2925.

[40] Sheldrick, G. M. *Acta Crystallogr A Found Adv.* **2015**, *71*, 3–8.

[41] Kabuto, C.; Akine, S.; Nemoto, T.; Kwon, E. *J. Cryst. Soc. Jpn.*, **2009**, *51*, 218-224.

[42] Gaussian 09, Revision B.01, Frisch, M. J.; Trucks, G. W.; Schlegel, H. B.; G. E. Scuseria, ; Robb, M. A.; Cheeseman, J. R.; Scalmani, G.; Barone, V.; Mennucci, B.; Petersson, G. A.; Nakatsuji, H.; Caricato, M.; Li, X.; Hratchian, H. P.; Izmaylov, A. F.; Bloino, J.; Zheng, G.; Sonnenberg, J. L.; Hada, M.; Ehara, M.; Toyota, K.; Fukuda, R.; Hasegawa, J.; Ishida, M.; Nakajima, T.; Honda, Y.; Kitao, O.; Nakai, H.; Vreven, T.; Montgomery Jr. J. A.; , Peralta, J. E.; Ogliaro, F.; Bearpark, M.; Heyd, J. J.; Brothers, E.; Kudin, K. N.; Staroverov, V. N.; Keith, T.; Kobayashi, R.; Normand, J.; Raghavachari, K.; Rendell, A.; Burant, J. C.; Iyengar, S. S.; Tomasi, J.; Cossi, M.; Rega, N.; Millam, J. M.; Klene, M.; Knox, J. E.; Cross, J. B.; Bakken, V.; Adamo, C.; Jaramillo, J.; Gomperts, R.; Stratmann, R. E.; Yazyev, O.; Austin,

A. J.; Cammi, R.; Pomelli, C.; Ochterski, J. W.; Martin, R. L.; Morokuma, K.; Zakrzewski, V. G.; Voth, G. A.; Salvador, P.; Dan nenberg, J. J.; Dapprich, S.; Daniels, A. D.; Farkas, O.; Foresman, J. B.; Ortiz, J. V.; Cioslowski, J.; Fox, D. J. Gaussian, Inc., Wallingford CT, 2010.

Chapter 4.

Intensification of Circularly Polarized Luminescence by Elongation of π-systems of Spiro-CPV

4.1. Introduction

4.1.1. Photoluminescence quantum yield and radiative rate constant

The efficiency of photoluminescence is generally evaluated by photoluminescence quantum yield (Φ) and the rate of radiative decay (k_r). These two values of luminescent materials are quite important when we think about their use in light-emitting device and laser applications.[1] A molecule in excited state, formed by photon absorption of its ground state, undergoes two deactivation pathways: radiative decay and nonradiative decay. The Φ is described as the ratio of molecules undergoing radiative decay, or the possibility of radiative decay, as following:

$$\Phi = \frac{m}{n} = \frac{k_r}{k_r + k_{nr}} \quad (4.1)$$

Where n is the number of absorbed photons, m is the number of photons radiated from molecules, and k_{nr} is nonradiative decay rate constant. From this equation, it is found that the enhancement of radiative decay, as well as the inhibition of nonradiative decay such as thermal deactivation and charge transfer, is important for intense photoluminescence.

Since Einstein achieved the derivation of the fundamental theory on the transition probabilities upon photoexcitation and emission in 1917,[2] researchers[3] developed the following equation to describe the absorption and emission system in solution.

$$k_r = A_{u\to l} = 8\times 2303\ \pi c\ N_A\ \bar{\nu}^2\ n^2\ \frac{g_l}{g_u}\int \varepsilon \mathrm{d}\,\bar{\nu} \quad (4.2)$$

Where, $A_{u\to l}$ is the Einstein transition probability coefficient for emission upon transition from the upper u state to the lower l state, c is the speed of light in vacuum, N_A is Avogadro constant, $\bar{\nu}$ is the frequency of the transition, n is the refractive index of solvent, g_l and g_u are the degeneracies for the u and l states, ε is the molar extinction coefficient. The relationship, however, was capable only for atomic transitions, and could not be applied for molecules due to large inaccuracy. In 1962, Strickler and Berg derived a modified relationship equation 4.3[4] that shows good agreements with the experimental results.

$$k_r = A_{u\to l} = 2.880\times 10^{-9} < \bar{\nu}^{-3} >^{-1}\ n^2\ \frac{g_l}{g_u}\int \varepsilon \mathrm{d}\ln\bar{\nu} \quad (4.3)$$

In this equation, $<\bar{\nu}^{-3}>^{-1}$ is the reciprocal of the reciprocal of the average of $\bar{\nu}^{-3}$. For oligo(*p*-phenylenevinylene) systems, Peeters *et al*. reported the increased extinction coefficient and k_r in longer conjugation length to be consistent with this relationship.[5] These equations 4.2–4.3, where k_r

is proportional to the integration of extinction coefficient over the absorption band, inspired me the idea that the strong absorption in the rigid carbocyclic system could enhance radiative decay, resulting in increase of k_r and Φ.

Recently, Maeda *et al.* proposed that the high energetic barrier to reach minimum energy conical intersections (MECI), which cause S_1–S_0 transition, is important to inhibit nonradiative decay of the excited state (Figure 4.1).[6,7] In these studies, it is suggested that the Frank-Condon state get stabilization in larger polyaromatic hydrocarbons because of the delocalization of π and π* orbitals, while the MECI does not differ so much. Therefore, the energy barrier between the Frank-Condon state and MECI increase in lager π-conjugation system to arrow high fluorescence quantum yield.

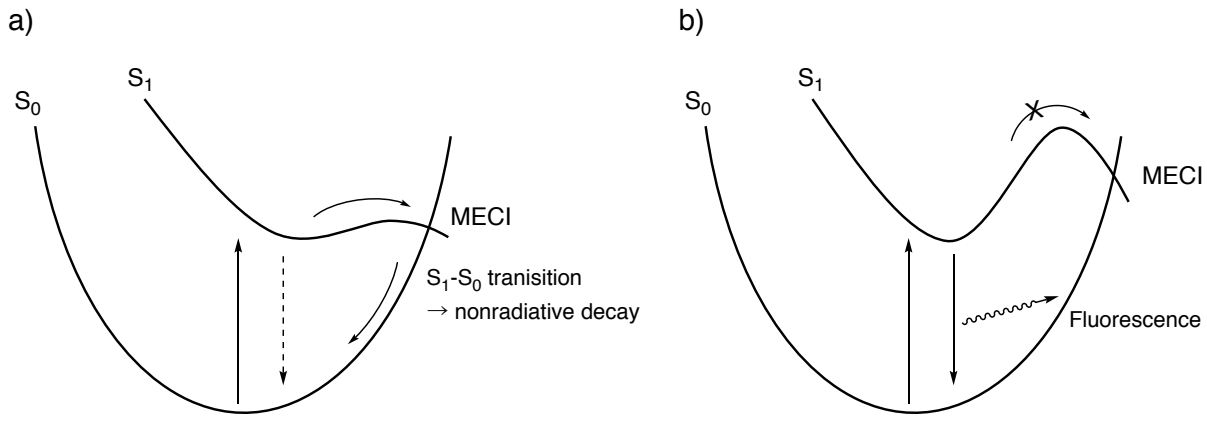

Figure 4.1. Schematic image for the energy surfaces and S_1-S_0 transition. a) Nonradiative decay via S_1-S_0 transition because of small energy barrier. b) High energy barrier to exhibit strong fluorescence.

4.1.2. Intensification of fluorescence by elongation of π-system: Chapter outline

In Chapter 3, it is suggested that spiro-CPV undergoes small reorganization upon photoexcitation thanks to its structural rigidity to show high Φ_{FL} of 0.74 and k_r of 1.30×10^{-8} s^{-1} as well as high stabilities. However, these values might actually be not high enough for some applications: organic semiconducting lasers, for example, require larger k_r than ~4×10^8 s^{-1} for amplified spontaneous emission (ASE).[8]

Based on these ideas, I envisioned that it is possible to increase the Φ_{FL} and k_r of CPL emission of spiro-CPV by the π-elongation of each COPV units that enhance absorption intensity. In this chapter, the effect of π-expansion of spiro-CPV is reported (Figure 4.2). Phenyl and phenylethynyl

groups were attached on 2 positions of each COPV units to expand conjugation systems straightforwardly. These substituents are selected due to their easiness of introduction and structural rigidity. Phenylethynyl group is also expected to enhance radiative decay, as seen in previous studies.[9] In section 4.2, the synthesis of the diphenyl and bis(phenylethynyl) derivatives is described. Section 4.3 describes computational study on the electron transition of spiro-CPVs. The π-elongation decreased HOMO-LUMO gap and increased oscillator strength for HOMO–LUMO excitation. In section 4.4, their photophysical and chiroptical properties are described. The absorption intensity and radiative decay rate were successfully enhanced by π-expansion, resulting in high fluorescence quantum yields. Especially, the bis(phenylethynyl) derivative achieved Φ_{FL} = 0.99, the highest value for organic CPL molecules. Section 4.5 summarizes the investigations in this chapter.

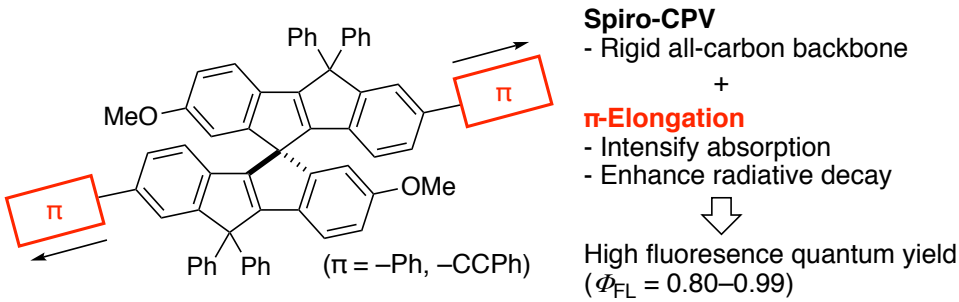

Figure 4.2. π-Elongation of spiro-CPV for photoluminescence intensification.

4.2. Synthesis

The π-elongation of spiro-CPV was conducted from compound **22** (Scheme 4.1). The diphenyl compound **C** was successfully synthesized via Suzuki-Miyaura coupling[10] with phenyl boronic acid in 51%. The bis(phenylethynyl) compound **D** was obtained via Sonogashira coupling[11] with ethynylbenzene in 59%. The enantiomers of them, obtained by using chiral **22** as a starting material, were used for the further investigation on photophysical properties.

Scheme 4.1. Elongation of π-conjugation of **22**.

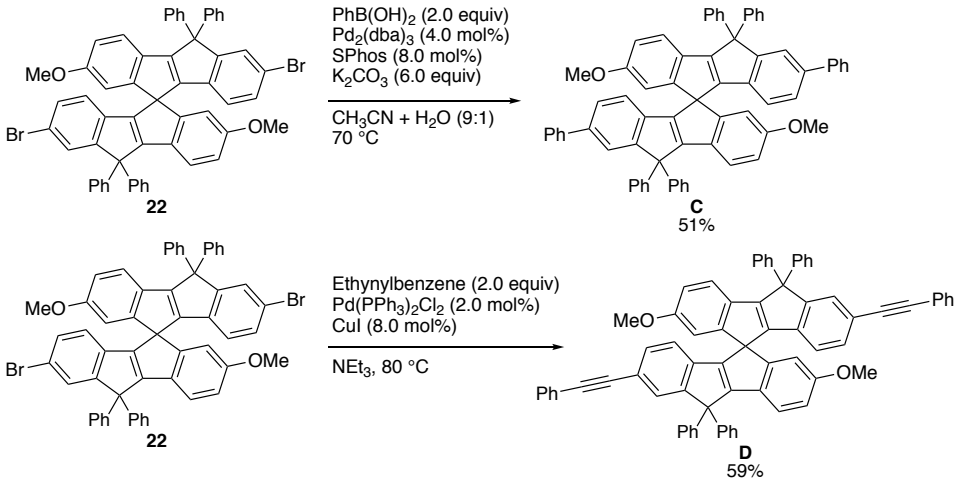

4.3. Calculation study

Time-dependent (TD) DFT calculation suggested the enhancement of absorption. I conducted TD-DFT calculation of **A** and its 2,2'-diphenyl and 2,2'-bis(phenylethynyl) derivatives, where the methoxy groups are omitted to simplify the model and avoid the structural disorder (Figure 4.3). The wavelength for π-π* transition from HOMO to LUMO increased by extension of π-system to reflect smaller HOMO–LUMO gap. Attachment of the π groups also increased oscillator strength (*f*) twofold. This result suggests that compound **C** and **D** would show much stronger absorption than **B**.

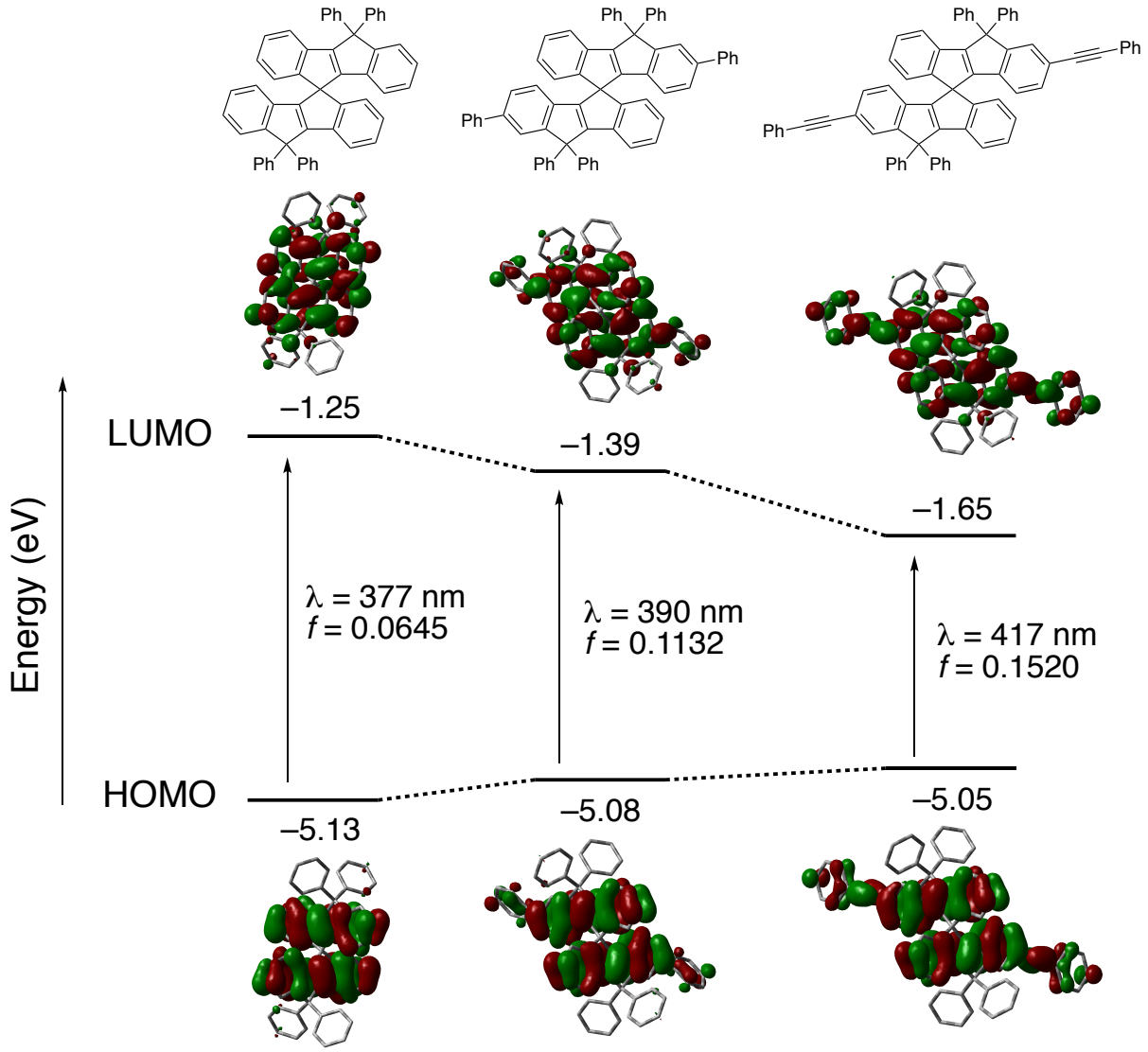

Figure 4.3. Energy levels of HOMO and LUMO, and the oscillator strength for the optical transition in the optimized structures of spiro-CPVs in their ground states obtained by TD-DFT calculation (B3LYP/6-31G(d,p) for structure optimization, TD B3LYP/6-31G(d) for oscillator strength and wavelength).

4.4. Photophysical properties

In order to find out the effect of π-elongation, the absorption and fluorescence spectra of **B**–**D** were investigated (Figure 4.4). Both of the spectra showed bathochromic peak shift, reflecting the π-conjugation length of the compounds. The addition of phenyl and phenylethynyl groups resulted in the increase of extinction coefficient from $\varepsilon = 4.10 \times 10^4$ L mol^{-1} cm^{-1} for **B** to 1.03×10^5 L mol^{-1} cm^{-1} for **C** and 1.01×10^5 L mol^{-1} cm^{-1} for **D**, as expected in the result of calculation study described in section *4.2.1*. The small Stokes shifts (Table 4.1), similar to compound **A**, suggest that the structural

rigidity to avoid geometry reorganization upon photoexcitation is still retained even after the addition of the functional groups. The fluorescence quantum yield Φ_{FL} increased by the expansion of π-system (Figure 4.5, black line). The experimental radiative rate constant k_r (Figure 4.5, grey line), determined by Φ_{FL} and fluorescence lifetime τ, also increased in order of **D** > **C** > **B**. These results suggest that the radiative decay is enhanced by the extension of π-conjugation system, which resulted in the increase of Φ_{FL}. Especially, compound **D** exhibited very intense photoluminescence with Φ_{FL} of 0.99, the highest for small organic CPL emitters. In addition, the k_r of 4.07×10^8 s^{-1} for **D** indicates the potential for its laser application.[8]

Enantiomerically pure **B**–**D** exhibited CD and CPL with $|g_{abs}|$ of 4.0–5.7 × 10^{-4} and $|g_{lum}|$ of 2.7–3.9 × 10^{-4}. Each enantiomer showed mirror image spectra, respectively (Figure 4.6). No relationship between g values and the length of π-system implies that electron transition takes place rather in each single COPV unit.

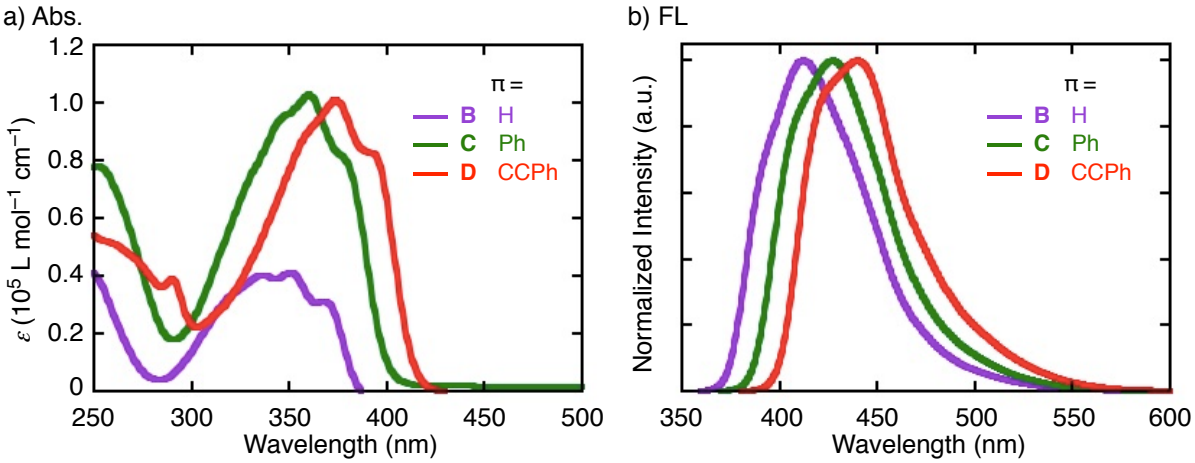

Figure 4.4. a) Absorption and b) fluorescence spectra of **B**–**D** in dichloromethane (1.0×10^{-5} M for absorption and 1.0×10^{-6} M for fluorescence).

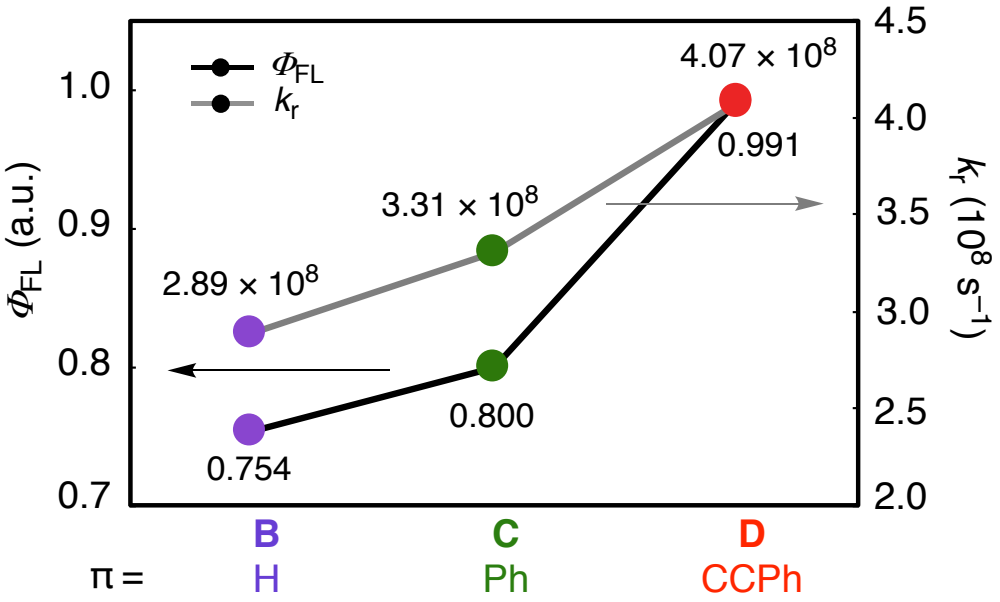

Figure 4.5. Effect of π-conjugation on fluorescence quantum yields Φ_{FL} (black, left) and radiative rate constant k_r (grey, right).

Table 4.1. Photophysical properties of **B**–**D**.

	λ_{abs}[a] (nm)	λ_{FL}[b] (nm)	$\Delta\nu$[c] (nm)	Φ_{FL}[d]	τ[e] (nm)	k_r[f] (10^8 s^{-1})	k_{nr}[g] (10^7 s^{-1})	$\lvert g_{abs}\rvert$[h] (10^{-4})	$\lvert g_{lum}\rvert$[i] (10^{-4})	$\lvert[\alpha]_D^{20}\rvert$ (*c*)[j]
B	368, 351, 336	413	62	0.75	2.61	2.89	9.43	4.1	3.5	247 (0.071)
C	379, 360	427	67	0.80	2.42	3.31	8.27	5.7	3.9	289 (0.058)
D	395, 374	440	66	0.99	2.43	4.07	0.37	4.0	2.7	228 (0.057)

[a] Absorption maximum wavelengths measured in dichloromethane. [b] Fluorescence maximum wavelengths measured in dichloromethane. [c] Stokes shift. [d] Fluorescence quantum yield determined using the absolute method. [e] Fluorescence lifetime measured with the time-correlated single-photon counting operation mode. [f] radiative rate constant. [g] Nonradiative rate constant. [h,i] Measured in dichloromethane. Wavelengths for $|g_{abs}|$ are 345 nm for **B**, 355 nm for **C**, and 364 nm for **D**; wavelength for $|g_{lum}|$ is 425 nm for **B**, 434 nm for **C**, and 445 nm for **D**. [j] Specific rotation in dichloromethane. Concentration (g mL^{-1}) in parentheses.

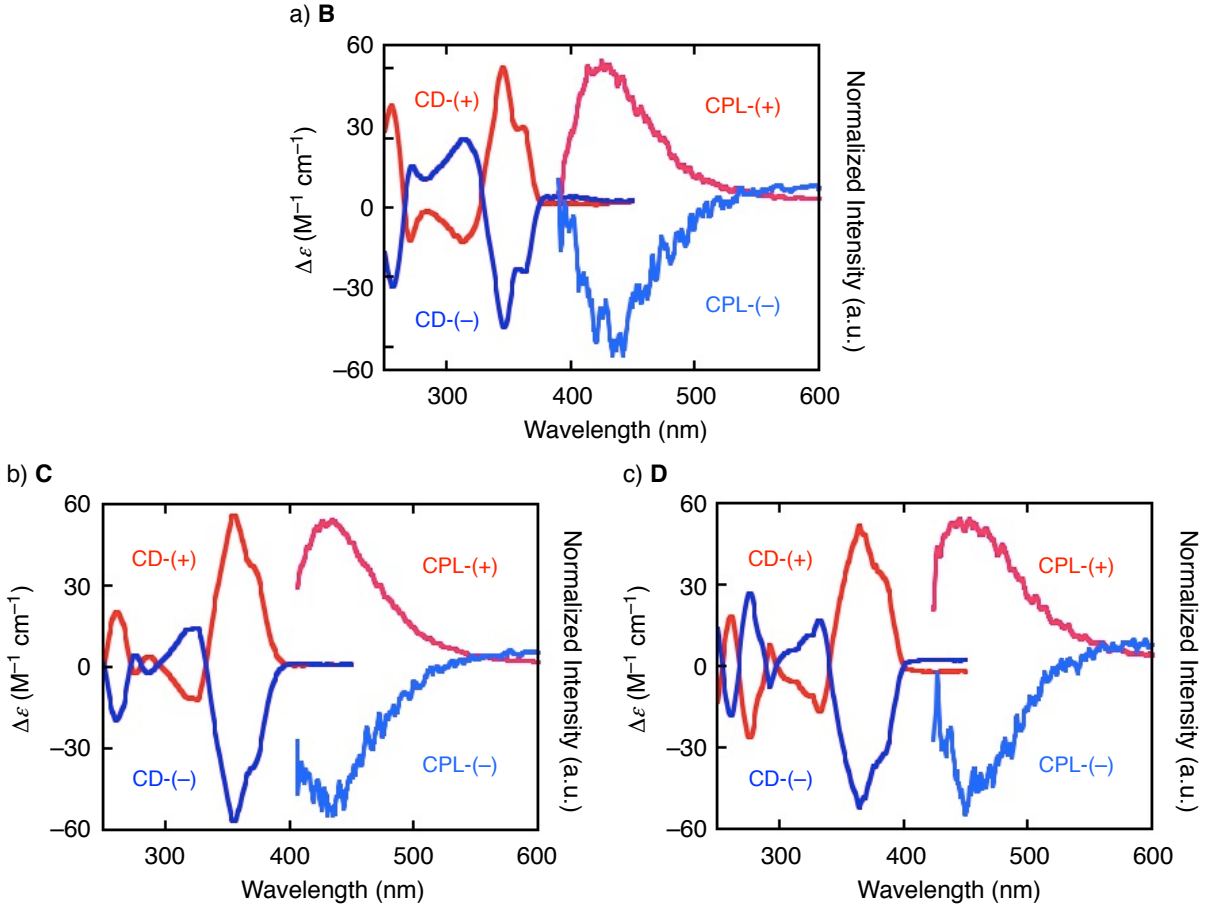

Figure 4.6. CD and CPL spectra of **B**–**D** in dichloromethane (1.0×10^{-5} M).

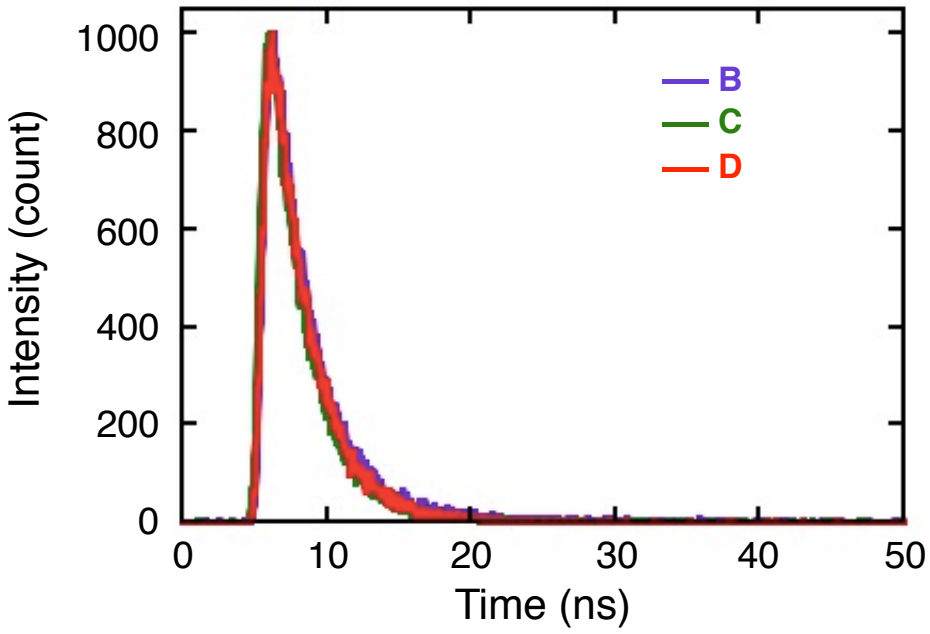

Figure 4.7. Fluorescence lifetime of **B**–**D** in dichloromethane (1.0×10^{-6} M).

4.5. Summary

In summary, the enhancement of radiative decay was achieved by the elongation of π-system of spiro-CPV. Absorption and fluorescence spectra showed the small Stokes shifts of the spiro-CPVs, reflecting the structural rigidity, and the increase of ε by π-elongation. Fluorescence lifetime measurement revealed the radiative decay is successfully accelerated as well, to afford high fluorescence quantum yield. The spiro-CPV-based CPL emitter with the highest ever Φ_{FL} was achieved. This study demonstrated the strategic enhancement of Φ_{FL} and k_r and expanded the opportunity for photoluminescent application of spiro-CPV materials.

4.6. Experimental section

4.6.1. Synthesis

General consideration

All the reactions dealing with air- or moisture-sensitive compounds were carried out in a dry reaction vessel under a positive pressure of N_2 or Ar gas. Air- and moisture-sensitive liquids and solutions were transferred via syringe or Teflon cannula. Analytical thin-layer chromatography (TLC) was performed using glass plates pre-coated with 0.25 mm, 230–400 mesh silica gel impregnated with a fluorescent indicator (254 nm). Thin-layer chromatography plates were visualized by exposure to ultraviolet light (UV). Organic solutions were concentrated by rotary evaporation at ca. 15 Torr (evacuated with a diaphragm pump). Flash column chromatography was performed as described by Still *et al*.[12], employing Kanto Silica gel 60 (spherical, neutral, 140–325 mesh).

Unless otherwise noted, commercial reagents were purchased from Tokyo Kasei Co., Aldrich Inc., and other commercial suppliers and used as purchased. Anhydrous solvents were purchased from Kanto, and purified by a solvent purification system (GlassContour) equipped with columns of activated alumina and copper catalyst prior to use.

NMR spectra were recorded using a JEOL ECZ-500 (^{1}H NMR, 500 MHz; ^{13}C NMR, 125 MHz) NMR spectrometer. Chemical data for protons are reported in parts per million (ppm, δ scale) downfield from tetramethylsilane and are referenced to the residual protons in the NMR solvent ($CDCl_3$: δ 7.26, CD_2Cl_2: δ 5.32). Chemical data for carbons are reported in parts per million (ppm, δ scale) downfield from tetramethylsilane and are referenced to the carbon resonance of the solvent ($CDCl_3$: δ 77.0, CD_2Cl_2: δ 54.0). The data are presented as follows: chemical shift, multiplicity (s = singlet, d = doublet, t = triplet, m = multiplet and/or multiple resonances, br = broad), coupling constant in Hertz (Hz), and integration. Melting points of solid materials were determined on a Mel-Temp II capillary melting-point apparatus and are uncorrected. Mass spectra were obtained on JEOL AccuTOF JMS-T100LC (APCI) mass spectrometer.

Synthetic procedures

7,7'-Dimethoxy-2,2'-diphenyl-spiro-CPV (**C**)

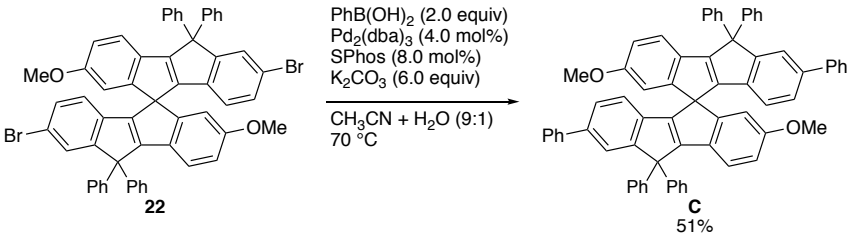

Phenylboronic acid (6.3 mg, 0.026 mmol), $Pd_2(dba)_3$ (0.1 mg, 0.10 μmol), SPhos (0.09 mg, 0.21 μmol) , potassium carbonate (21.6 mg, 0.16 mmol), and **22** (23.8 mg, 0.026 mmol) was dissolved in acetonitrile (0.90 mL) and water (0.10 mL), and heated to 70 ºC. After stirring for 15 h, the reaction mixture was cooled to ambient temperature and added water. The organic layer was extracted with CH_2Cl_2, dried over anhydrous Na_2SO_4, and evaporated *in vacuo*. The crude mixture was purified by column chromatography (eluent: CH_2Cl_2/hexane = 1/2) to afford **C** (12.0 mg, 51%) as a white solid. Mp: 340–344 ºC; ^{1}H NMR (500 MHz, CD_2Cl_2) δ 3.63 (s, 6H), 6.29 (d, *J* = 7.4 Hz, 2H), 6.47 (d, *J* = 2.3 Hz, 2H), 6.77 (dd, *J* = 8.6, 2.3 Hz, 2H), 6.77 (dd, *J* = 8.0, 1.7 Hz, 2H), 7.13 (dd, *J* = 8.0, 1.7 Hz, 2H), 7.26 (t, *J* = 7.7 Hz, 2H), 7.31–7.44 (m, 24H), 7.54–7.58 (m, 4H), 7.62 (d, *J* = 1.7 Hz, 2H), 7.62 (d, *J* = 1.7 Hz, 2H); ^{13}C NMR (125 MHz, CD_2Cl_2) δ 55.7, 60.0, 64.5, 110.6, 112.7, 119.7, 121.5, 124.0, 126.6, 127.3, 127.5, 128.7, 128.8, 128.92, 128.95, 128.99, 133.4, 137.4, 139.0, 141.6, 143.1, 143.3, 147.6, 152.1, 157.4, 159.2, 159.6; HRMS (APCI+) calcd for $C_{69}H_{48}O_2$ (M): 909.1182; found: 909.1168.

7,7'-Dimethoxy-2,2'-bis(phenylethynyl)-spiro-CPV (**D**)

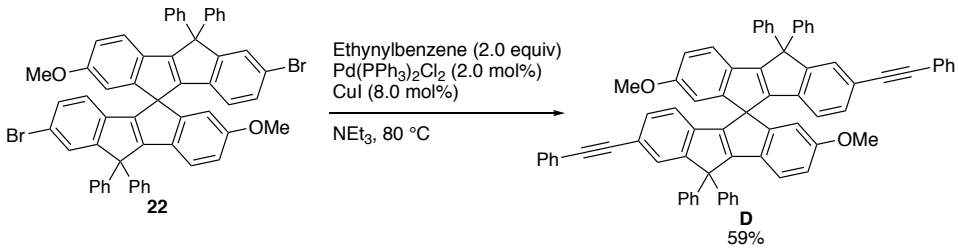

Ethynylbenzene (5.84 mg, 0.57 mmol), $Pd(PPh_3)_2Cl_2$ (0.38 mg, 0.54 μmol), CuI (0.21 mg, 1.09 μmol), and **22** (24.9 mg, 0.027 mmol) was dissolved in triethylamine (1.0 mL) and heated to 80 ºC. After stirring for 15 h, the reaction mixture was cooled to ambient temperature and added aqueous NH_4Cl solution. The organic layer was extracted with CH_2Cl_2, dried over anhydrous Na_2SO_4, and evaporated *in vacuo*. The crude mixture was purified by column chromatography (eluent: CH_2Cl_2/hexane = 1/2) to

afford **D** (15.3 mg, 59%) as a white solid. Mp: 338–341 ºC; ^{1}H NMR (500 MHz, CD_2Cl_2) δ 3.63 (s, 6H), 6.15 (d, *J* = 7.4 Hz, 2H), 6.45 (d, *J* = 2.3 Hz, 2H), 6.78 (dd, *J* = 8.3, 2.6 Hz, 2H), 7.06 (dd, *J* = 7.4, 1.1 Hz, 2H), 7.26 (d, *J* = 8.0 Hz, 2H), 7.29–7.33 (m, 6H), 7.34–7.41 (m, 16H), 7.42–7.45 (m, 4H), 7.52 (t, *J* = 6.9 Hz, 6H); ^{13}C NMR (125 MHz, CD_2Cl_2) δ 52.5, 55.4, 64.0, 90.1, 103.3, 110.3, 112.6, 119.1, 119.9, 121.6, 123.3, 127.4, 127.7, 128.2, 128.4, 128.5, 128.6, 128.7, 131.0, 131.4, 132.7, 138.0, 142.2, 142.4, 151.7, 156.5, 159.1, 160.4; HRMS (APCI+) calcd for $C_{73}H_{48}O_2$ (M): 957.1516; found: 957.1489.

4.6.2. Characterization

Computational study

The DFT and TD-DFT calculations for 2,2'-substituted spiro-CPVs were conducted at the B3LYP/6-31G (d,p) and TD B3LYP/6-31G(d) levels on Gaussian09 packages.[13]

Table 4.2. Theoretically optimized coordinates of 2,2'-diphenyl-spiroCPV calculated at the B3LYP/6-31G(d,p) level of theory.

Total energy: *E*(RB3LYP/6-31G(d,p)) = –2579.71333433 Hartree

Center Number	Atomic Number	Atomic Type	Coordinates (Angstroms) X	Y	Z
1	6	0	1.747342	-2.977016	-3.05143
2	1	0	2.700746	-2.800671	-3.536897
3	6	0	0.844452	-3.904205	-3.58105
4	1	0	1.10538	-4.447608	-4.484607
5	6	0	-0.38753	-4.138369	-2.965741
6	1	0	-1.076263	-4.860313	-3.394349
7	6	0	-0.744103	-3.448313	-1.798514
8	6	0	1.398557	-2.285602	-1.88877
9	6	0	0.147652	-2.529999	-1.268994
10	1	0	-1.702187	-3.629794	-1.319848
11	6	0	2.073146	-1.256291	-1.103362
12	6	0	1.29233	-0.876626	-0.059799
13	6	0	3.423493	-0.539818	-1.095368

14	6	0	3.219959	0.379511	0.137619
15	6	0	1.951413	0.151853	0.724544
16	6	0	4.076495	1.328048	0.668357
17	6	0	3.692119	2.073881	1.803877
18	6	0	2.428502	1.835071	2.372836
19	6	0	1.555817	0.884587	1.844488
20	1	0	0.584424	0.720285	2.299119
21	1	0	2.135478	2.388907	3.259384
22	1	0	5.034749	1.529689	0.20127
23	6	0	3.686375	0.326215	-2.340339
24	6	0	2.661934	0.648689	-3.238773
25	6	0	4.9608	0.870466	-2.568023
26	6	0	2.898689	1.493466	-4.325478
27	1	0	1.672064	0.229134	-3.097931
28	6	0	5.198205	1.716514	-3.649697
29	1	0	5.779346	0.615956	-1.902466
30	6	0	4.165859	2.034316	-4.534285
31	1	0	2.08727	1.72444	-5.009783
32	1	0	6.193252	2.124416	-3.802965
33	1	0	4.350445	2.690783	-5.379469
34	6	0	4.523184	-1.605624	-0.863906
35	6	0	4.844909	-2.039765	0.430131
36	6	0	5.156994	-2.231099	-1.947119
37	6	0	5.774419	-3.05992	0.633945
38	1	0	4.368034	-1.575121	1.286187
39	6	0	6.087895	-3.250825	-1.744251
40	1	0	4.934483	-1.909157	-2.95884
41	6	0	6.402532	-3.670154	-0.452115
42	1	0	6.009435	-3.373922	1.647053
43	1	0	6.567588	-3.71525	-2.601185

44	1	0	7.129286	-4.461324	-0.293046
45	6	0	0.000042	-1.667223	0.000398
46	6	0	-0.147846	-2.529937	1.26976
47	6	0	-1.29214	-0.876387	0.060428
48	6	0	-1.398804	-2.28539	1.889375
49	6	0	-2.073178	-1.256031	1.103843
50	6	0	-1.951088	0.15206	-0.724086
51	6	0	-3.423641	-0.539763	1.095369
52	6	0	-3.219827	0.37958	-0.137527
53	6	0	-4.522912	-1.605909	0.863286
54	6	0	-5.157082	-2.231582	1.94617
55	6	0	-4.843939	-2.040052	-0.430925
56	6	0	-6.087609	-3.251558	1.742826
57	1	0	-4.935171	-1.909609	2.958013
58	6	0	-5.773058	-3.060464	-0.635212
59	1	0	-4.366817	-1.575221	-1.286739
60	6	0	-6.401506	-3.670933	0.450527
61	1	0	-6.56758	-3.716136	2.599521
62	1	0	-6.007527	-3.374477	-1.648445
63	1	0	-7.12796	-4.462298	0.291071
64	6	0	-3.687394	0.326215	2.340149
65	6	0	-2.663285	0.649446	3.23872
66	6	0	-4.962094	0.869994	2.567335
67	6	0	-2.900704	1.494311	4.325192
68	1	0	-1.673152	0.230444	3.098068
69	6	0	-5.200163	1.716148	3.648797
70	1	0	-5.780319	0.615074	1.901537
71	6	0	-4.168209	2.034562	4.5336
72	1	0	-2.089566	1.725868	5.009634
73	1	0	-6.195425	2.123664	3.8017

74	1	0	-4.353308	2.691114	5.378607
75	6	0	-1.747719	-2.976604	3.052114
76	6	0	0.743782	-3.448269	1.799463
77	6	0	0.387052	-4.138167	2.966734
78	1	0	1.075689	-4.860116	3.395489
79	6	0	-0.844952	-3.903806	3.581922
80	1	0	-1.105985	-4.44705	4.485544
81	1	0	1.701891	-3.629875	1.320896
82	1	0	-2.701117	-2.800079	3.537525
83	6	0	-4.076244	1.32819	-0.668307
84	6	0	-1.555193	0.88503	-1.843776
85	6	0	-2.42779	1.835536	-2.372234
86	1	0	-2.13454	2.38953	-3.258616
87	6	0	-3.691572	2.074217	-1.803597
88	1	0	-0.583603	0.720969	-2.298067
89	1	0	-5.034552	1.529825	-0.201303
90	6	0	4.605693	3.090152	2.383407
91	6	0	5.993128	2.870053	2.435556
92	6	0	4.109248	4.300898	2.897147
93	6	0	6.851087	3.823538	2.980848
94	1	0	6.397999	1.931388	2.0692
95	6	0	4.966709	5.253476	3.444477
96	1	0	3.044452	4.506072	2.841487
97	6	0	6.342184	5.019874	3.48883
98	1	0	7.918867	3.6269	3.017419
99	1	0	4.55991	6.18492	3.82797
100	1	0	7.010528	5.762629	3.914298
101	6	0	-4.604933	3.090611	-2.383156
102	6	0	-4.108292	4.301407	-2.896579
103	6	0	-5.992363	2.870608	-2.435632

104	6	0	-4.965563	5.254121	-3.443958
105	1	0	-3.043498	4.506525	-2.84058
106	6	0	-6.850142	3.824242	-2.98095
107	1	0	-6.39737	1.931886	-2.069558
108	6	0	-6.341052	5.020623	-3.488647
109	1	0	-4.558621	6.185619	-3.827168
110	1	0	-7.917923	3.627658	-3.017814
111	1	0	-7.00925	5.763493	-3.914143

Table 4.3. Theoretically optimized coordinates of 2,2'-bis(phenylethynyl)-spiroCPV calculated at the B3LYP/6-31G(d,p) level of theory.

Total energy: *E*(RB3LYP/6-31G(d,p)) = –2732.02651516 Hartree

Center	Atomic	Atomic	Coordinates (Angstroms)		
Number	Number	Type	X	Y	Z
1	6	0	-1.085379	-3.414397	3.354714
2	1	0	-1.917761	-3.230192	4.024713
3	6	0	-0.093361	-4.339522	3.69393
4	1	0	-0.16192	-4.87499	4.636389
5	6	0	0.98464	-4.581908	2.83892
6	1	0	1.74616	-5.302399	3.122092
7	6	0	1.093468	-3.90243	1.617403
8	6	0	-0.983313	-2.733747	2.138943
9	6	0	0.112074	-2.986338	1.275798
10	1	0	1.932372	-4.089172	0.953004
11	6	0	-1.804757	-1.70937	1.501901
12	6	0	-1.254489	-1.337543	0.317086
13	6	0	-3.131618	-0.997932	1.763752
14	6	0	-3.18961	-0.091976	0.506416
15	6	0	-2.066049	-0.323291	-0.327488

16	6	0	-4.145215	0.839616	0.150238
17	6	0	-4.000347	1.562997	-1.059224
18	6	0	-2.877443	1.323714	-1.87943
19	6	0	-1.912065	0.387747	-1.520441
20	1	0	-1.048588	0.220735	-2.155428
21	1	0	-2.774377	1.887085	-2.800823
22	1	0	-5.007354	1.034083	0.778177
23	6	0	-3.139301	-0.118241	3.026839
24	6	0	-1.954906	0.213265	3.695691
25	6	0	-4.342123	0.430712	3.500266
26	6	0	-1.967412	1.071152	4.797707
27	1	0	-1.013612	-0.208433	3.361266
28	6	0	-4.356225	1.289629	4.597538
29	1	0	-5.278375	0.170686	3.016849
30	6	0	-3.166816	1.615942	5.251961
31	1	0	-1.034491	1.309501	5.300454
32	1	0	-5.299981	1.7013	4.943715
33	1	0	-3.177603	2.282913	6.108875
34	6	0	-4.249033	-2.071283	1.771971
35	6	0	-4.812827	-2.531665	0.573283
36	6	0	-4.657087	-2.67571	2.969548
37	6	0	-5.759469	-3.556227	0.573386
38	1	0	-4.515602	-2.082413	-0.36801
39	6	0	-5.605391	-3.699749	2.970618
40	1	0	-4.244287	-2.334042	3.912738
41	6	0	-6.16231	-4.144978	1.772401
42	1	0	-6.18591	-3.889527	-0.368481
43	1	0	-5.908068	-4.147113	3.91314
44	1	0	-6.902954	-4.939214	1.772721
45	6	0	0.000015	-2.128707	0.000033

46	6	0	-0.112146	-2.986245	-1.275798
47	6	0	1.25454	-1.337591	-0.317021
48	6	0	0.983191	-2.73361	-2.138992
49	6	0	1.8047	-1.709303	-1.501922
50	6	0	2.066181	-0.323432	0.327594
51	6	0	3.131529	-0.997835	-1.763837
52	6	0	3.189662	-0.092025	-0.506395
53	6	0	4.248963	-2.071165	-1.772326
54	6	0	4.656956	-2.675385	-2.970022
55	6	0	4.812825	-2.531742	-0.573741
56	6	0	5.605279	-3.699413	-2.971314
57	1	0	4.244093	-2.333577	-3.913135
58	6	0	5.759484	-3.556283	-0.574066
59	1	0	4.515637	-2.082651	0.367641
60	6	0	6.162273	-4.144827	-1.773205
61	1	0	5.907906	-4.146614	-3.913928
62	1	0	6.185983	-3.889737	0.36772
63	1	0	6.902931	-4.939049	-1.773694
64	6	0	3.139046	-0.117997	-3.026827
65	6	0	1.954597	0.21344	-3.695614
66	6	0	4.341794	0.431129	-3.500252
67	6	0	1.966974	1.071437	-4.79755
68	1	0	1.013358	-0.208405	-3.361223
69	6	0	4.355768	1.290152	-4.597439
70	1	0	5.278092	0.171146	-3.016902
71	6	0	3.1663	1.616404	-5.25179
72	1	0	1.034008	1.309724	-5.300244
73	1	0	5.299469	1.701954	-4.943611
74	1	0	3.176986	2.283459	-6.108639
75	6	0	1.085172	-3.414176	-3.354818

76	6	0	-1.09358	-3.90229	-1.617409
77	6	0	-0.984838	-4.581683	-2.838981
78	1	0	-1.746387	-5.302141	-3.122156
79	6	0	0.093117	-4.339258	-3.694039
80	1	0	0.16161	-4.874663	-4.636538
81	1	0	-1.932449	-4.089062	-0.952974
82	1	0	1.917521	-3.229939	-4.02485
83	6	0	4.145314	0.839501	-0.150178
84	6	0	1.912328	0.387429	1.520667
85	6	0	2.877753	1.323337	1.879688
86	1	0	2.774791	1.886578	2.801172
87	6	0	4.000577	1.562715	1.059401
88	1	0	1.048929	0.220308	2.155732
89	1	0	5.007414	1.034034	-0.77815
90	6	0	-6.805074	4.295799	-2.145583
91	6	0	-7.910582	4.561211	-1.311847
92	6	0	-6.691808	4.994043	-3.365206
93	6	0	-8.869977	5.495597	-1.690356
94	1	0	-8.002427	4.027072	-0.371817
95	6	0	-7.656481	5.92644	-3.735041
96	1	0	-5.842757	4.794208	-4.01062
97	6	0	-8.748116	6.181227	-2.901404
98	1	0	-9.716424	5.689991	-1.038152
99	1	0	-7.556562	6.457008	-4.677457
100	6	0	4.97979	2.521251	1.44119
101	6	0	5.821852	3.338847	1.763955
102	6	0	6.805425	4.295346	2.145873
103	6	0	6.692361	4.99325	3.36571
104	6	0	7.910732	4.56108	1.311972
105	6	0	7.65704	5.925625	3.735598

106	1	0	5.843463	4.793173	4.011251
107	6	0	8.87013	5.495436	1.690534
108	1	0	8.002411	4.027207	0.371774
109	6	0	8.748475	6.180724	2.9018
110	1	0	7.557278	6.455926	4.678181
111	1	0	9.716422	5.690083	1.038205
112	1	0	9.499096	6.909042	3.193867
113	1	0	-9.49873	6.909563	-3.193441
114	6	0	-4.979526	2.521588	-1.440973
115	6	0	-5.821535	3.339251	-1.763699

Photophysical properties

UV-Vis absorption spectra were measured with a JASCO V-670 spectrometer. Fluorescence spectra were measured with a HITACHI F-4500 spectrometer. Photoluminescence quantum yields were measured on Hamamatsu Photonics C9920–02 Absolute PL Quantum Yield Measurement System, and absolute quantum yields were determined by using a calibrated integrating sphere system. Fluorescence lifetimes were measured on Hamamatsu Photonics C11367-02 Quantaurus-Tau. CD spectra were measured on a JASCO J-1500 spectropolarimeter. CPL spectra were measured on a JASCO CPL-200 spectrometer. Optical rotations were measured on a JASCO P-1030 polarimeter using a 50-mm cell. The absorption maximum wavelengths were used as excitation wavelengths. Spectral grade solvent (dichloromethane) was used as solvent for UV-Vis absorption fluorescence, CD, CPL, and optical rotation measurements.

4.7. References

[1] Samuel, I. D.; Turnbull, G. A. *Chem. Rev.* **2007**, *107*, 1272–1295.

[2] Einstein, A. *Physik. Z.* **1917**, *18*, 121–128.

[3] (a) Perrin, F. *J. Phys. Radium* **1926**, *7*, 390–401. (b) Lewis, G. N.; Kasha, M. *J. Am. Chem. Soc.* **1945**, *67*, 994–1003.

[4] Strickler, S. J.; Berg, R. A. *J. Chem. Phys*. **1962**, *37*, 814–822.

[5] Peeters, E.; Ramos, A. M.; Meskers, S. C. J.; Janssen, R. A. *J. Chem. Phys.* **2000**, *112*, 9445–9454.

[6] Harabuchi, Y.; Taketsugu, T.; Maeda, S. *Phys. Chem. Chem. Phys.* **2015**, *17*, 22561–22565.

[7] (a) Harabuchi, Y.; Taketsugu, T.; Maeda, S. *Chem. Lett.* **2016**, *45*, 940–942. (b) Harabuchi, Y.; Saita, K.; Maeda, S. *Photochem. Photobiol. Sci.* **2018**, *17*, 317–322. (c) Ikemoto, K.; Tokuhira, T.; Uetani, A.; Harabuchi, Y.; Sato, S.; Maeda, S.; Isobe, H. *J. Org. Chem*. **2020**, *85*, 150–157.

[8] Aimono, T.; Kawamura, K.; Goushi, K.; Yamamoto, H.; Sasabe, H.; Adachi, C. *Appl. Phys. Lett.* **2005**, *86*, 071110.

[9] (a) Hanhela, P. J.; Paul, D. B. *Aust. J. Chem.* **1984**, *37*, 553–559. (b) Maeda, H.; Maeda, T.; Mizuno, K.; Fujimoto, K.; Shimizu, H.; Inouye, M. *Chem. Eur. J*. **2006**, *12*, 824–831. (c) Yamaji, M.; Nanai, Y.; Mizuno, K. *ISRN Phys. Chem*. **2012**, *2012*, 103817. (d) Hakoda, Y.; Aoyagi, M.; Irisawa, K.; Kato, S.; Nakamura, Y.; Yamaji, M. *Photochem. Photobiol. Sci.* **2016**, *15*, 1586–1593. (e) Abengózar, A.; Sucunza, D.; García-García, P.; Vaquero, J. J. *Beilstein J. Org. Chem.* **2019**, *15*, 1257–1261.

[10] (a) Miyaura, N.; Suzuki, A. *Chem. Rev.* **1995**, *95*, 2457–2483. (b) Lennox, A. J. J.; Lloyd-Jones, G. C. *Chem. Soc. Rev.* **2014**, *43*, 412–443.

[11] (a) Sonogashira, K.; Tohda, Y.; Hagihara, N. *Tetrahedron Lett.* **1975**, *16*, 4467–4470. (b) Chinchilla, R.; Nájera, C. *Chem. Rev*. **2007**, *107*, 874–922. (c) Chinchilla, R.; Nájera, C. *Chem. Soc. Rev*. **2011**, *40*, 5084–5121.

[12] Still, W. C.; Kahn, M.; Mitra, A. *J. Org. Chem. 1978,* **43**, 2923–2925.

[13] Gaussian 09, Revision B.01, Frisch, M. J.; Trucks, G. W.; Schlegel, H. B.; G. E. Scuseria, ; Robb, M. A.; Cheeseman, J. R.; Scalmani, G.; Barone, V.; Mennucci, B.; Petersson, G. A.; Nakatsuji, H.; Caricato, M.; Li, X.; Hratchian, H. P.; Izmaylov, A. F.; Bloino, J.; Zheng, G.; Sonnenberg, J. L.; Hada, M.; Ehara, M.; Toyota, K.; Fukuda, R.; Hasegawa, J.; Ishida, M.; Nakajima, T.; Honda, Y.; Kitao, O.; Nakai, H.; Vreven, T.; Montgomery Jr. J. A.; , Peralta, J. E.; Ogliaro, F.; Bearpark, M.; Heyd, J. J.; Brothers, E.; Kudin, K. N.; Staroverov, V. N.; Keith, T.; Kobayashi, R.; Normand, J.; Raghavachari, K.; Rendell, A.;

Burant, J. C.; Iyengar, S. S.; Tomasi, J.; Cossi, M.; Rega, N.; Millam, J. M.; Klene, M.; Knox, J. E.; Cross, J. B.; Bakken, V.; Adamo, C.; Jaramillo, J.; Gomperts, R.; Stratmann, R. E.; Yazyev, O.; Austin, A. J.; Cammi, R.; Pomelli, C.; Ochterski, J. W.; Martin, R. L.; Morokuma, K.; Zakrzewski, V. G.; Voth, G. A.; Salvador, P.; Dan nenberg, J. J.; Dapprich, S.; Daniels, A. D.; Farkas, O.; Foresman, J. B.; Ortiz, J. V.; Cioslowski, J.; Fox, D. J. Gaussian, Inc., Wallingford CT, 2010.

Chapter 5.

Spiro-conjugated Carbon and Heteroatom-co-bridged *p*-Phenylenevinylenes: Synthesis, Materials Properties, and Solvatochromic CPL

Chapter 5

本章については，５年以内に雑誌等で刊行予定のため，非公開.

Chapter 6.

Synthesis and Semiconducting Properties of Spiro-CPV-based Hole Transporting Materials

6.1. Introduction

6.1.1. Organic semiconductor devices

The importance of organic semiconductor devices has been continuously increasing since the mid of 1980s. Tang reported the first organic photovoltaic cell in 1986.[1] In 1987, organic field-effect transistor and organic light-emitting diode are demonstrated by Ando *et al*.[2] and VanSlyke *et al.*,[3] respectively.

The use of organic semiconducting materials offers advantages over the inorganic semiconductor devices. The organic materials can be processed by various printing methods, such as vapor deposition and wet processing, which make device fabrications less cost, and scalable. Because the organic materials are generally accumulated by van der Waals force in solid, their films are light and flexible. In addition, the color, energy levels, and other semiconducting properties could be tuned by molecular design. Therefore, the desired device properties could be accessed by the development of new organic semiconductor materials.

6.1.2. Perovskite solar cell

We depend on fossil fuels for main energy source. However, there are some risks in this situation, such as environmental contamination and depletion. Photovoltaics have attracted much interest as a clean and feasible energy source where solar energy is converted to electricity. Perovskite solar cell (PVSC) is one of the most promising photovoltaic devices since the first report by Miyasaka *et al.*[4] due to high power conversion efficiencies (PCEs) and solution-based device fabrication process.

PVSCs have layer structures composed of electrodes, carrier transport layers (hole and electron transport layer, HTL and ETL), and a perovskite layer as a photoactive layer (standard structure, Figure 6.1). Metal halide perovskite materials are generally used for the active layer.[5] Though lead has been conventionally used for the metal in perovskite, the use of other metals are also developed due to the toxicity of lead.[6] Because perovskite materials are ambipolar, the order of layers could be inverted (inverted structure, Anode/HTL/perovskite/ETL/Cathode from the bottom).

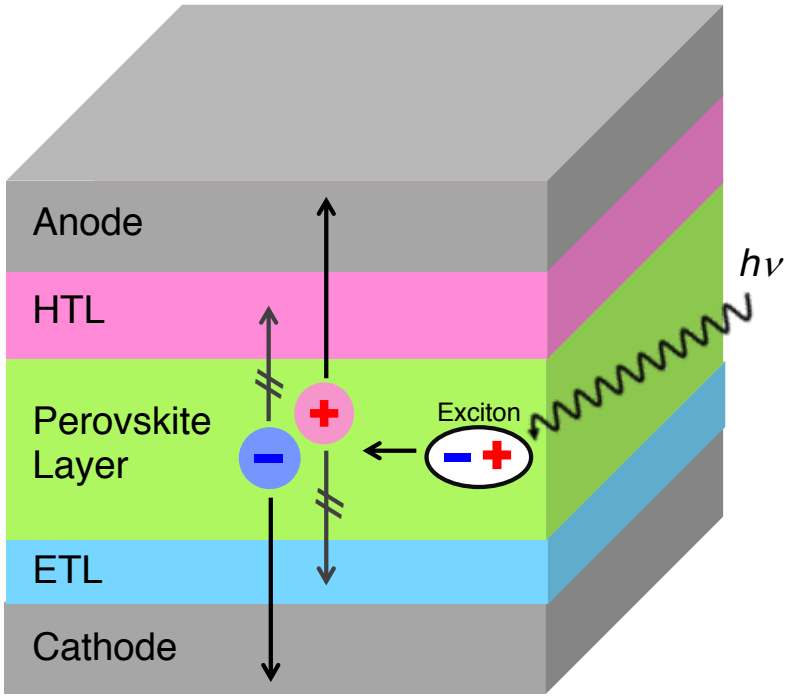

Figure 6.1. Device structure of standard-type perovskite solar cells.

Upon photoirradiation, excitons are generated by photoexcitation of perovskite materials, followed by the generation of hole and electron. These polarons are transferred to each electrode and used as current electricity in external circuits. As well as the photoactivity of perovskite layer, efficient carrier transfer without recombination of the polarons is quite important to achieve high PCEs. In this regard, hole transport materials (HTMs, Figure 6.2) are required to have high hole mobility and aligned HOMO energy level with perovskite layer for efficient hole transfer. In order to avoid carrier recombination, its LUMO level should be high. For the wet fabrication process and device stability, the solution-processed film of HTM should have high phase stability in amorphous state.

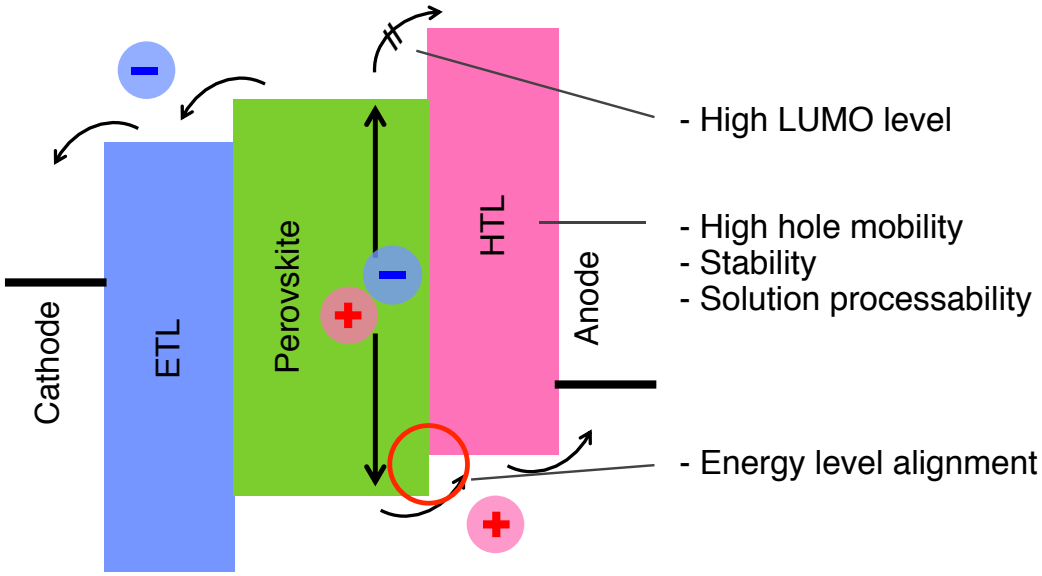

Figure 6.2. Energy diagram of the components of perovskite solar cells and properties required for hole transporting materials.

6.1.3. Spiro compounds for hole transporting materials (HTMs)

Spiro compounds have been used as carrier transporting materials[7] in organic light-emitting diodes,[8] organic field-effect transistors,[9] organic phototransistors,[10] and solar cells.[11] Thanks to the isotropic electronic structure via spiroconjugation, spiro compounds have small reorganization energy and fast intermolecular charge transfer to enhance carrier mobility,[12,13] as similarly seen in spherical fullerene semiconducting materials.[14] In addition, their three-dimensional structure effectively increases solubility and inhibits crystallization to form amorphous films with high glass transition temperature (T_g) that influence on the device stability.[15]

Since Grätzel and coworkers reported the use for solid state dye-sensitized solar cells in 1998, 2,2',7,7'-tetrakis(*N*,*N*-di-*p*-methoxyphenyl-amine)9,9'-spirobifluorene (Spiro-OMeTAD, Figure 6.3)[11,15,16] has been one of the most common HTM, especially for PVSCs, because of their efficient hole transporting and solution-processability. In the four terminals of spirobifluorene, di-(*p*-methoxyphenyl)amino groups are incorporated to increase solubility and enhance the interaction between perovskite layer because of branched structure. Methoxy groups decrease HOMO level by resonance electron-donating effect to achieve good energy level alignment with adjacent layers. Seok *et al.* reported the energy level tuning of the HTM by changing the position of methoxy groups to utilize the resonance effects.[17] Huang *et al.* dealt with the HOMO level tuning by replacing oxygen atoms of

methoxy groups with other elements (C, S, N).[18] Regarding the hole transporting, it is reported the chemical doping of lithium bis(trifluoromethanesulfonyl)imide (LiTFSI) into the HTMs improves conductivity of hole transporting layer to increase the device performance.[19,20] Similar effect is observed for COPV-based HTM, reported by our laboratory,[21] whose hole transporting property increased upon the oxidant doping. This improvement is because through-space homoconjugation in radical cation expands the charge delocalization over the whole structure to make reorganization energy smaller.

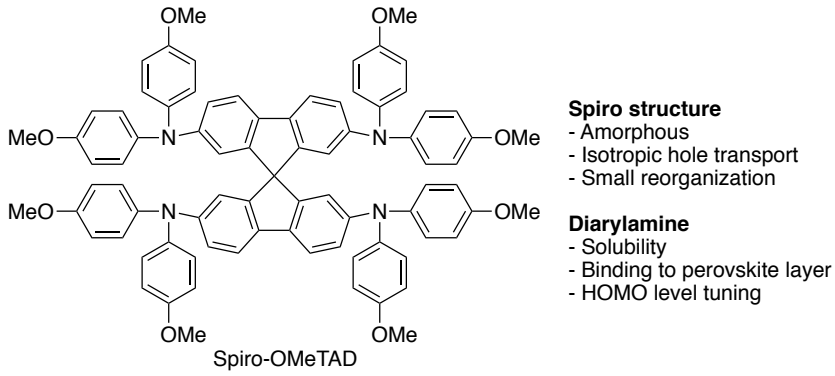

Figure 6.3. Molecular structure of spiro-OMeTAD.

6.1.4. Spiro-CPV-based HTMs: Chapter outline

Inspired by these materials, I envisioned the application of spiro-CPV for HTMs. In this chapter, the investigation on spiro-CPV-based HTMs are reported. I designed spiro-CPV-based HTMs by attaching diarylamines on 2 and 7 terminals of each COPV units (Figure 6.4). Two COPV units electronically connected via spiroconjugation would allow efficient intermolecular hole transfer. The spherical shape and rather higher molecular weight would enable solution processing and afford higher phase stability in amorphous state,[22] comparing to spiro-OMeTAD. As arylamino substituents, I chose di-(*p*-methoxyphenyl)amine for comparison with spiro-OMeTAD, and di-(*m*-methoxyphenyl)amine and di-(*p*-methylthiophenyl)amine derivatives for energy level tuning by the difference of resonance effect and electron-donating effect.

Section 6.2 describes the synthesis of spiro-CPV-based HTMs. In Section 6.3, thermal properties are reported to show their stabilities in amorphous states better than spiro-OMeTAD. Section 6.4 provides photophysical properties. Section 6.5–6.6 describe the investigation of oxidation process

of the HTMs by electrochemical measurements, absorption titration by oxidant, and electron spin resonance measurements. These studies suggested the efficient electronic interaction between two π-planes connected via spiro-linkage in radical cation states. In Section 6.7, the investigation on their hole mobilities are described. The novel HTMs showed better hole mobilities than the conventional spiro-OMeTAD. The mobility enhancement upon oxidant doping was observed in their spin-coated films. Section 6.8 provides the summary of this work.

It should be noted here that the fabrication of PVSC device in Section 6.7 is conducted by Dr. Zhongmin Zhou. I appreciate very much for his help.

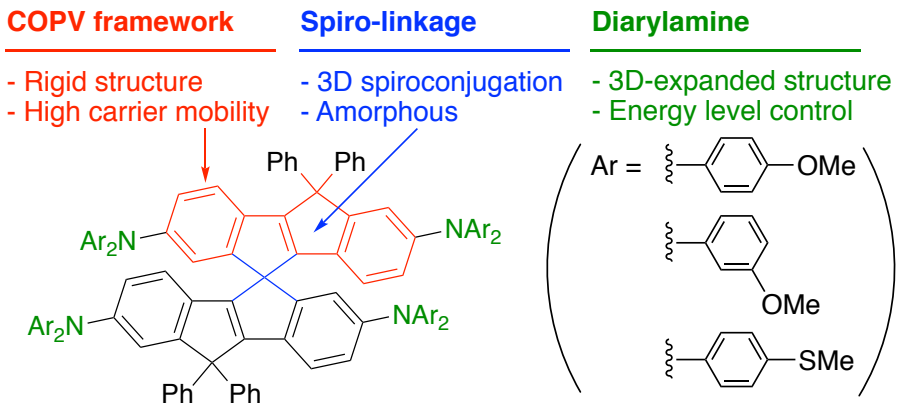

Figure 6.4. Molecular design of spiro-CPV-based HTMs.

6.2. Synthesis

The spiro-CPV-based hole transporting materials were successfully obtained from the tetraiodo spiro-CPV **20**. Buchwald–Hartwig amination[23] of **20** with the corresponding diarylamines afforded the tetrakis(diarylamino) compounds **I–K** in 89–59% yield (Scheme 6.1).

Scheme 6.1. Synthesis of **I**–**K** via Buchwald–Hartwig amination.

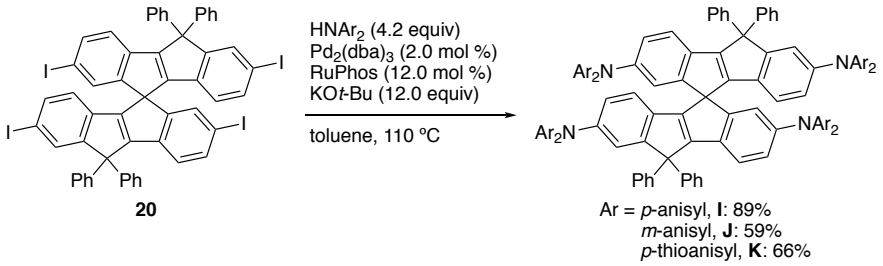

6.3. Thermal stability

TG and DSC measurements showed that **I**–**K** undergo 5% weight loss at T_{d5} = 350–388 °C and glass transition at T_g = 134–176 °C (Table 6.1. Figure 6.5), much higher than a popularly used spiro-OMeTAD (T_g = 120 °C).[16] I accredited the higher phase stabilities for spiro-CPVs to larger molecular weights, and possibly for more spherical configurations. Their thermal stabilities would be beneficial for the development of stable electronic devices in a wide range of temperature.[24] Lower T_{d5} of **K**, comparing to **I** and **J**, is due to the weaker C–S bond (ΔH_a = 62.0 kcal mol^{-1}) than C–O bond (ΔH_a = 84.0 kcal mol^{-1}),[25] while the larger molecular weight slightly improves its T_g.

Table 6.1. Thermal properties of **I**–**K**.

	T_{d5}[a] (°C)	T_g[b] (°C)
I	382	171
J	388	134
K	350	176

[a] 5% weight loss temperature determined by TG curve. [b] Glass transition temperature determined by DSC.

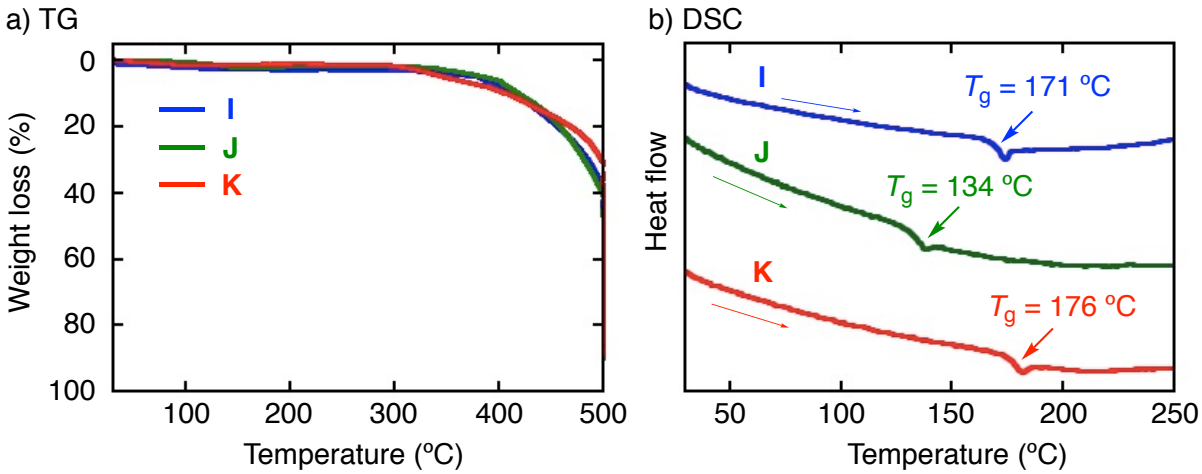

Figure 6.5. TG and DSC curve of **I**–**K** under N_2 atmosphere.

6.4. Photophysical properties

The photophysical properties of **I**–**K** suggested that a COPV unit mainly concerns into the photoexcitation and emission. Absorption spectra exhibited maximum absorption peaks at 402–411 nm, attributed to π–π* transition of the COPV unit.[21] The corresponding fluorescence peaks were observed at 445–461 nm (Table 6.2, Figure 6.6). Comparing to **A,** both of the spectra for **I**–**K** are red-shifted because of the extended conjugation system and electron donation from the diarylamino substituents. Compound **J** showed its absorption and fluorescence in shorter wavelength region, while **I** and **K** show absorption and fluorescence in very similar wavelength. This result indicates the enlargement of optical bandgap due to the decrease of HOMO by the resonance effect. The relatively high fluorescence quantum yields (Φ_{FL} = 0.42–0.59, Table 6.2) and similar nonradiative rate constants (k_{nr} = 1.47–1.74 × 10^8 s^{-1}), where heavy atom effect of sulfur atom in **K** is negligible, indicate photoexcitation properties of **I**–**K** mainly attributed to the all-carbon backbone.

Table 6.2. Photophysical properties of **I**–**K**.

	λ_{abs} [a] (nm)	λ_{FL} [b] (nm)	Φ_{PL} [c]	τ [d] (10^{-9} s^{-1})	k_r [e] (10^8 s^{-1})	k_{nr} [f] (10^8 s^{-1})
I	305, 411	461	0.590	2.80	2.11	1.47
J	312, 402	445	0.420	3.54	1.19	1.64
K	327, 411	460	0.525	2.73	1.93	1.74

[a] Absorption maximum wavelengths measured in dichloromethane. [b] Fluorescence maximum wavelengths measured in dichloromethane. [c] Fluorescence quantum yield determined using the absolute method. [d] Fluorescence lifetime measured with the time-correlated single-photon counting operation mode. [e] Radiative rate constant. [f] Nonradiative rate constant.

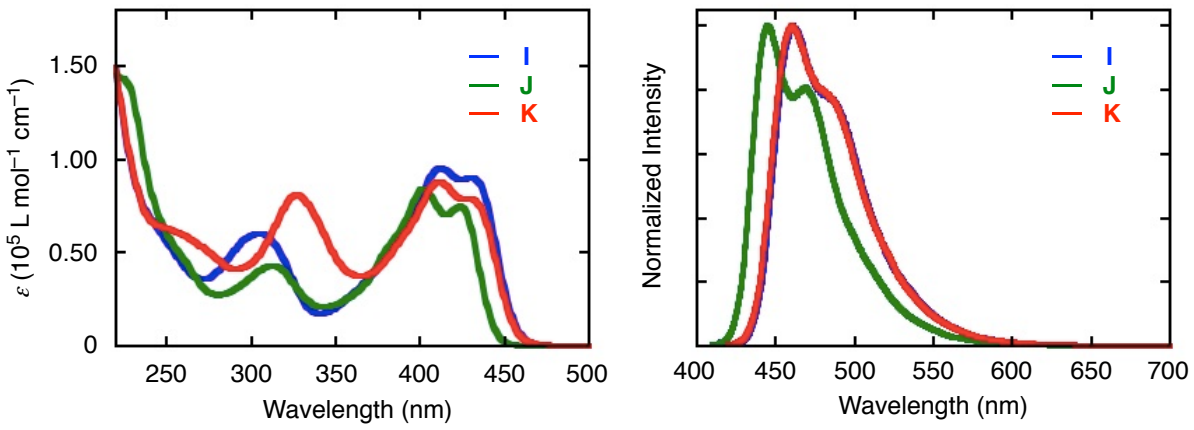

Figure 6.6. Absorption and fluorescence spectra of **I**–**K** in THF (1.0×10^{-5} M for absorption and 1.0×10^{-6} M for fluorescence).

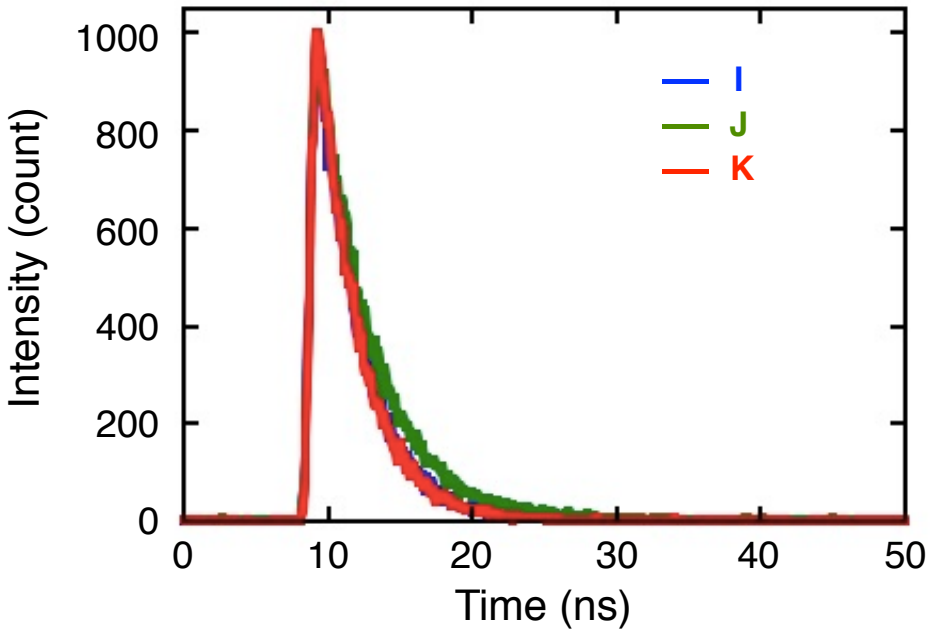

Figure 6.7. Fluorescence lifetime of **I**–**K** in THF (1.0×10^{-6} M).

6.5. Electrochemical properties

An electrochemical study provided evidence of strong electronic interaction between the two spiro-linked π-planar units in the radical cation. DPV measurement of **I** (Figure 6.8, blue line) showed the first peak at 0.03 V vs Fc/Fc^+ by single-electron oxidation of a COPV1 unit, followed by the second two-electron oxidation peak at 0.19 V vs Fc/Fc^+. Considering that the oxidation peaks of bis(diarylamino) COPV1[26] as a referential compound are reported as –0.05/0.17 V vs Fc/Fc^+ (Figure 6.8, grey line), the overlap of the second and the third oxidation peaks of **I** strongly indicates the spiro-conjugation in the radical cation form. In the other words, it is suggested that the first oxidation of a COPV unit becomes much more difficult once the other COPV unit get oxidized at the first oxidation peak, and the dication delocalizes over whole the structure through spiroconjugation, as seen in similar homo-conjugated tetraamino compounds.[21] The same effect in radical cation is observed in the DPV curves of **J** and **K** (Figure 6.8, green and red). The potential of the first oxidation peak becomes higher in the order of **K** > **J** > **I**. This result suggests the HOMO level is effectively lowered by the positional effect in **J** and weaker electron donation of methylthio group in **K**.

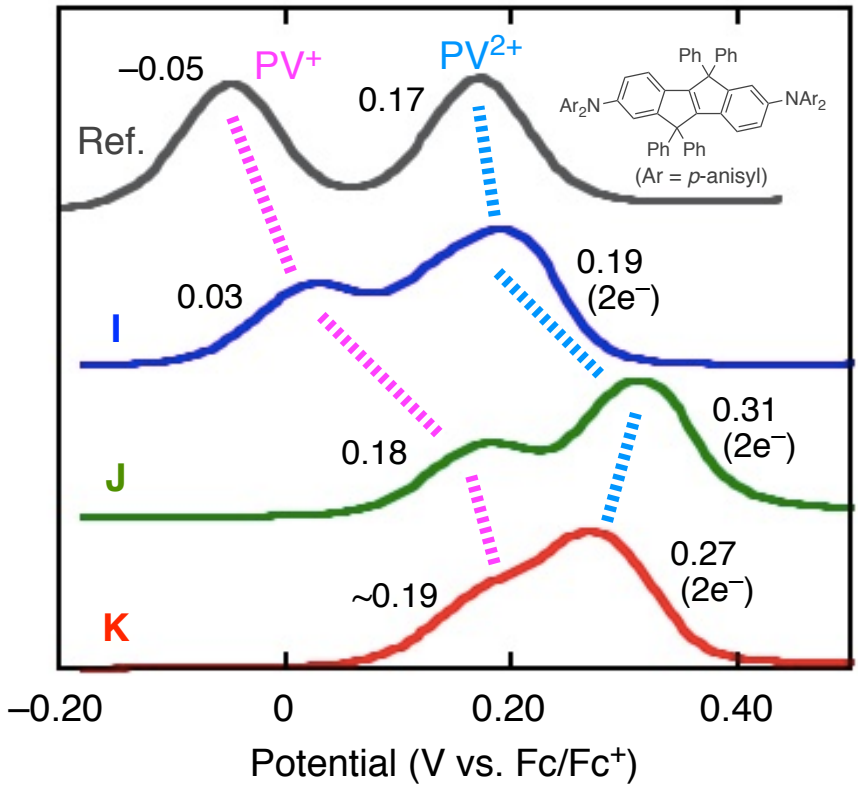

Figure 6.8. DPV curves of **I**–**K** and bis(diarylamino) COPV1 in THF (0.5 mM solution with 0.1 M Bu_4NPF_6 electrolyte).

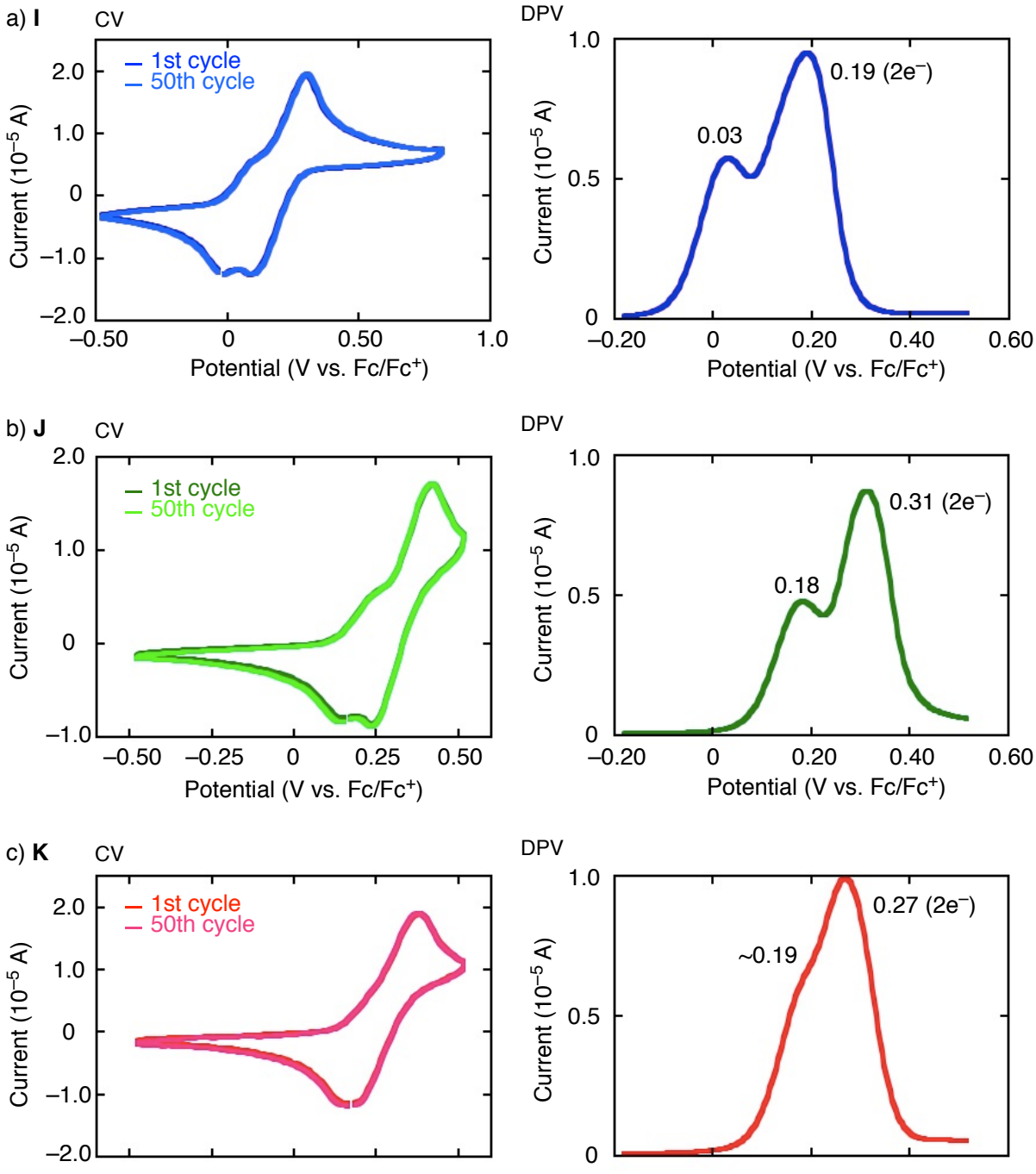

Figure 6.9. Cyclic voltammograms and differential pulse voltammograms of **H**–**J** in THF (0.5 mM solution with 0.1 M Bu_4NPF_6 electrolyte).

6.6. Properties of radical cation

In order to understand the oxidation processes of **I**–**K**, I conducted absorption titration of the compounds on chemical oxidation (Scheme 6.2). Solutions of **I**–**K** in chlorobenzene were titrated with $NOPF_6$ in acetonitrile under monitoring of absorption spectra (Figure 6.10). Addition of up to 1.0 equiv of $NOPF_6$ to a solution of **I** resulted in appearance of new absorption peaks at 620 and 1591 nm, and decrease of the original peak at 411 nm of the neutral compound (Figure 6.10a, left, red line). Comparing this to the absorption spectra of COPV1 cation[27] and its diarylamino derivative,[26] the new peaks at 620 and 1591 nm were assigned to SOMO–LUMO and HOMO–SOMO electron transitions of a radical-cationic COPV unit (PV^+ in Figure 6.10) in $\mathbf{I}^+$, respectively. Further addition of $NOPF_6$ decreased the peaks at 620 and 1591 nm with the generation of a new peak at 941 nm, suggesting the formation a dicationic COPV1 moiety (PV^{2+}) from a radical-cationic COPV unit. (Figure 6.10a, right). Importantly, the peak derived from a dicationic COPV unit is already observed with 2.0 equiv of oxidant. It suggests the first oxidation of a neutral COPV unit of $\mathbf{I}^+$ and the formation of a dicationic COPV unit take place simultaneously. These results support the strong electronic interaction between the two COPV units upon single electron oxidation, as well as the electrochemical properties discussed in section 6.5. The similar results are observed in compound **J** and **K** to indicate the formation of radical cationic COPV units by oxidation (Figure 6.10b, c right). However, the peak intensity for a dicationic COPV is much less in **K** or does not appeared in **J**. It should be because the much higher second two-election oxidation potentials of **K** (0.27 eV) and **J** (0.31 eV) than that of **I** (0.19 eV), observed in DPV (Figure 6.8).

Scheme 6.2. Oxidation process of tetrakis(diarylamino) spiro-CPV.

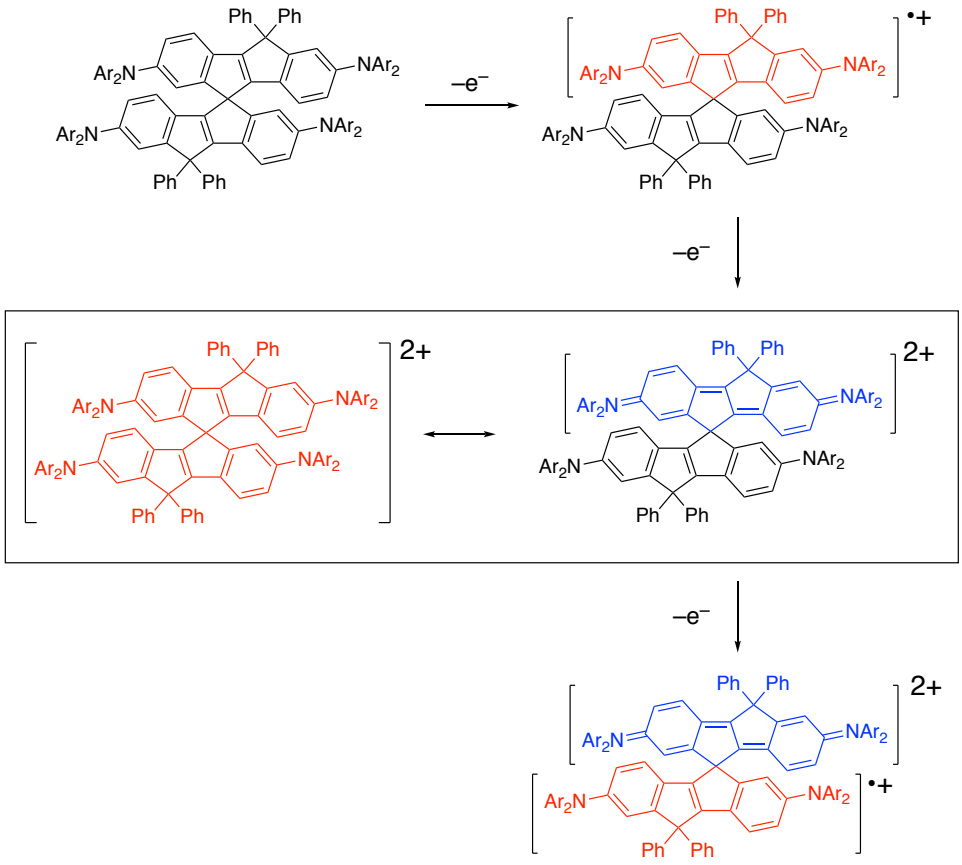

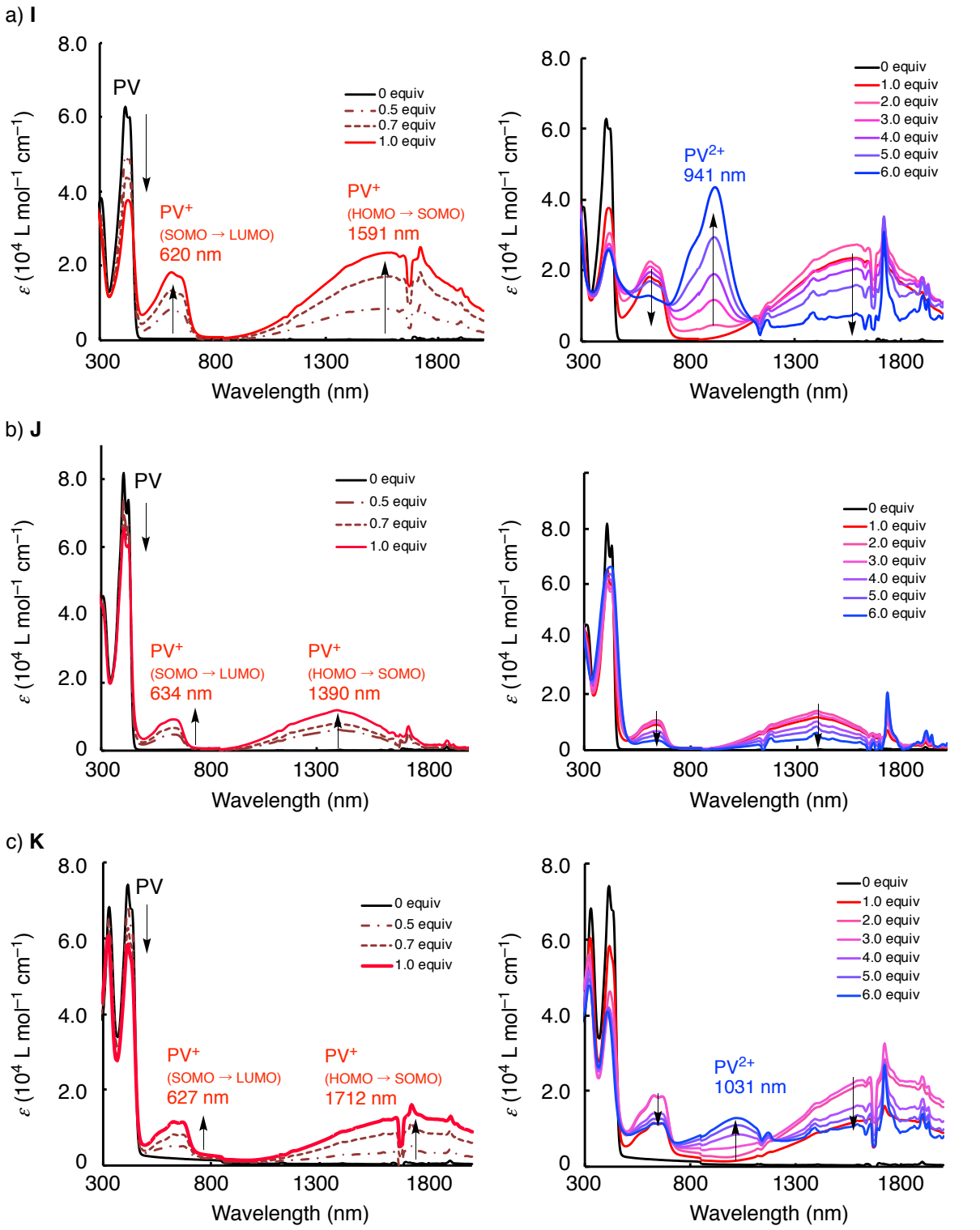

Figure 6.10. Absorption titration experiments of **I**–**K** in chlorobenzene upon addition of $NOPF_6$ solution in acetonitrile: (left) up to 1.0 equiv and (right) up to 6.0 equiv.

Electron spin resonance (ESR) measurement was also conducted. Radical-cationic **I**–**K** (Figure 6.11) showed a single ESR peak without hyperfine structure with a g value of 2.00298, 2.00292, and 2.00327, respectively, indicating that the spin is mainly located on spiro-CPV moiety.

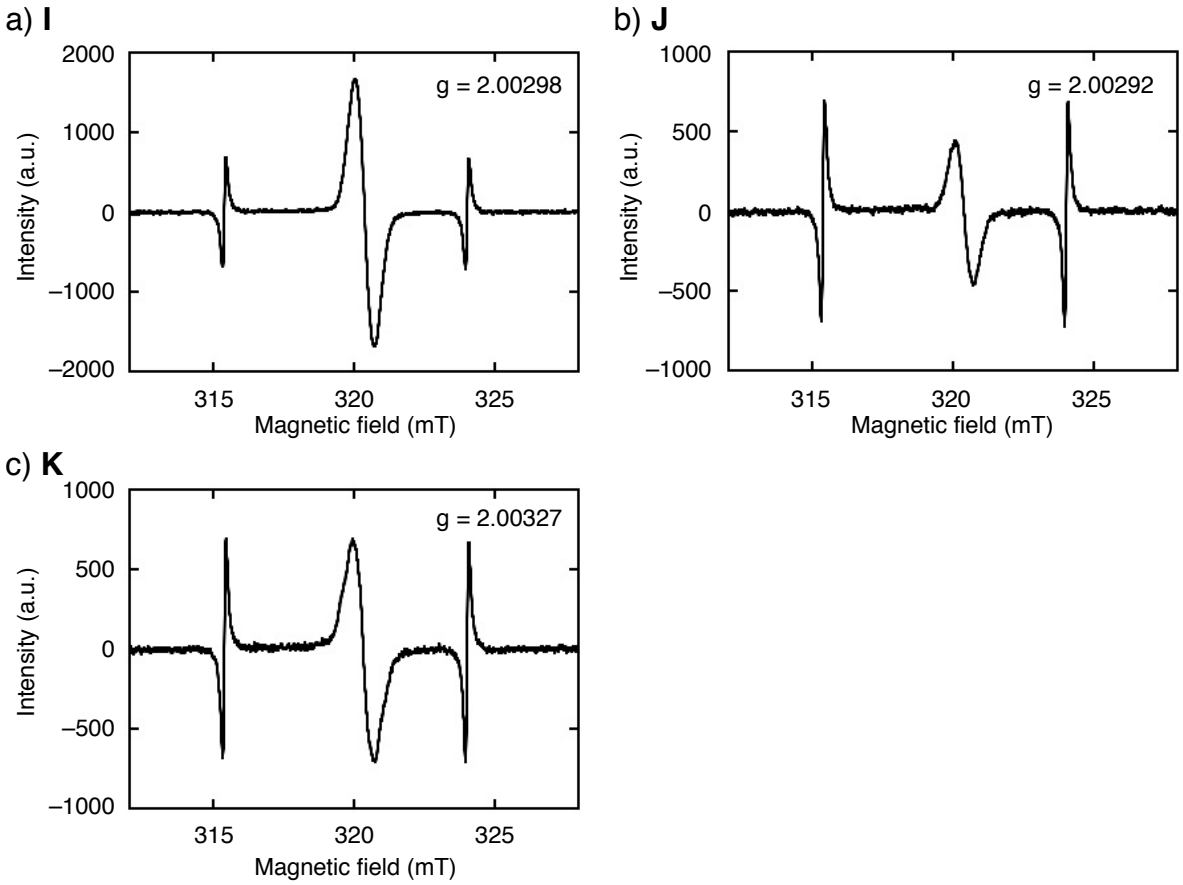

Figure 6.11. ESR spectra of radical-cationic **I**–**K** in chlorobenzene doped by 1.0 equiv of $NOPF_6$ in acetonitrile.

6.7. Semiconducting properties

The ionization potentials and optical bandgaps of **I**–**K** determined by PYS and absorption, indicated the spiro-CPV-based HTMs have suitable energy levels for the applications in organic electronic applications (Table 6.3, Figure 6.12). Especially for PVSC application, compound **J** and **K**, compared to spiro-OMeTAD, show a comparable or better energy level alignment with perovskite layer thanks to their lowered HOMO levels.

Table 6.3. Ionization potentials and electron affinities of **I**–**K** films spin-coated on ITO surface.

	IP[a] (eV)	Absorption offset (nm)	OBG[b] (eV)	EA[c] (eV)
I	4.83	462	2.68	2.15
J	5.18	447	2.77	2.41
K	5.35	459	2.70	2.65

[a] Ionization potential. [b] Optical bandgap. [c] Electron affinity determined from IP and OBG.

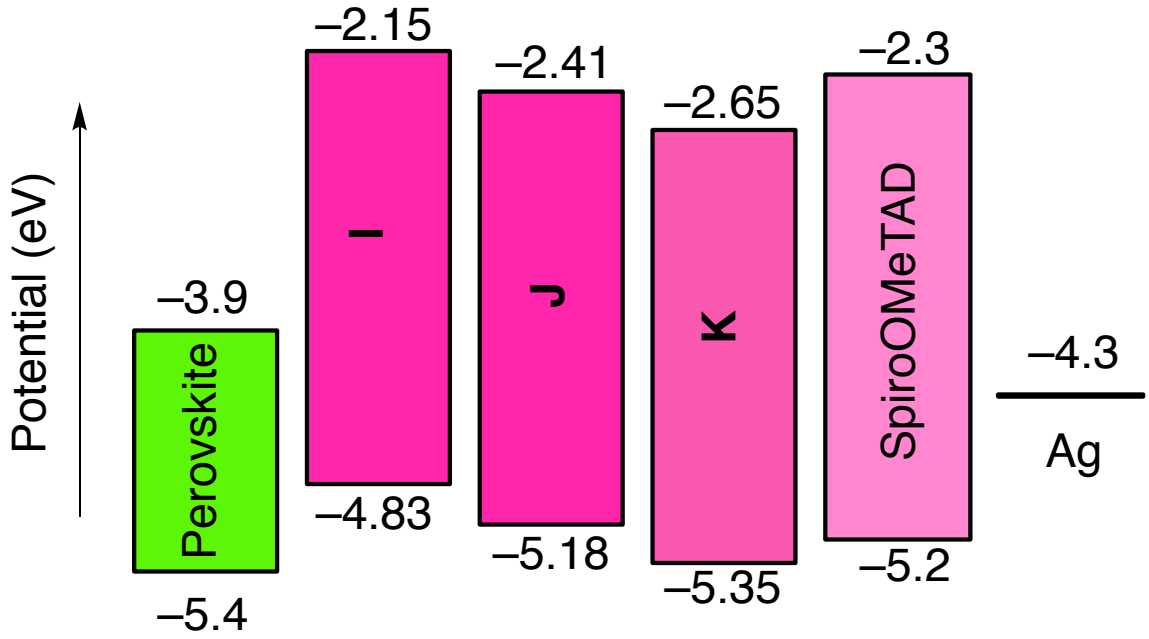

Figure 6.12. Energy level diagram of **I**–**K**, spiro-OMeTAD, and the components of perovskite solar cell.

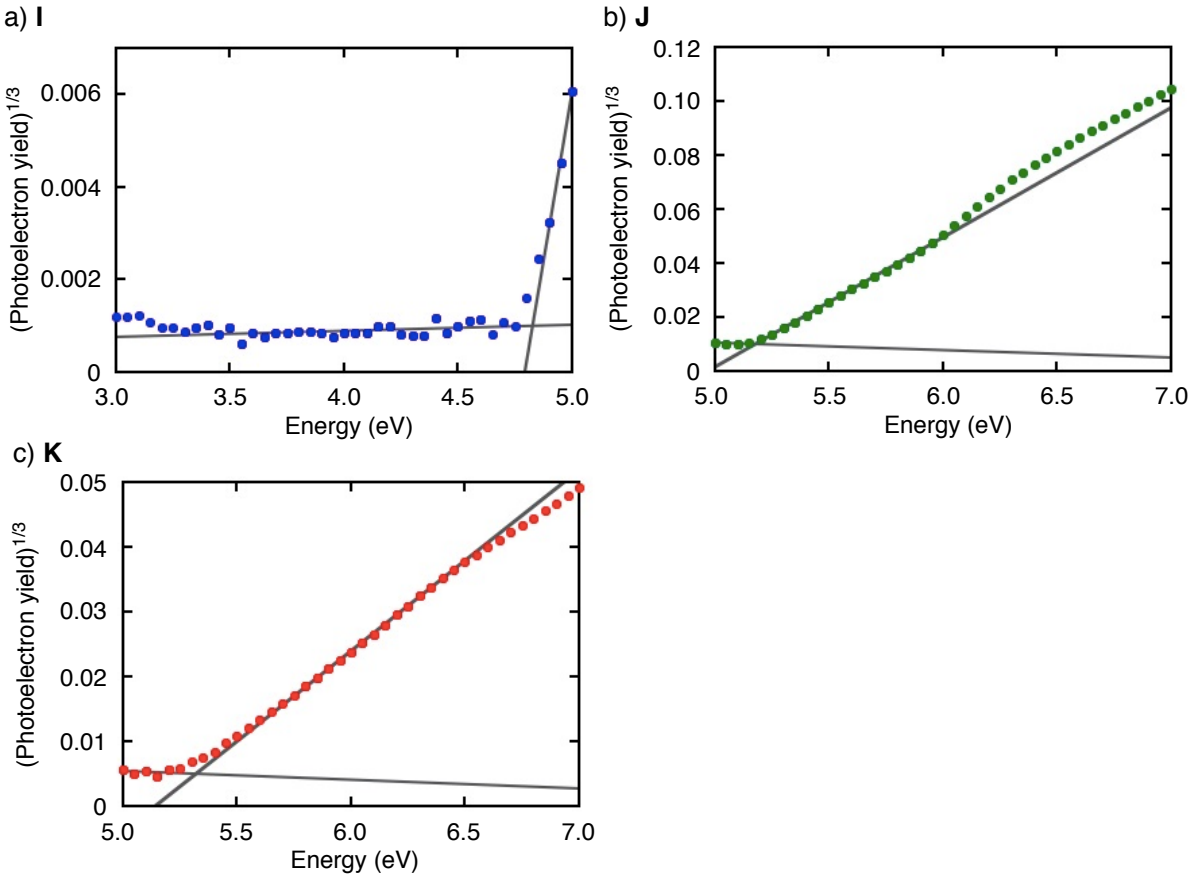

Figure 6.13. PYS data of **I**–**K** films spin-coated on ITO surface.

The hole mobility μ_h of spin-coated films of **I**–**K** were determined by using the space charge limited current (SCLC) method with a device structure of ITO/PEDOT:PSS/HTM/MoO_3/Ag (Figure 6.14). Compound **I** and **J** showed comparable μ_h of 2.74–3.84 × 10^{-5} cm^2 V^{-1} s^{-1} than spiro-OMeTAD[21] (μ_h = 2.6 × 10^{-5} cm^2 V^{-1} s^{-1} with a device structure of ITO/PEDOT:PSS/spiro-OMeTAD/Au), while **K** shows low μ_h of 2.74 × 10^{-6} cm^2 V^{-1} s^{-1}. Noteworthily, the oxidant doping with LiTFSI and TBP increases the hole mobilities of **I**–**K** to 1.12–2.67 × 10^{-4} cm^2 V^{-1} s^{-1}. This enhancement of μ_h suggests that hole transport becomes more efficient upon oxidation to generate radical cation species, where the charge delocalizes over the whole structure via spiroconjugation as suggested in the DPV and absorption titration studies. The three-dimensional charge delocalization decreases reorganization energy, important for effective charge transport,[12,13] as observed in fullerene electron acceptor materials.[14,28]

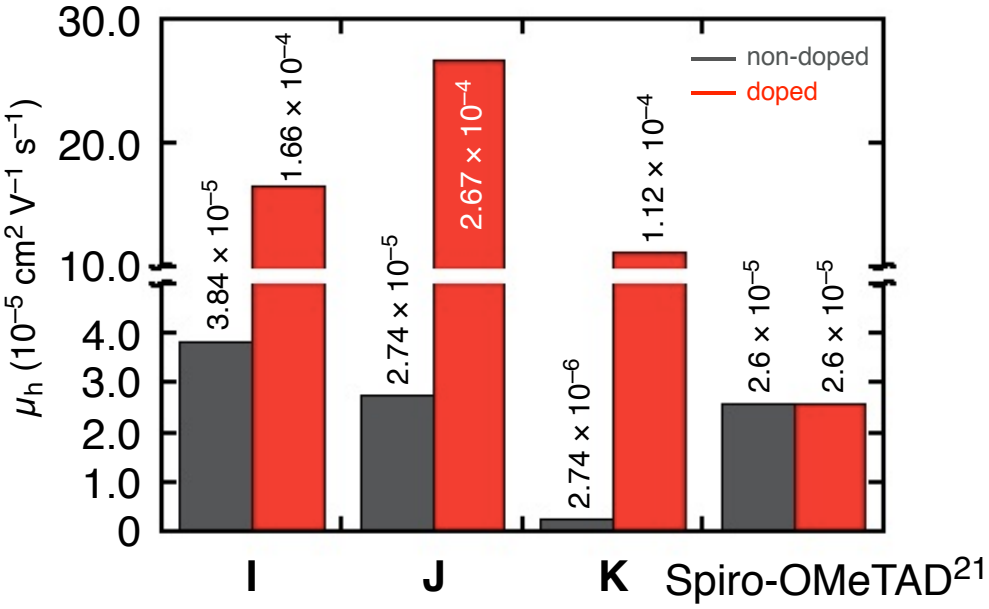

Figure 6.14. Hole mobilities of spin-coated **I**–**K** films without and with LiTFSI dopant measured by SCLC method.

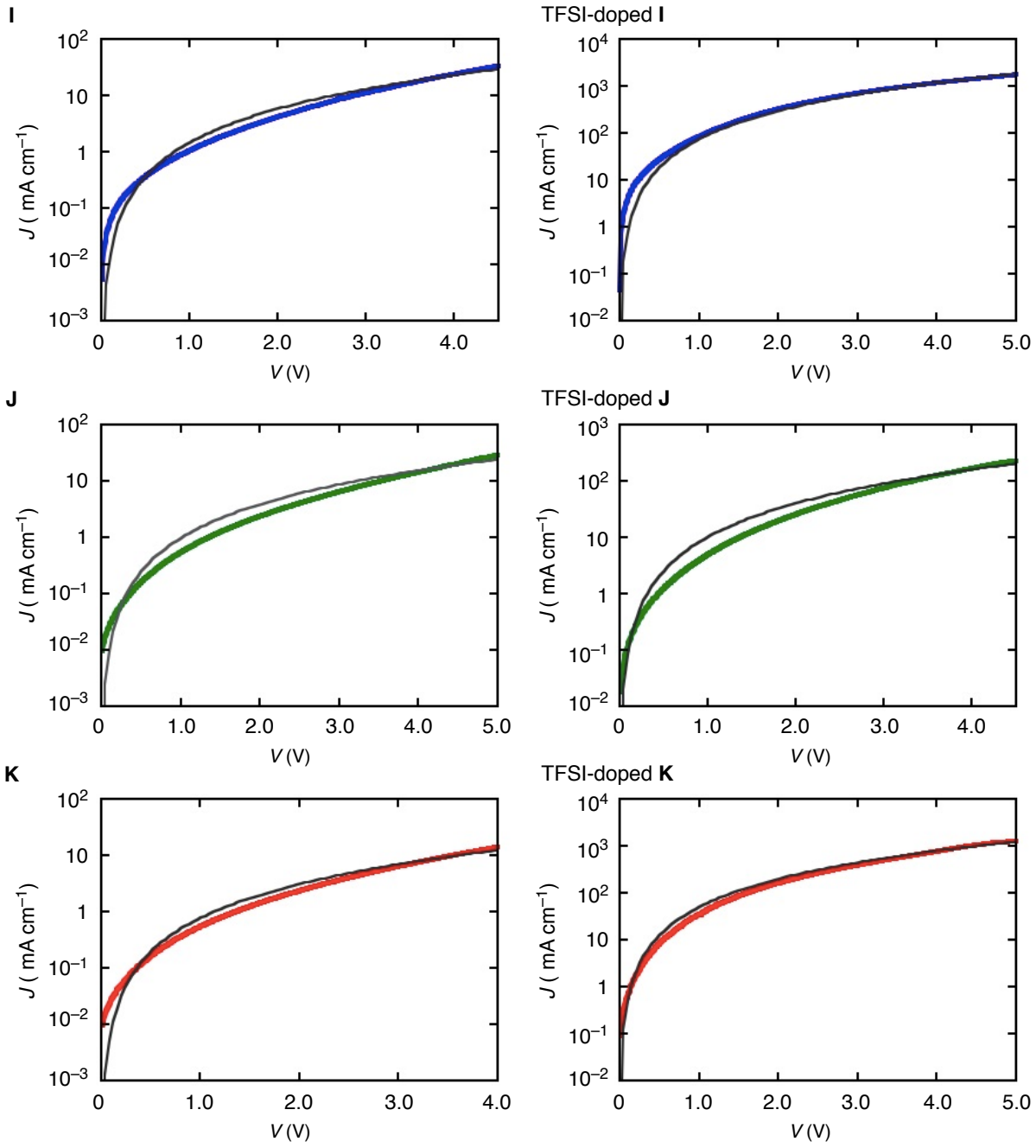

Figure 6.15. *J-V* curves of hole-only transporting devices with spin-coated **I**–**K** films. Non-doped (left) and TFSI-doped (right). Grey lines show fitting curves.

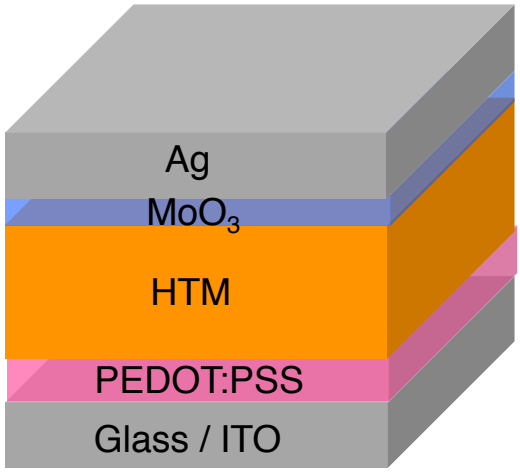

Figure 6.16. Schematic image of the device structure for SCLC measurement.

Finally, PVSCs were fabricated in order to demonstrate the usage of the HTMs in practical devices (Table 6.4). The use of TFSI-doped **I** as a HTM with a device structure of FTO/TiO_x/$MAPbI_{3-x}Cl_x$/HTM/Au afforded a PCE of 12.9%. This value was higher than that of the corresponding spiro-OMeTAD based device (PCE = 12.2%).[21] PVSC with HTM **I** in another condition (ITO/SnO_2/$FA_{0.9}Cs_{0.1}PbI_{2.7}Br_{0.3}$/HTM/Ag) gave a PCE of 14.1%. These results suggest the utility of spiro-CPV-based HTM in solar cell application.

Table 6.4. Device performances of PVSCs with **I** and spiro-OMeTAD as HTMs.

HTM	Device structure	V_{OC} (V)	J_{SC} (mA/cm^2)	FF	PCE (%)
Spiro-OMeTAD[21]	a)	0.98	18.4	0.68	12.2
I	a)	1.04	19.4	0.64	12.9
I	b)	0.96	21.7	0.68	14.1

Device structure: a) FTO/TiO_x/$MAPbI_{3-x}Cl_x$/HTM/Au and b) ITO/SnO_2/$FA_{0.9}Cs_{0.1}PbI_{2.7}Br_{0.3}$/HTM/Ag.

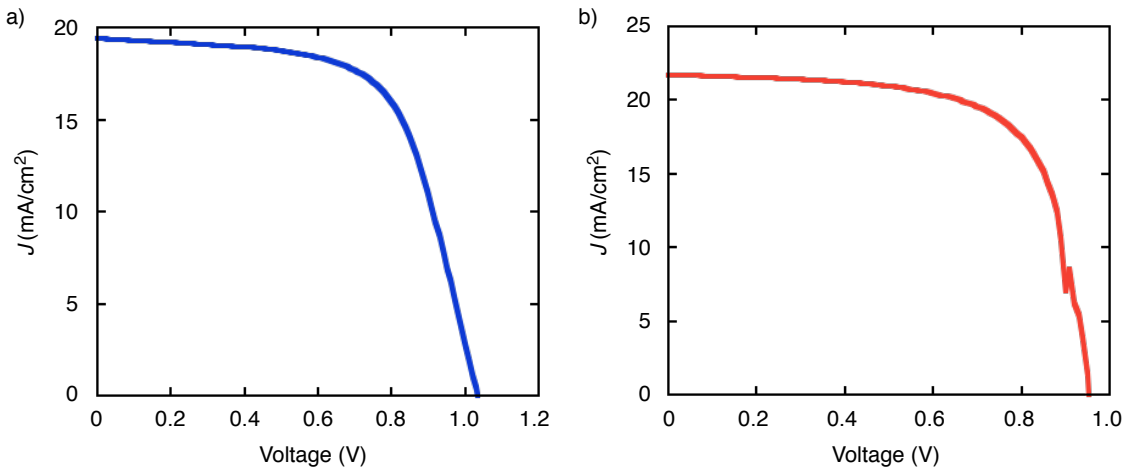

Figure 6.17. *J-V* characteristics of PVSCs with **I** as an HTM. Device structures are a) FTO/TiO_x/$MAPbI_{3-x}Cl_x$/HTM/Au and b) ITO/SnO_2/$FA_{0.9}Cs_{0.1}PbI_{2.7}Br_{0.3}$/HTM/Ag.

6.8. Summary

In summary, spiro-CPV-based HTMs are developed by attaching diarylamine substituents on spiro-COPV backbone. The novel HTMs are found to have higher phase stability in amorphous state and better hole transporting properties than those of spiro-OMeTAD, the common HTM. The HOMO energy levels could be finely tuned by the choice of aryl substituents. Their radical cationic states show efficient inter-subunit electronic interactions, which cause the enhancement of μ_h upon oxidant doping in their spin-coated films. These investigations demonstrated the performance of spiro-CPV as a semiconducting material backbone.

6.9. Experimental section

6.9.1. Synthesis

General consideration

All the reactions dealing with air- or moisture-sensitive compounds were carried out in a dry reaction vessel under a positive pressure of N_2 or Ar gas. Air- and moisture-sensitive liquids and solutions were transferred via syringe or Teflon cannula. Analytical thin-layer chromatography (TLC) was performed using glass plates pre-coated with 0.25 mm, 230–400 mesh silica gel impregnated with a fluorescent indicator (254 nm). Thin-layer chromatography plates were visualized by exposure to ultraviolet light (UV). Organic solutions were concentrated by rotary evaporation at ca. 15 Torr (evacuated with a diaphragm pump). Flash column chromatography was performed as described by Still *et al*.[29], employing Kanto Silica gel 60 (spherical, neutral, 140–325 mesh).

Unless otherwise noted, commercial reagents were purchased from Tokyo Kasei Co., Aldrich Inc., and other commercial suppliers and used as purchased. Anhydrous solvents were purchased from Kanto, and purified by a solvent purification system (GlassContour) equipped with columns of activated alumina and copper catalyst prior to use.

NMR spectra were recorded using a JEOL ECZ-500 (^{1}H NMR, 500 MHz; ^{13}C NMR, 125 MHz) NMR spectrometer. Chemical data for protons are reported in parts per million (ppm, δ scale) downfield from tetramethylsilane and are referenced to the residual protons in the NMR solvent (CD_2Cl_2: δ 5.32). Chemical data for carbons are reported in parts per million (ppm, δ scale) downfield from tetramethylsilane and are referenced to the carbon resonance of the solvent (CD_2Cl_2: δ 54.0). The data are presented as follows: chemical shift, multiplicity (s = singlet, d = doublet, t = triplet, m = multiplet and/or multiple resonances, br = broad), coupling constant in Hertz (Hz), and integration. Melting points of solid materials were determined on a Mel-Temp II capillary melting-point apparatus and are uncorrected. Mass spectra were obtained on JEOL AccuTOF JMS-T100LC (APCI) mass spectrometer. High-resolution mass spectra were obtained with a calibration standard of reserpine.

Synthetic procedures

General procedure of Buchwald-Hartwig amination of **20**.

2,2'-7,7'-Tetrakis(di-*p*-anisyl)amino-spiro-CPV (**I**)

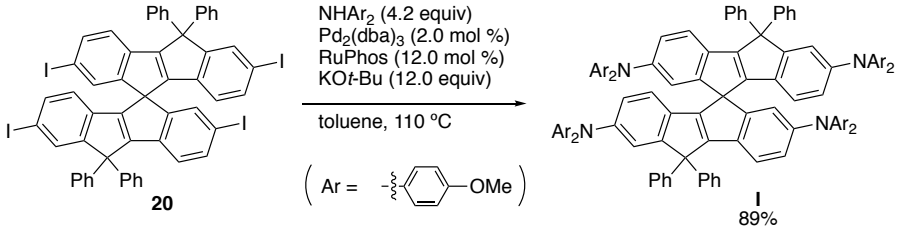

4,4'-Dimethoxydiphenylamine (160 mg, 0.698 mmol), $Pd_2(dba)_3$ (3.05 mg, 3.3 μmol), RuPhos (3.11 mg, 6.7 μmol), potassium *tert*-butoxide (224 mg, 2.00 mmol), and **20** (200 mg, 0.167 mmol) were dissolved in toluene (5.0 mL) and stirred for 15 h at 110 ºC. The reaction mixture was allowed to cool gradually down to ambient temperature and then was added water. The organic layer was extracted with dichloromethane, dried over anhydrous Na_2SO_4, and evaporated *in vacuo*. The crude mixture was purified by column chromatography (eluent: EtOAc/hexane = 1/3) and reprecipitation (CH_2Cl_2/hexane) to afford compound **I** (239 mg, 89%) as a yellow solid. Mp: 171 ºC (T_g from DSC data); ^{1}H NMR (500 MHz, CD_2Cl_2) δ 3.71 (s, 12H), 3.76 (s, 12H), 6.29 (d, J = 8.0 Hz, 2H), 6.54–6.62 (m, 6H), 6.67 (td, J = 6.3, 3.8 Hz, 8H), 6.75 (td, J = 6.2, 3.8 Hz, 8H), 6.82 (td, J = 6.2, 4.0 Hz, 8H), 6.88 (d, J = 8.0 Hz, 2H), 6.91–7.03 (m, 16H), 7.09 (d, J = 2.3 Hz, 2H), 7.10–7.16 (m, 2H), 7.21–7.28 (m, 6H), 7.30–7.36 (m, 4H); ^{13}C NMR (125 MHz, CD_2Cl_2) δ 55.67, 55.74, 63.9, 114.7, 114.8, 117.7, 118.9, 119.5, 119.9, 120.3, 120.8, 125.9, 126.3, 126.9, 127.2, 128.5, 128.6, 128.8, 131.5, 134.1, 141.4, 143.5, 143.6, 146.8, 147.0, 148.3, 151.0, 155.8, 156.1, 157.4, 158.5; HRMS (APCI+) calcd for $C_{111}H_{88}N_4O_8$ (M): 1604.6602; found: 1604.6610.

2,2'-7,7'-Tetrakis(di-*m*-anisyl)amino-spiro-CPV (**J**)

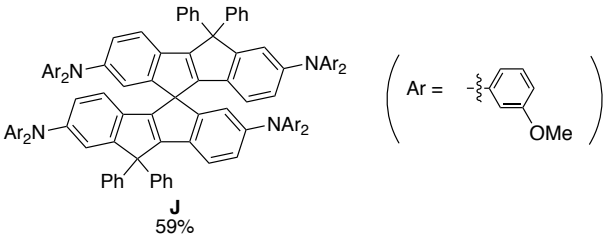

476 mg, 59% as a yellow solid. Mp: 134 ºC (T_g from DSC data); ^{1}H NMR (500 MHz, CD_2Cl_2) δ 3.52 (s, 12H), 3.60 (s, 12H), 6.33 (d, J = 8.0 Hz, 2H), 6.46 (dd, J = 8.0, 1.1 Hz, 4H) 6.48–6.61 (m, 22H), 6.70

(dd, J = 8.3, 2.0 Hz, 4H), 6.75 (d, J = 2.3 Hz, 2H), 6.97 (d, J = 8.0 Hz, 2H), 6.99–7.12 (m, 16H), 7.15 (tt, J = 7.3, 1.4 Hz, 2H), 7.20 (d, J = 2.3 Hz, 2H), 7.23–7.27 (m, 4H), 7.32–7.37 (m, 4H); ^{13}C NMR (125 MHz, CD_2Cl_2) δ 55.4, 55.5, 64.0, 77.7, 108.8, 108.9, 110.0, 110.2, 117.0, 117.1, 119.4, 119.6, 120.7, 121.2, 122.6, 123.2, 125.2, 127.0, 127.3, 128.4, 128.69, 128.75, 129.98, 130.02, 135.3, 143.1, 143.2, 145.7, 145.9 148.9, 149.1, 158.4, 160.7, 160.8; HRMS (APCI+) calcd for $C_{111}H_{88}N_4O_8$ (M): 1604.6602; found: 1604.6656.

2,2'-7,7'-Tetrakis(di-*p*-thioanisyl)amino-spiro-CPV (**K**)

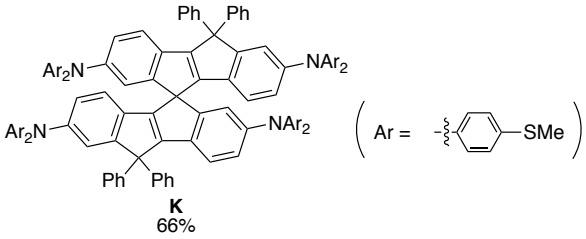

K
66%

124 mg, 66% as a yellow solid. Mp: 176 ºC (T_g from DSC data); ^{1}H NMR (500 MHz, CD_2Cl_2) δ 2.40 (s, 12H), 2.44 (s, 12H), 6.39 (d, J = 8.0 Hz, 2H), 6.68 (d, J = 2.3 Hz, 2H), 6.71 (dd, J = 8.0, 2.3 Hz, 2H), 6.74 (dd, J = 8.0, 2.3 Hz, 2H), 6.84 (dt, J = 9.4, 2.3 Hz, 8H), 6.95 (d, J = 9.4, 2.4 Hz, 8H), 6.98–7.05 (m, 16H), 7.09–7.16 (m, 12H), 7.20 (d, J = 2.3 Hz, 2H), 7.24–7.30 (m, 6H), 7.34–7.38 (m, 4H); ^{13}C NMR (125 MHz, CD_2Cl_2) δ 16.5, 16.5, 59.2, 63.7, 119.3, 119.5, 120.6, 120.7, 122.1, 123.2, 124.2, 124.6, 126.8, 127.1, 128.0, 128.1, 128.2, 128.4, 128.5, 131.7, 132.1, 132.5, 135.2, 142.6, 142.9, 145.0, 145.3, 145.6, 148.2, 150.5; HRMS (APCI+) calcd for $C_{111}H_{88}N_4S_8$ (M+H): 1733.4853; found: 1733.4934.

6.9.2. Characterization

Photophysical properties

UV-Vis absorption spectra were measured with a JASCO V-670 spectrometer. Fluorescence spectra were measured with a HITACHI F-4500 spectrometer. Photoluminescence quantum yields were measured on Hamamatsu Photonics C9920–02 Absolute PL Quantum Yield Measurement System, and absolute quantum yields were determined by using a calibrated integrating sphere system. Fluorescence lifetimes were measured on Hamamatsu Photonics C11367-02 Quantaurus-Tau. CD spectra were measured on a JASCO J-1500 spectropolarimeter. CPL spectra were measured on a JASCO CPL-200 spectrometer. Optical rotations were measured on a JASCO P-1030 polarimeter using a 50-mm cell. The absorption maximum wavelengths were used as

excitation wavelengths. Spectral grade solvents (THF, chlorobenzene) were used as solvents for UV-Vis absorption fluorescence, CD, CPL, and optical rotation measurements.

Electrochemical properties

CV and DPV were conducted with HOKUTO DENKO HZ-7000 voltammetric analyzer. Measurements were carried out in a one-compartment cell under argon gas, equipped with a platinum counter electrode, a glassy-carbon working electrode, and an Ag/Ag^+ reference electrode. The supporting electrolyte was a 0.5 M dichloromethane solution of tetrabutylammonium hexafluorophosphate. All potentials were collected against Fc/Fc^+.

Ionization potential

PYS measurement was performed with PYS-201 (Sumitomo Heavy Industries, Ltd).

Thermal stabilities

TGA was performed on a Rigaku ThermoPlus 2 thermal analyzer (TG 8120). Sample was placed in an aluminum pan and heated to 500 ºC at the rate of 10 K/min under N_2 purge at a flow rate of 10 mL/min. Al_2O_3 was used as reference material. DSC was performed on a SII Nanotechnology (DSC6220) instrument. Samples were placed in aluminum pans and heated at 10 K/min, under N_2 gas at a flow rate of 50 mL/min.

Hole mobility

The hole mobilities were measured by the space charge limited current (SCLC) method with a device configuration of ITO/PEDOT:PSS/HTL/MoO_3/Ag. A solution of TFSI-doped **H**–**J** were prepared by mixing **H**–**J** (60 mg/mL, 1.0 mL) in chlorobenzene and dopant (15 µL, 520 mg/mL LiTFSI in acetonitrile and 22.5 µL 2,6-di-*tert*-butylpyridine), respectively. ITO glasses (Techno Print Co., Ltd., Japan) were used as a substrate. The patterned ITO glass was treated by UV-ozone irradiation for 5 min. A thin PEDOT:PSS layer was prepared on the ITO surface by spin-coating at 500 rpm for 3 sec, and 3000 rpm for 30 sec. The substrate was annealed at 120 ºC for 30 min under ambient conditions. A solution of HTM (60 mg/mL in chlorobenzene) or TFSI-doped HTM was spin-coated on the PEDOT:PSS layer at 500 rpm for 3 sec, and then at 2000 rpm for 60 sec. The resulting substrate was

heated at 120 ºC for 15 min under ambient conditions. MoO_3 layer and Ag as a counter electrode were deposited on the HTL by vacuum evaporation. *J-V* characteristics of the devices were measured on a Keithley 2400 source measurement unit. The SLCL is described as the following:[30]

$$J_{\mathrm{SCLC}} = \frac{9}{8}\mu_{\mathrm{SCLC}}\varepsilon_0\varepsilon_r\frac{V^2}{d^3}$$

J_{SCLC}: the steady-state current density.

V: the applied voltage.

d: the film thickness.

μ_{SCLC}: the carrier mobility.

ε_r: the dielectric constant assumed to be 3, a typical value for organic HTMs.

$\varepsilon_{\square}$: the permittivity of the free space.

Electron spin resonance (ESR) spectrum

ESR spectra were recorded using a JEOL JES-FA200 ESR spectrometer with a Mn marker as a reference.

Device fabrication for perovskite solar cells

For a device structure of FTO/TiO_x/$MAPbI_{3-x}Cl_x$/HTM/Au, a fluorine-doped tin oxide (FTO) layer on a glass substrate was used for this study. Prior to the formation of the buffer layer, the patterned FTO glass was ultrasonically cleaned using a surfactant, rinsed with water and then finally given 3 min UV−ozone treatment. A 45 nm thick electron-transporting layer of TiO_x was deposited by spin-coating (3000 rpm for 30 s) of the precursor solution and annealed at 500 °C for 30 min in air atmosphere. To form the $MAPI_{3-x}Cl_x$ layer, a 40wt% precursor solution (4:1:1 mol ratio of MAI:PbI_2:$PbCl_2$) in DMF was spin-coated onto the TiO_x layer at 500rpm for 3s and 4000rpm for 30 s. Further, it was annealed at 100 °C for 35 min in a N_2- filled glovebox. The HTM (60 mg/mL) in chlorobenzene with dopants (15 μL, 520 mg/mL LiTFSI in CH_3CN and 22.5 μL 2,6-di-*tert*-butylpyridine) was then deposited by spin-coating (2200 rpm for 30 s). The top electrode (Au, 80 nm) was deposited through a metal shadow mask, which defined a 2 mm stripe pattern perpendicular to the ITO stripe.

For a device structure of ITO/SnO_2/$FA_{0.9}Cs_{0.1}PbI_{2.7}Br_{0.3}$/HTM/Ag, $FA_{0.9}Cs_{0.1}PbI_{2.7}Br_{0.3}$ layer

was formed from a 40 wt% precursor solution (9:9:1.5:1 mol ratio of FAI:PbI_2:$PbBr_2$:CsI) in DMF spin-coated onto SnO_2 layer on ITO substrate at 100 rpm for 10s and 6000 rpm for 30s. Further, it was annealed at 100 °C for 60 min in a N_2- filled glovebox. The HTM (60 mg/mL) in chlorobenzene with dopants (15 μL, 520 mg/mL LiTFSI in CH_3CN and 22.5 μL 2,6-di-*tert*-butylpyridine) was then deposited by spin-coating (2200 rpm for 30 s). The top electrode (Ag, 100 nm) was deposited through a metal shadow mask, which defined a 1 mm stripe pattern perpendicular to the ITO stripe.

6.10. References

[1] Tang, C. W. *Appl. Phys. Lett.* **1986**, *48*, 183–185.

[2] Koezuka, H.; Tsumura, A.; Ando, T. *Synth. Met.* **1987**, *18*, 699–704.

[3] Tan, C. W.; VanSlyke, S. A. *Appl. Phys. Lett.* **1987**, *51*, 913–915.

[4] Kojima, A.; Teshima, K.; Shirai, Y.; Miyasaka, T. *J. Am. Chem. Soc.* **2009**, *131*, 6050–6051.

[5] Jena, A. K.; Kulkarni, A.; Miyasaka, T. *Chem. Rev.* **2019**, *119*, 3036–3103.

[6] Hoefler, S. F.; Trimmel, G.; Rath, T. *Monatsh. Chem.* **2017**, *148*, 795–826.

[7] Saragi, T. P. I.; Spehr, T.; Siebert, A.; Fuhrmann-Lieker, T.; Salbeck, J. *Chem. Rev.* **2007**, *107*, 1011–1065.

[8] Pfeiffer, M.; Leo, K.; Zhou, X.; Huang, J. S.; Hofmann, M.; Werner, A.; Blochwits-Nimoth, J. *Org. Electron,* **2003**, *4*, 89–103.

[9] Saragi, T. P. I.; Fuhrmann-Lieker, T.; Selbeck, J. *Adv. Funct. Mater.* **2006**, *16*, 966–974.

[10] Saragi, T. P. I.; Pudzich, R.; Fuhrmann-Lieker, T.; Salbeck, J. *Appl. Phys. Lett.* **2004**, *84*, 2334–2336.

[11] Urieta-Mora, J.; García-Benito, I.; Molina-Ontoria, A.; Martín, N. *Chem. Soc. Rev.* **2018**, *47*, 8505–8970.

[12] (a) Marcus, R. A. *J. Chem. Phys.* **1957**, *26*, 867– 871. (b) Marcus, R. A. *J. Phys. Chem.* **1968**, *72*, 891–899.

[13] Wu, C.-C.; Liu, W.-G.; Hung, W.-Y.; Liu, T.-L.; Lin, Y.-T.; Lin, H.-W. *Appl. Phys. Lett.* **2005**, *87*, 052103.

[14] Kawashima, Y.; Ohkubo, K.; Fukuzumi, S. *J. Phys. Chem. A* **2013**, *117*, 6737–6743.

[15] Agarwala, P.; Kabra, D. *J. Mater. Chem. A* **2017**, *5*, 1348–1373.

[16] (a) Bach, U.; Lupo, D.; Comte, P.; Moser, J. E.; Weissörtel, F.; Salbeck, J.; Spreitzer, H.; Grätzel, M. *Nature*, **1998**, *395,* 583–585. (b) Hawash, Z.; Ono, L. K.; Qi, Y. *Adv. Mater. Interfaces*, **2018**, *5*, 1700623.

[17] Jeon, N. J.; Lee, H. G.; Kim, Y. C.; Seo, J.; Noh, J. H.; Lee, J.; Seok, S. I. *J. Am. Chem. Soc.* **2014**, *136*, 7837–7840.

[18] Hu, Z.; Fu, W.; Yan, L.; Miao, J.; Yu, H.; He, Y.; Goto, O.; Meng, H.; Chen, H.; Huang, W. *Chem. Sci.* **2016**, *7*, 5007–5012.

[19] (a) Krüger, J.; Plass, R.; Cevey, L.; Piccirelli, M.; Grätzel, M.; Bach, U. *Appl. Phys. Lett.* **2001**, *79*, 2085–2087. (b) Lee, M. M.; Teuscher, J.; Miyasaka, T.; Murakami, T.; Snaith, H. J. *Science*, **2012**, *338*,

643–647.

[20] (a) Fang, B.; Zhou, H.; Honma, I. *Appl. Phys. Lett.* **2005**, *86*, 261909. (b) Xia, J.; Masaki, N.; Lira-Cantu, M.; Kim, Y.; Jiang, K.; Yanagida, S. *J. Am. Chem. Soc.* **2008**, *130*, 1258–1263.

[21] Yan, Q.; Guo, Y.; Ichimura, A.; Tsuji, H.; Nakamura, E. *J. Am. Chem. Soc.* **2016**, *138*, 10897–10904.

[22] Naito, K.; Miura, A. *J. Phys. Chem.* **1993**, *97*, 6240–6248.

[23] (a) Wolfe, J. P.; Tomori, H.; Sadighi, J. P.; Yin, J.; Buchwald, S. L. *J. Org. Chem*. **2000**, *65*, 1158–1174. (b) Surry, D. S.; Buchwald, S. L. *Angew. Chem. Int. Ed*. **2008**, *47*, 6338–6361. (c) Surry, D. S.; Buchwald, S. L. *Chem. Sci.* **2011**, *2*, 27–50.

[24] (a) Dualeh, A.; Moehl, T.; Nazeeruddin, M. K.; Grätzel, M. ACS Nano *2013*, **7**, 2292–2301. (b) Minna, T.; Janne, H.; Lauri, P.; Peter, L. *Int. J. Photoenergy* **2009**, *2009*, 1–15. (c) Sebastián, P. J.; Olea, A.; Campos, J.; Toledo, J. A.; Gamboa, S. A. *Solar Energy Materials & Solar Cells* **2004**, *81*, 349–361.

[25] "*The Nature of the Chemical Bond*" *3rd Ed*.; Pauling, L.; Cornell University Press, New York, 1960.

[26] Burrezo, P. M.; Lin, N.-T.; Nakabayashi, K.; Ohkoshi, S.; Calzado, E. M.; Boji, P. G.; Garcia, M. A. D.; Franco, C.; Rovira, C.; Veciana, J.; Moos, M.; Lambert, C.; Navarrete, J. T. L.; Tsuji, H.; Nakamura, E.; Casado, J. *Angew. Chem. Int. Ed.* **2017**, *56*, 2989–2902.

[27] Zhu, X.; Tsuji H.; López Navarrete, J. T.; Casado, J.; Nakamura, E. *J. Am. Chem. Soc.* **2012**, *134*, 19254–19259.

[28] (a) Matsuo, Y.; Ozu, A.; Obata, N.; Fukuda, N.; Tanaka, H.; Nakamura, E. *Chem. Commun*. **2012**, *48*, 3878–3880. (b) Matsuo, Y.; Sato, Y.; Niinomi, T.; Soga, I.; Tanaka, H.; Nakamura, E. *J. Am. Chem. Soc*. **2009**, *131*, 16048–16050. (c) Matsuo, Y.; Kawai, J.; Inada, H.; Nakagawa, T.; Ota, H.; Otsubo, S.; Nakamura, E. *Adv. Mater.* **2013**, *25*, 6266–6263.

[29] Still, W. C.; Kahn, M.; Mitra, A. *J. Org. Chem. 1978,* **43**, 2923–2925.

[30] Blakesley, J. C.; Castro, F. A.; Kylberg, W.; Dibb, G. F.A; Arantes, C.; Valaski, R.; Cremona, M.; Kim, J. S.; Kim J.-S. *Organic Electronics* **2014**, *15*, 1263–1272.

Chapter 7.

Overview and Perspectives

The investigations in my doctoral course study demonstrated that the materials properties could be accumulated in one organic compound by integration of functional structures. The molecular design on backbone structure is the most important to determine the fundamental properties of a series of compounds. The choice of substituents based on the mechanism enables to achieve desired properties and phenomena.

In Chapter 2, the combination of ACQ and AIE in one molecule was demonstrated. TAE core evoking AIE and benzofuryl subunits luminescing in solution were fused to constitute **TBFE**. This compound exhibited three-stage two-wavelength on-off-on fluorescence switching behavior in THF/H_2O solvents. The mechanism investigation revealed the switching is triggered by aggregation as designed, suggesting the utility of the molecular design strategy.

Chapter 3–6 describe on spiro-CPV, a spiro-conjugated carbocyclic backbone. In Chapter 3, the synthesis and properties of spiro-CPV backbone was firstly described. Thanks to rigidness of full-carbon moiety and axial chirality, spiro-CPV exhibited circularly polarized luminescence (CPL) with high Φ_{FL} and high thermal and photo-stability. The investigation on the potential energies of MO suggested inter-subunit electronic interaction via spiroconjugation.

Due to high stability, the spiro backbone was expected to be utilized in light-emitting devices or organic dye lasers. However, there still was room for the improvement of Φ_{FL} and k_r of spiro-CPV, opening up further applications. Chapter 4 describes the enhancement of radiative decay by π-elongation based on that k_r is ideally proportional to extinction coefficient. Expansion of the rigid π-system successfully increased the absorption intensity to result in k_r and Φ_{FL}. Especially, the phenylethynyl derivative achieved high k_r of 4.07×10^8 s^{-1} enough for ASE, and Φ_{FL} of 0.99, the highest value for organic CPL molecules. Further investigation for improvement of $|g_{lum}|$ and practical device application would pave the way for the development of CPL devices, such as organic CPL lasers.[1]

The structural rigidity upon photoexcitation is another advantage of the spiro carbocycle. In Chapter 5, the modification of electronic structure by the incorporation of heteroatom was demonstrated. The electronic properties changed due to electron donating and accepting effects of heteroatoms. Especially, the introduction of SO_2 group in the rigid and chiral backbone caused ICT, which possibly attribute to large $|g_{lum}|$ in CPL spectra. Moreover, the thiophene dioxide exhibits solvatochromic fluorescence because of the polarization upon photoexcitation. This study provided the insight that the inter-subunit electron transition is the key for improvement of dissymmetry factors in

the spiro-conjugated system, as well as for the achievement of materials properties such as TADF and environment responsivity.

Chapter 6 described the application of spiro-CPV backbone in HTMs. The attachment of diarylamino substituents on the four edges of spiro-CPV enhanced structural isotropy to show higher phase stability in amorphous state than spiro-OMeTAD. Fine-tuning of energy level was achieved by the choice of aryl groups on the amino moieties. The investigation on oxidation process revealed the inter-subunit electronic interaction in radical cation is enhanced via spiroconjugation, which resulted in the improvement of μ_h for their spin-coated films by oxidant doping.

These investigations on spiro-CPV established a novel organic backbone for luminescent and semiconducting applications. I expect further investigation based on these works would expand the potential use of organic materials. The characteristic conjugation via π-system and spiro-linkage would provide possibility for wider applications, such as singlet-fission materials,[2] single molecular devices,[3] and asymmetric catalysts.[4] The further investigation on ICT system in this backbone would enable not only the enhancement of $|g_{lum}|$ but also high electroluminescence property by thermally activated delayed fluorescence.[5] While I demonstrated the application in HTM here, considering conventional π-conjugated materials have been utilized as ETM[6] and host materials for OLED,[7] spiro-CPV would be a promising backbone for these applications as well due to its small reorganization energy.

References

[1] Jiménez, J.; Cerdán, L.; Moreno, F.; Maroto, B. L.; García-Moreno, I.; Lunkley, J. L.; Muller, G.; de la Moya, S. *J. Phys. Chem. C* **2017**, *121*, 5287–5292.

[2] (a) Kumarasamy, E.; Sanders, S. N.; Tayebjee, M. J. Y.; Asadpoordarvish, A.; Hele, T. J. H.; Fuemmeler, E.G.; Pun, A. B.; Yablon, L. M.; Low, J. Z.; Paley, D. W.; Dean, J. C.; Choi, B.; Scholes, G. D.; Steigerwald, M. L.; Ananth, N.; McCamey, D. R.; Sfeir, M. Y.; Campos, L. M. *J. Am. Chem. Soc.* **2017**, *139*, 12488–12494. (b) Sandoval-Salinas, M. E.; Carreras, A.; Casado, J.; Casanova, D. *J. Chem. Phys.* **2019**, *150*, 204306.

[3] (a) Farazdel, A.; Dupuis, M.; Clementi, E.; Aviram, A. *J. Am. Chem. Soc*. **1990**, *112*, 4206–4214. (b) Sowa, J. K.; Mol, J. A.; Briggs, G. A. D.; Gauger, E. M. *J, Phys. Chem. Lett.* **2018**, *9*, 1859–1865.

[4] Xie, J.-H.; Zhou, Q. L. *Acc. Chem. Res.* **2008**, *41*, 581–593.

[5] (a) Tao, Y.; Yuan, K.; Chen, T.; Xu, P.; Li, H.; Chen, R.; Zheng, C.; Zhang, L.; Huang, W. *Adv. Mater.* **2014**, *26*, 7931–7958. (b) Yang, Z.; Mao, Z.; Xie, Z.; Zhang, Y.; Liu, S.; Zhao, J.; Xu, J.; Chi, Z.; Aldred, M. P. *Chem. Soc. Rev*. **2017**, *46*, 915–1016.

[6] Kulkarni, A. P.; Tonzola, C. J.; Babel, A.; Jenekhe, S. A. *Chem. Mater.* **2004**, *16*, 4556–4573.

[7] Tao, Y.; Yang, C.; Qin, J. *Chem. Soc. Rev.* **2011**, *40*, 2943–2970.